High-Q MEMS Capacitive-Gap Resonators for RF Channel Selection

Lingqi Wu

Electrical Engineering and Computer Sciences
University of California at Berkeley

December 1, 2017

High-Q MEMS Capacitive-Gap Resonators for RF Channel Selection

by

Lingqi Wu

A dissertation submitted in partial satisfaction of the

requirements for the degree of

Doctor of Philosophy

in

Engineering – Electrical Engineering and Computer Sciences

in the

Graduate Division

of the

University of California, Berkeley

Committee in charge:

Professor Clark T.-C. Nguyen, Chair
Professor Tsu-Jae King Liu
Professor Liwei Lin

Fall 2015

High-Q MEMS Capacitive-Gap Resonators for RF Channel Selection

Abstract

High-Q MEMS Capacitive-Gap Resonators for RF Channel Selection
by

Lingqi Wu

Doctor of Philosophy in Engineering — Electrical Engineering and Computer Sciences

University of California, Berkeley

Professor Clark T.-C. Nguyen, Chair

On chip capacitive-gap transduced micromechanical resonators constructed via MEMS technology have achieved very high Q's at both VHF and UHF range, making them very attractive as on-chip frequency selecting elements for filters in wireless communication applications. Still, there are applications, such as software-defined cognitive radio, that demand even higher Q's at RF to enable low-loss selection of single channels (rather than bands of them) to reduce the power consumption of succeeding electronic stages down to levels more appropriate for battery-powered handhelds.

This dissertation focuses on improving the performance of MEMS capacitive-gap resonators to the degree which can be used to build the aforementioned RF channel-select filters. It first aims to enhance quality factor of MEMS capacitive-gap resonators by suppressing vibration energy loss via device substrate, which will lead to low insertion loss in RF channel selection. Then, in order to reduce an RF front-end filter's bandwidth and termination resistance, it explores the method of building micromechanical resonator array composites that include large number of mechanically coupled resonators. Finally, the dissertation presents an experimentally demonstrated RF narrowband filter built upon mechanically coupled high-Q resonator array composites.

Pursuant to further increasing Q at UHF for low insertion loss RF channel select application, the thesis develops an equivalent circuit model of a radial contour mode disk resonator that can analytically predict anchor loss dominated Q. Indicated by this improved equivalent circuit model, this work "hollows" the stems supporting all-polysilicon micromechanical disk resonators to effectively squeeze the energy conduit between the disk structure and the substrate, thereby suppressing energy loss and maximizing Q. By using the same fabrication process flow from the conventional all-polysilicon devices, the use of hollow stem support enhances Q with minimal increase in fabrication complexity. Measurements confirm Q enhancements of 2.6× for contour modes at 154 MHz and 2.9× for wine glass modes around 112 MHz over values previously achieved by full stem all-polysilicon disk resonators with identical dimensions. Measured Q's as high as 56,061 at 329 MHz and 93,231 at 178 MHz for whispering gallery modes further attest to the efficacy of this approach.

This dissertation also employs mechanically coupled disk array composites to increase resonator stiffness and lower motional resistance, which are both highly desired for RF

front-end channel-select filters. By using half-wavelength coupling beams and proper electrode phasing design, measurements confirm that a 215-MHz 50-resonator disk array achieves $46.5\times$ Q-normalized R_x reduction, with no observation of other undesired vibration modes. Notably, as indicated by the newly developed negative-capacitance equivalent circuit model, such array composite also shows enhanced frequency stability against dc-bias voltage fluctuations because of its large electrode-to-resonator overlap capacitance.

Finally, the thesis demonstrates a 75MHz 3$^{\text{rd}}$ order 210 kHz bandwidth (0.3%) filter with a sharp roll-off of 20dB shape factor of 1.46. This filter employs three high-Q disk array composites connected by quarter-wavelength rotational coupling beams to achieve a weak coupling for narrowband selection. Each array composite itself includes seven flexural disk resonators coupled by strong quasi-zero length beams to enforce desired response. By using electromechanical analogies, the equivalent electrical circuit model of this filter can accurately capture the device's response and provide insights for filter designers.

Most importantly, the accuracy of the described equivalent circuit model in predicting quality factor, frequency stability, and filter response encourages the design of even more complex micromechanical circuits to come, for example, as would be needed in an all-mechanical RF front-end.

To my parents and Fangran

TABLE OF CONTENTS

List of Figures

LIST OF TABLES

ACKNOWLEDGEMENTS

To end this, I want to share a quote that has supported me through all these years and will definitely keep me going in the future:

"You can't connect the dots looking forward, you can only connect them looking backwards. So you have to trust that the dots will somehow connect in your future."

You will never know in what ways certain experiences will bring great benefits later in life.

Chapter 1 Introduction

1.1. Motivation: RF Channel Select Filters

Future mobile transceivers will need more flexibility to accommodate the fast evolving wireless communication protocols and the increasing need for cell phones that can truly operate in any places around the world. The desire for reconfigurable radios that are capable of adapting to any communication standards and environments at any location across the world has spurred great interest in the concept of a software defined radios (SDR) [1] [2], in which the frequencies and modulation schemes of any existing communication standard can be produced in real time by calling up a software. The goal of such a radio is to realize radio functions digitally much as possible, which requires the analog-to-digital converter (ADC) to be placed as close to the antenna as possible so that as much signal processing as possible could be done digitally. To achieve this, a RF front-end filter that can enable low-loss selection of single channels (rather than bands of them) is needed to reduce the power consumption of succeeding electronic stages down to levels more appropriate for battery powered handhelds.

To better understand why SDR needs channel select filters, we need to know how a cell phone transceiver works. Figure 1.1 presents the block diagram of a traditional super-heterodyne receiver with a band select RF front-end filter. There are two band pass filters in this block diagram that contribute to picking the low power desired signal out of the transmitted signals. As illustrated in Figure 1.2, the first RF pre-select filter at ultra-high frequency (UHF) range band selects the transmitted signal, which not only includes desired signal, but also very high power blockers with frequencies very close to the desired signal. While the second IF filter only selects the wanted signal, which reduces the input power
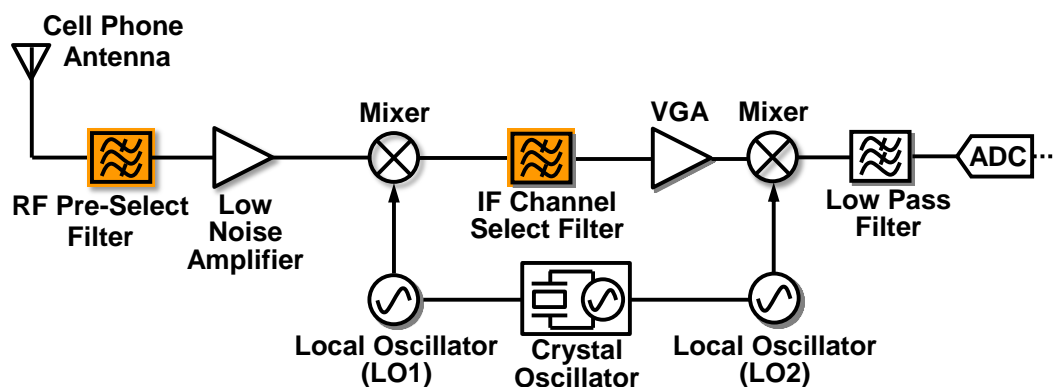
Figure 1.1. Simplified block diagram of a super-heterodyne receiver
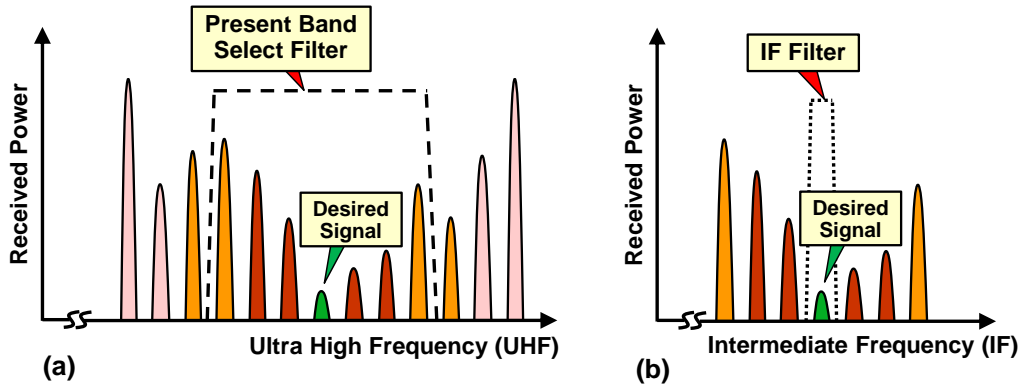
Figure 1.2: Illustration of: (a) frequency spectrum selected by a traditional RF band select filter. (b) down converted frequency spectrum selected by an IF channel select filter.
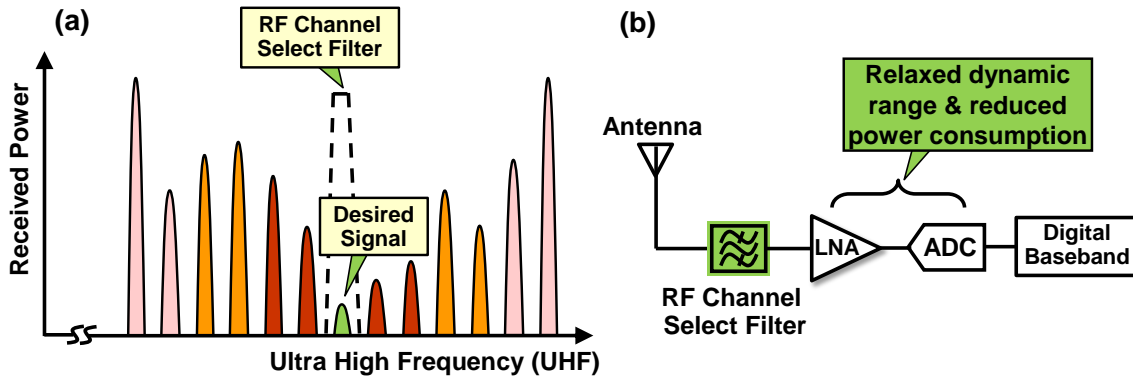
Figure 1.3: (a) Illustration of frequency spectrum selected by a new RF channel select filter. (b) Simplified schematic of a possible software defined radio block diagram.

level and the dynamic range requirement of the following ADC. To build a SDR receiver, the ADC needs to move as close to the antenna as possible, e.g. directly after low noise amplifier (LNA). Such reconfiguration to SDR will need to operate ADC at a much higher frequency and with a very high dynamic range to handle the power of blockers, both of which could lead to high power consumption that is not suitable for portable handsets [3]. Here, the pre-select filter in the SDR block diagram plays a very important role in reducing power consumptions.

As the bandwidth of the pre-select filter decreases, more interferers are suppressed, and the needed dynamic range of the LNA and ADC relaxes, leading to less power consumption. Therefore a RF front-end channel select filter that can take only the desired signal and reject all interferers is needed to implement the SDR with a reasonable power consumption. For GSM, where emissions are regulated so that each 200 kHz channel is sandwiched by empty spectrum in any given cell, a channel select filter with bandwidth of 600 kHz (0.067% percent bandwidth) would only select the desired signal and knock down the ADC power consumption to a reasonable 80mW. While a 35 MHz bandwidth of a conventional pre-select filter will force an ADC operating at 3 GHz bandwidth to consume a highly impractical 45 W [3]. As shown in Figure 1.3, with RF channel select filter selecting only
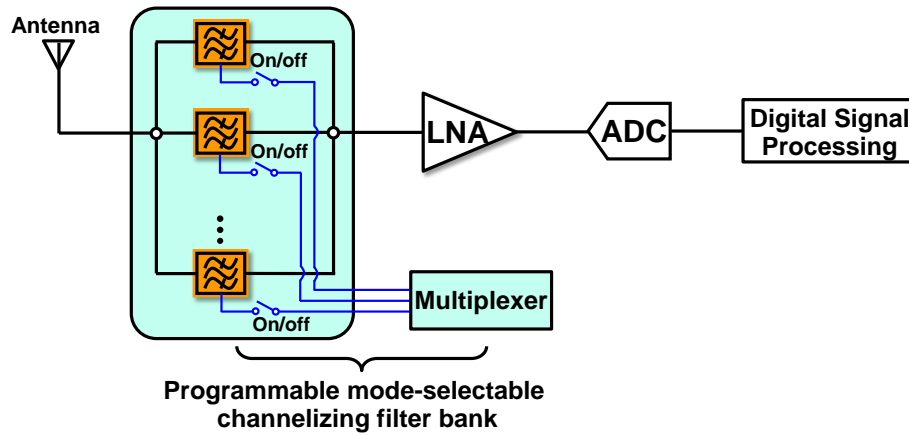
Figure 1.4: System block diagram for a programmable SDR front-end utilizing a RF channel-select filter network to realize a frequency selecting function at will for any communication standards.

the desired signal, the power sent to LNA and ADC dramatically reduces, which can potentially reduce the power consumption down to a level that can be supported by a portable handset battery [3].

Ultimately, all functions in a SDR implementation should be programmable, including any pre-select filtering functions. In other words, a SDR would require a RF front-end channel select filter that can be tuned to pass and reject tiny RF frequency channels at will along the entire input frequency span, e.g. 0 to 3GHz frequency range. However, such tunability requirement often contradicts with the channel select filter's high Q requirement, as it is often the case that the higher the Q of a resonator, the less tunable it is. In fact, at the time of this writing, there are no existing resonator technologies capable of achieving $Qs > 30,000$ while also being continuously tunable over a 3 GHz frequency span.

An alternative way to achieve the desired programmable frequency selecting is to build a bank of filters, with each of them centered at different frequency, which dispenses with the need to tune a given resonator's frequency over a wide range. Figure 1.4 shows the ultimate proposed block diagram of an SDR front-end utilizing a RF channel-select filter banks to realize the function of real time frequency selecting at will. With each individual channel select filter switchable, the filter bank can be reconfigured to be compatible with any communication standard by the code controlled multiplexer, which realizes a programmable mode-selectable communication front-end.

1.2. Narrowband Filter Design Challenges

The need for such a small percent bandwidth filter that can pass and reject tiny RF frequency channels at will makes software defined radio very difficult to realize, since the smaller the percent bandwidth, the higher the needed Qs of resonators comprising a given filter to maintain reasonable insertion loss. In addition, to realize small percent bandwidth at high frequency, coupling beams need to have very small cross-sectional area, which poses fabrication challenges during lithography and etching when making these beams.
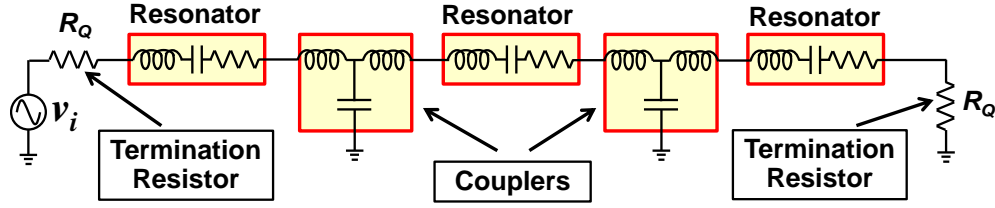
Figure 1.5: Topology of a 3rd order channel select filter with termination resistors at the I/O ports. Here, each resonator has identical resonance frequency and the filter's center frequency would be the same as the resonance frequency of resonators.
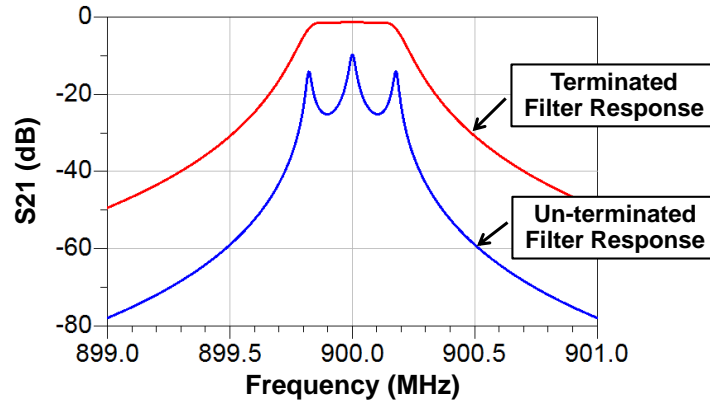
Figure 1.6: Simulation results of terminated and un-terminated filter response. The termination resistors R_Q 'flatten' the 3 slightly separated resonance peaks of the coupled 3-resonator composite.

1.2.1. Low Insertion Loss (*I.L.*)

To better understand why quality factor of resonators affects a filter's insertion loss, Figure 1.5 presents the schematic of a 3rd order narrow band filter. Here, 3 identical resonators with couplers connected in-between them will together create a single mechanical vibration system that has three slightly separated resonance peaks, as shown in Figure 1.6. Such multi-peak response looks like a filter pass band, but with ripples in passband. A pair of termination resistors with values of R_Q is needed at the I/O ports to generate an ideal band pass filter response.

For a filter with topology like Figure 1.5, quality factor of each individual resonators Q_r and the filter percent bandwidth P_{BW} together determine the filter's insertion loss. Basically, higher Q_r and lower filter quality factor Q_f ($Q_f = 1/P_{BW}$) will lead to lower insertion loss, as indicated by the following expression:

$$IL \propto q_i \frac{Q_f}{Q_r} \quad (if\ Q_f \gg Q_r) \tag{1.1}$$

where q_i is a normalized parameter obtained from a filter cookbook and is mainly dependent on filter type and filter order [4].
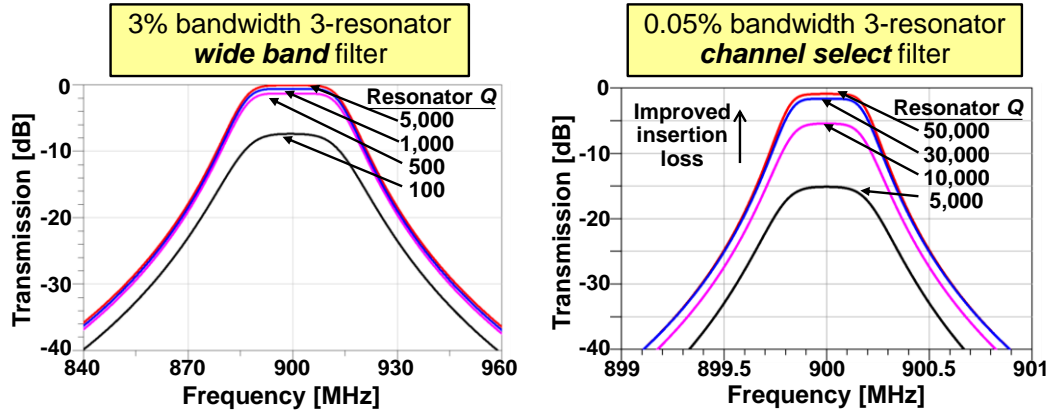
Figure 1.7. Simulated frequency characteristics for 900 MHz filters with varying constituent resonator Q's, illustrating how resonator Q and filter bandwidth together govern the insertion loss of a filter. (a) For a 3% bandwidth 3rd order filter, resonators with Q larger than 500 will lead to insertion loss less than 3 dB. (b) For a 0.05% bandwidth 3rd order channel select filter, even Qs in the order of 10,000 for individual resonators still generate severe insertion loss.

Figure 1.7 compares the dependence of insertion loss on resonator Q_r for a 3% bandwidth band select filter and a 0.05% bandwidth channel select filter, both at 900 MHz center frequency. For the 3% bandwidth filter, resonators with Q of 1,000 is good enough to achieve insertion loss (*IL*) less than 1dB. However, for the 0.05% bandwidth channel select filter, resonators with Q_r as high as 10,000 would still lead to insertion loss larger than 5dB. To achieve less than 3dB insertion loss for a 3rd order channel select filter, Q_r around 30,000 is needed for individual resonators, which is very challenging and difficult to achieve using current technologies such as SAW, FBAR or BAW resonators.

1.2.2. Narrow Bandwidth

For a narrowband filter using the topology in Figure 1.5, the equivalent stiffness ratio of resonator to mechanical coupler will largely determines the percent bandwidth (P_{BW}), as shown in the following expression:

$$P_{BW} = \frac{1}{k_{ij}} \cdot \frac{k_s}{k_{re}} \tag{1.2}$$

where k_{ij} is the normalized coupling coefficient between resonator tanks for a given filter type (i.e., Butterworth, Chebyshev, etc.) [4], k_s represents the coupler's stiffness, and k_{re} is the equivalent stiffness of the resonator. Indicated by (1.2), a narrowband filter will need high stiffness resonators and low stiffness couplers.

A coupler's stiffness is generally determined by its material and geometry. To lower the mechanical stiffness of couplers, a narrowband filter desires coupling beams with small Young's modulus, small cross sectional area and length corresponding to quarter-wavelength ($\lambda/4$) of the propagating acoustic wave, as will be discussed in Chapter 5. However, as the center frequency of a narrowband filter goes up, the resonator's equivalent

stiffness k_{re} may keep constant, e.g. for radial contour mode disk type resonators which will be discussed in Chapter 2 and Chapter 3, but the equivalent quarter-wavelength will decrease and lead to shorter coupling beams and higher stiffness, causing higher bandwidth. This will pose fabrication challenges because designers need to shrink the cross sectional area of coupling beams to compensate increased bandwidth, which will increase difficulties in lithography and etching when making these beams using microfabrication technology. For example, for a 2nd order Chebyshev filter based on polycrystalline silicon type disk resonators, a 0.5% bandwidth at 70 MHz will need 0.55 μm wide coupling beams. However, if frequency goes up to 700 MHz, the width of the coupling beams will have to shrink down to 55 nm in order to keep the same percent bandwidth, which is challenging to fabricate with a good control of tolerance.

To overcome this issue, designers need to boost the resonator stiffness in a narrowband filter such that the requirement on the coupler's stiffness will relax. One good way to do this is to make micromechanical disk array composite that will behave similar to a resonator, but with $N\times$ higher stiffness, in which N is the number of resonators in an array composite. Ideally, such array will also have $N\times$ smaller motional resistance and $N\times$ larger linearity, which potentially reduces a filter's termination resistance and power handling, both of which are desired by RF front-end channel select filters. The thesis will discuss in details on the coupled resonator array composite method in Chapter 4.

1.3. High Q Capacitive-Gap MEMS Resonators

Considering the requirements and challenges discussed above to achieve a software defined RF receiver, MEMS capacitive-gap resonators would be a very good candidate with high quality factor, on/off switchable capacity, and .wafer level manufacturing capability which could enable massive numbers of filters in a single chip. A capacitive-gap micromechanical resonator usually consists of a suspended mechanical structure and capacitive transducers that convert energy between electrical domain and mechanical domain. It offers the best fQ (frequency-quality factor product) among different types of micromechanical resonators [5], since they generally are constructed in single high quality materials, and thus suffer less from the material interface losses that can encumber other transducer types (e.g., piezoelectric). Figure 1.8 compares the quality factor of a capacitive-gap disk resonator and a piezoelectric ring resonator at similar frequencies around 500 MHz. the capacitive-gap disk resonator achieved $10\times$ higher Q compared with the piezoelectric resonator. Although piezoelectric transducers may be more successful in achieving lower impedances between 50 Ω and 377 Ω for matching to off-chip wireless components [6], capacitive-gap devices can scale down their impedances by using some of the recent developed techniques [7] [8]. In addition to better Q, capacitive-gap resonators also offer more flexible geometries with CAD-definable frequencies, as they can take the form of many shapes, such as beams, disks, rings, or plates [9] [5] [10] [11], and their frequencies usually depend on lateral geometries that can be defined by lithography.
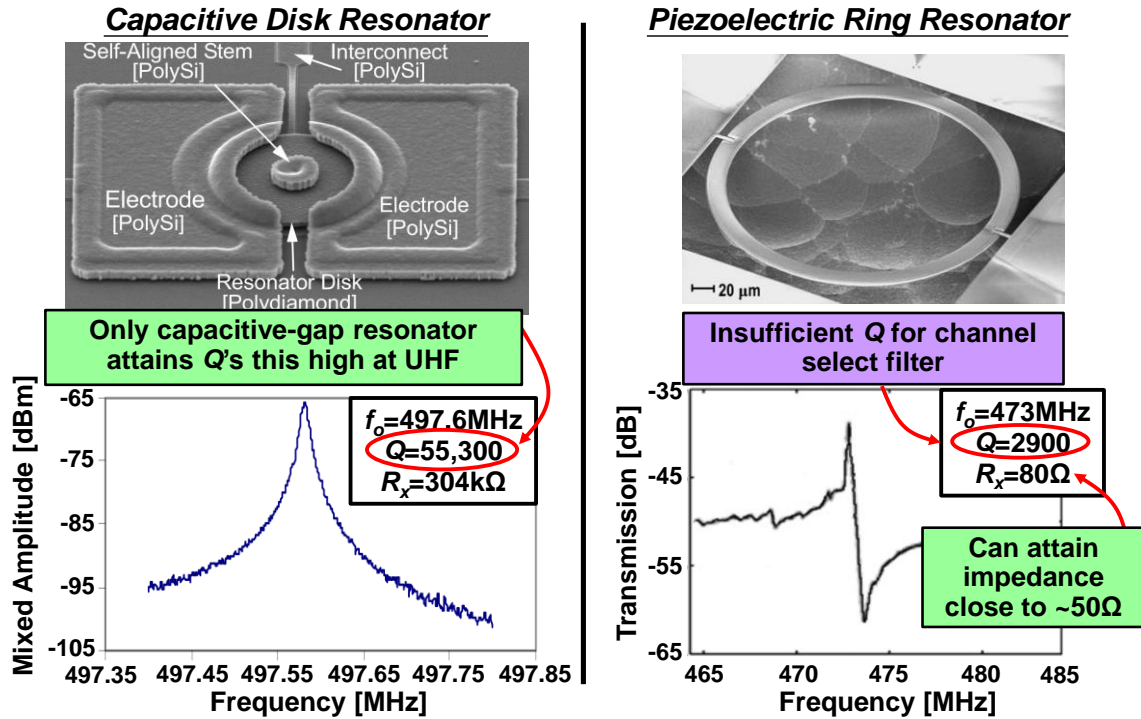
Figure 1.8: *Q* Comparison between a capacitive-gap disk resonator and a piezoelectric ring resonator at similar resonance frequencies.
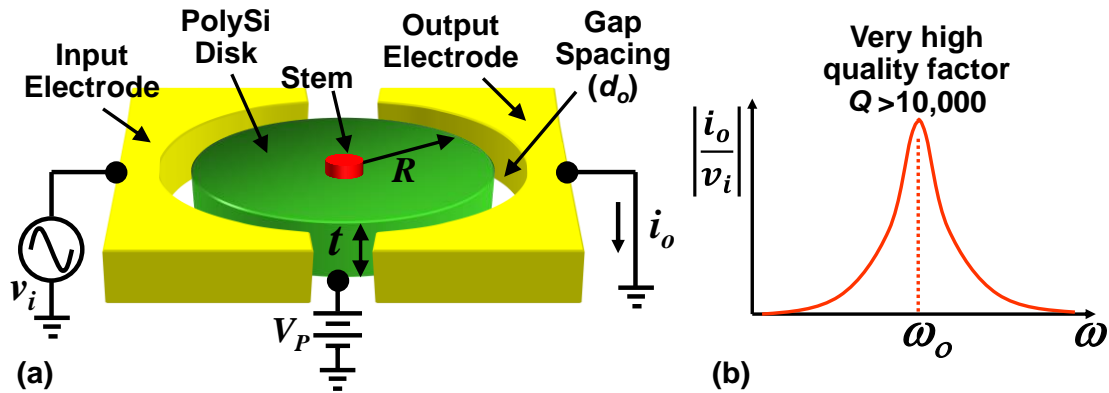
Figure 1.9: (a) Schematic of a capacitive-gap all-polysilicon micromechanical disk resonator in a two-port excitation and sensing configuration; (b) Typical output current frequency spectrum of a capacitive-gap disk resonator with very high quality factor.

Figure 1.9 depicts a capacitive-gap disk type resonator in a typical bias, excitation, and detection scheme. This device comprises a polysilicon disk surrounded by two closely spaced electrodes and supported by an anchored stem attached at the center of the disk. The device is excited into resonance via a combination of a dc-bias voltage V_P applied to the conductive polysilicon resonant structure and an ac signal v_i applied to the input electrode, which together induce a force at the frequency of v_i that drives the disk into

resonance when the frequency of v_i matches the resonance frequency. Once vibrating, the V_P-biased time varying capacitance between the disk and its output electrode generate an output current detectable by measurement instrumentation, as shown in Figure 1.9 (b). The resonance frequency of a radial contour mode disk resonator can be expressed by:

$$f_{nom} = \frac{1}{2\pi} \sqrt{\frac{k_r}{m_m}} \propto \frac{1}{R} \sqrt{\frac{E}{\rho}}$$

(1.3)

where k_r, m_m, R, E, and ρ represent the equivalent dynamic stiffness, equivalent mass, radius, material Young's modulus, and density of disk resonator structure, respectively. With resonance frequency determined by the lateral dimensions R that are CAD-definable, such devices can enable a bank of filters with various center frequencies on a single chip.

1.4. Existing Techniques to Enhance Quality Factor

On chip capacitive-gap vibrating polysilicon micro-mechanical resonators have achieved Q's over 160,000 at 61 MHz [12] and larger than 40,000 at ~3 GHz [5], making them very attractive as on-chip frequency selecting and set-ting elements for filters and oscillators in wireless communication applications. There are many energy loss mechanisms that could be responsible for limiting the Q of micromechanical resonators, including gas damping, anchor loss via anchors, thermoelastic dissipation (TED), phonon-phonon interaction and phonon-electron interaction [13]. The aforementioned high Q's were usually achieved by first recognizing that anchor loss dominated among all these loss mechnisms.at UHF, then using design strategies to suppress such loss, such as attaching to the vibrating structure at nodal locations [9], designing quarter wavelength supports [9] [14], using different materials for the support and vibrating structure to effect an energy reflecting impedance mismatch [15], and minimizing support dimensions (e.g., reducing stem size [11].

1.4.1. Nodal Point Anchor

A very commonly used technique to suppress anchor loss and enhance Q is to place support structure at the nodal points of a resonator's mode shape. Here, the nodal points of a vibrating mechanical system refer to areas in a mode shape that have zero-displacement at all time. By attaching anchors to the nodal points, resonators will introduce minimum displacement into the substrate through anchors, which reduces energy dissipation and maximizes the Q. Figure 1.10(a) shows the SEM of a polysilicon flexural mode beam from [9] with four supporting beams placed at its 1st order flexural mode nodal points, which are $0.224L_r$ (L_r is the total beam length) away from the two ends of the beam, as indicated by the cross section schematic in Figure 1.10(b). Compared with the clamped-clamped beam counterparts in which the anchors are placed directly at the two ends, the free-free beam resonator achieves a very high Q of 8,250, a 27.5× improvement over the clamped-clamped
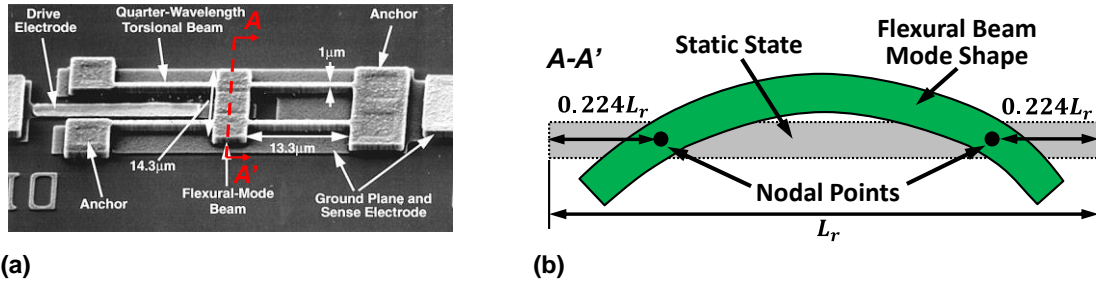
Figure 1.10: (a) SEM of a 71.49-MHz free-free beam micromechanical resonator with supporting beams placed at nodal points of the 1st order flexural mode shape. (b) Schematic of a flexural beam mode shape showing that the nodal points are located 0.224L_r away from the two ends of the beam structure, where L_r is the total length of the beam.

beam's Q's of 300, which clearly demonstrates the effectiveness of nodal point attachment method for high Q resonator design. In this thesis, the micromechanical disk resonator also follows such design guidelines by placing the supporting stem right at the center of the disk, which is the nodal point of the mode shape of interest.

1.4.2. Quarter Wavelength Supporting Beam

As identified in Figure 1.10 that the free-free beam micromechanical resonator is supported by four supporting beams attached at its fundamental-mode nodal points, the support springs sustain no translational movement during vibration and, thus, anchor loss due to translational movements—such as those sustained by clamped-clamped beam resonators—are greatly alleviated. However, Figure 1.10(b) indicates that the nodal points still experience rotational movement, even though the translational displacement is zero. Therefore the free-free beam resonator will still apply rotational torques onto the anchors via supporting beams, which induces substrate displacement and thus impacts Q.

With the recognition that the supporting beams actually behave like acoustic transmission lines at the frequencies of interest, the torsional loss mechanisms can be negated by strategically choosing support dimensions so that they present virtually no impedance to the free-free beam. In particular, by choosing the dimensions of a torsional support beam such that they correspond to an effective quarter-wavelength of the resonator operating frequency, the solid anchor condition on one side of the support beam is transformed to a free end condition on the other side that connects to the resonator. In terms of impedance, the infinite acoustic impedance at the anchors is transformed to zero impedance at the resonator attachment points. As a result, the resonator effectively "sees" no support at all and operates as if levitated above the substrate, devoid of anchors and their associated loss mechanisms.

The above transformation can be more readily seen using the equivalent acoustic T network model for a torsional supporting beam using the analogy where force is the across variable and velocity is the through variable [16]. In particular, when the dimensions of a given support beam correspond to an effective quarter-wavelength of the resonator operation frequency, its equivalent acoustic T-network takes the form shown in Figure
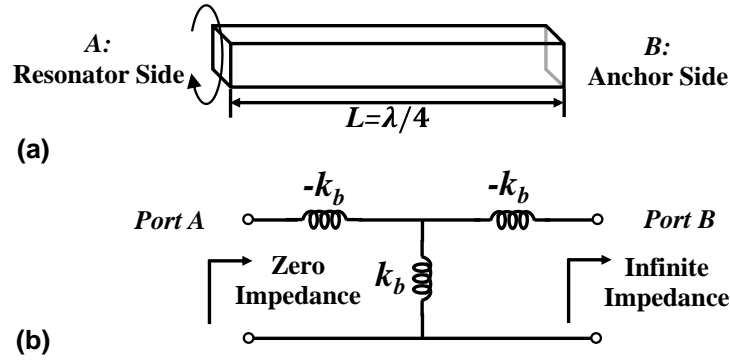
Figure 1.11: (a) Quarter-wavelength torsional beam with *B* side connecting to anchor and *A* side connecting to resonator. (b) Equivalent acoustic network showing zero impedance at port *A* with port *B* open.

1.11(b), where shunt and series arm impedances are modeled by equal and opposite stiffness. Given that in this mechanical circuit, anchoring the beam of Figure 1.10(a) at side *B* corresponds to opening the *B* port of Figure 1.11(b), it is clear that the impedance seen at port A will be zero due to cancellation of the remaining impedances in the circuit of Figure 1.11(b). Seeing zero impedance from port *A* represents the situation that the supporting points are effectively in free condition, which ideally will have no anchor loss and therefore maximize *Q*.

The quarter-wavelength support method contributes to *Q* enhancement for resonators with many different type of support couplings, e.g., rotational coupling [9], flexural coupling [17], and extensional coupling [5]. For example, the quarter-wavelength supporting beams contribute to achieve an extremely high *Q* of over 40,000 at ~3 GHz for a polydiamond ring type micromechanical resonator, which till now sets the highest *fQ* product for acoustic MEMS resonators [5].

1.4.3. Material Mismatched Anchor

Ultimately, the previously discussed strategies to suppress anchor loss all seek to create large acoustic impedance mismatches at the resonator-anchor boundaries in an attempt to confine the acoustic energy within the resonator structure during resonance vibration, thereby preventing energy loss to the surroundings. Knowing this, and further recognizing the potential difference in characteristic acoustic impedance between different materials lead to another very effective method to boost *Q*—using material mismatched anchor. The work of [18] used HFCVD (hot filament chemical vapor deposition) polydiamond for the disk structure, but polysilicon for the stem, to effect a material mismatch between the disk and stem that reflects energy back into the disk structure, preventing the energy leakage that would otherwise lower the *Q*. The degree of reflection can be modeled and designed analogously to electrical transmission lines to generate a non-zero reflection coefficient for acoustic waves at the resonator-anchor boundary, preventing energy from flowing into the stem anchor towards the substrate. Figure 1.12 specifically illustrates how a stem made in the same material as the disk does little to impede energy flow; whereas a mismatched stem made in a material different from that of the disk suppresses energy loss to the substrate.
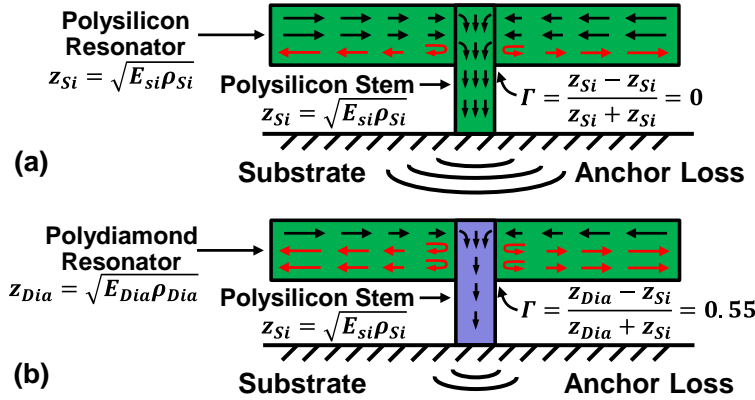
Figure 1.12: Schematics comparing energy losses to the substrate for (a) a polysilicon disk with an impedance matched polysilicon stem; and (b) a polydiamond disk with a material-mismatched polysilicon stem, where (b) loses much less energy.
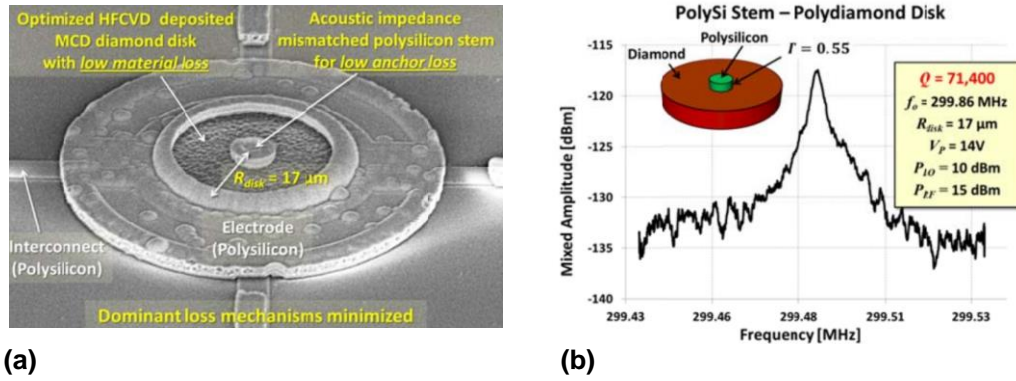
Figure 1.13: (a) SEM image of a 300-MHz contour mode disk resonator constructed with HFCVD polydiamond disk and polysilicon supporting stem. (b) Measured frequency response for a polydiamond contour mode disk resonator employing a material-mismatched polysilicon stem [18].

By using the material mismatched anchor for contour mode micromechanical disk resoantors, the work in [18] exhibits a very high Q of 71,400 at 299.86 MHz, which is the highest series resonant Q measured at this frequency for an on-chip micromechanical resonator at room temperature at the time of publication, as shown in Figure 1.13(b). The polysilicon disk with impedance matched stem, on the other hand, posts a much lower Q of only 20,912, which is 0.29× of the acoustic impedance mismatched diamond device. The measured results clearly confirm the efficacy of the material-mismatching method to suppress energy loss to the substrate and enhance quality factor.

1.4.4. Anchor Geometry Scaling

Another obvious way for Q-enhancement is to shrink the size of supporting anchors of a micromechanical resonator to reduce its cross-sectional area and thereby reduce the conduit through which energy can pass from the vibrating resonator to the substrate. In
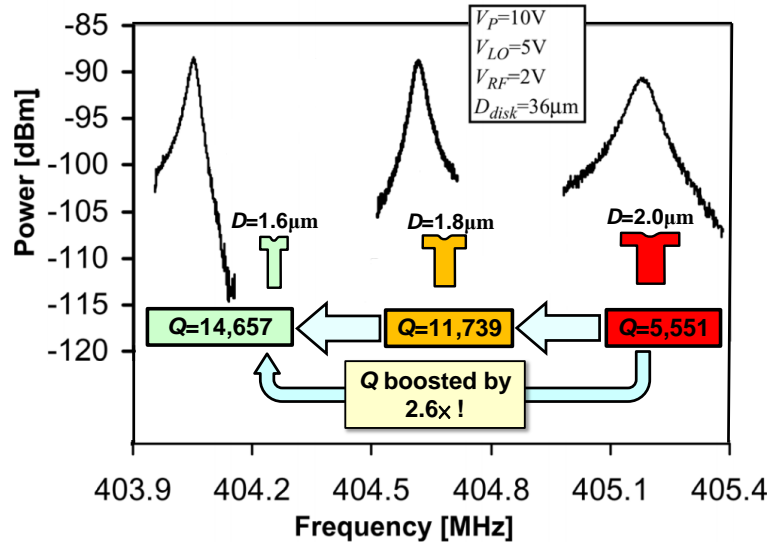
Figure 1.14: Frequency characteristics for 36-μm dismeter disk resonators operating in the 2nd radial-contour mode with self-aligned stem diameters varying from 1.6 μm to 2.0 μm [11].

particular, by reducing stem sizes from 2.0 μm to 1.6 μm, Figure 1.14 showed a measured Q increase from 5,551 to 14,657 for 405-MHz polysilicon radial-contour mode disk resonators. In keeping with several theoretical studies in the literature [19] [20] [21], even higher Q's are expected as anchors dimensions decrease to submicron range.

Unfortunately, there are of course practical barriers to continued scaling of stem diameters for a micromechanical disk resonator. First, as a stem is thinned, its strength wanes, so there is a minimum stem diameter and length that can support a disk of a given size. Second, even if a stem maintained sufficient strength while scaled to nanometer dimensions, the need to not only form it, but also place it exactly at the disk center, poses fabrication challenges. To overcome these issues, the hollow stem approach used in this thesis employs a hollow cylinder with thin walls, rather than a single thin stem, to support the disk structure. Since the walls are thin, the cross-sectional area of the stem is still very small. However, as with all hollow cyliners (e.g., pipes, lances, etc.), it still retains much of the strength of a full stem with the same diameter, which will be discussed with more details in the following sections.

1.5. Conventional Equivalent Circuit of Capacitive-Gap Resonators

To conveniently model and simulate the behavior of a micromechanical radial contour mode disk resonator in a way that facilitates circuit analysis, Figure 1.15 presents a traditional ac small-signal electrical equivalent circuit of a radial contour mode disk resonator, which includes a core *lcr* tank to model the mechanical vibration, a variable capacitor to model the dependence of resonance frequency on electrical stiffness k_e, and a pair of transformers to represent the electromechanical couplings.
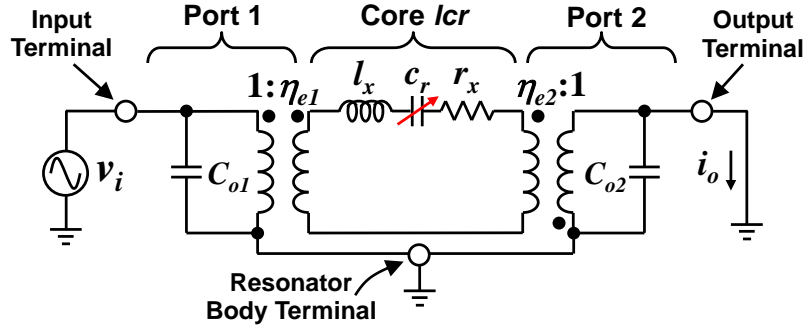
Figure 1.15. Classic equivalent electrical circuit for a capacitive gap micromechanical disk resonator with electrical stiffness lumped into the variable capacitance c_r.

1.5.1. Core *lcr* Tank

Despite its mechanical nature, the disk resonator of Figure 1.9(a) still looks like an electrical device when looking into its ports, and so can be modeled by the electrical inductor-capacitor-resistor (*lcr*) equivalents shown in Figure 1.15. Expressions for the element values in the *lcr* equivalents take the form:

$$l_x = m_m, c_r = \frac{1}{k_r} = \frac{1}{k_m - k_e}, r_x = b_m \tag{1.4}$$

where m_m, k_r, k_m, k_e and b_m are the actual values of dynamic mass, equivalent stiffness, mechanical stiffness, electrical stiffness, and damping constant of the resonator being modeled at the core *lcr* location. For radial contour mode shape with all points on the sidewalls of the disk moving the same amount, the perimeter of the disk structure usually becomes the core *lcr* location. The equivalent mass can be obtained by dividing the total kinetic energy KE_{tot} by one-half the square of the velocity [11]. Doing so on the perimeter of the disk yields:

$$m_m = \frac{KE_{tot}}{\frac{1}{2} v^2 (R, \theta)} = \frac{2\pi \rho t \int_0^R r J_1^2 (hr) dr}{J_1^2 (hR)} \tag{1.5}$$

where ρ, t, and R are the material density, thickness, and radius of the disk structure; $J_n(hr)$ is the Bessel function of the first kind of order n; and h is a constant defined by Young's Modulus E, density ρ, Poisson ratio v, and radian resonance frequency ω_o:

$$h = \sqrt{\omega_o^2 \rho / \left(\frac{2E}{2 + 2v} + \frac{Ev}{1 - v^2} \right)} \tag{1.6}$$

From (1.4) and (1.5), expressions for l_x, c_r, and r_x in the *lcr* tank at a location on the disk perimeter can be obtained using the following relations [11]:

$$l_x = m_m \tag{1.7}$$

$$c_r = \frac{1}{\omega_o^2 m_m} \tag{1.8}$$

$$r_x = \frac{\omega_o m_m}{Q} \tag{1.9}$$

1.5.2. Electromechanical Coupling Factor η_{ei}

As the *lcr* tank only captures the mechanical behavior of the disk structure, this equivalent circuit also needs a transformer to model the transduction from mechanical domain to electrical domain or vice versa. A succinct derivation of the transformer turn ratio η_{ei}, which is also called the electromechanical coupling factor, follows directly from consideration of the mechanical forces generated by voltages applied to terminals of the disk resonator depicted in Figure 1.9(a). A dc-bias voltage V_P on the resonator body and an ac voltage signal v_i at the input together generate an electrostatic input force F_i in a radial direction that takes the following form:

$$F_i = \frac{1}{2}\frac{\partial C_i}{\partial r}(V_P - v_i)^2 \tag{1.10}$$

where C_i represents the electrode-to-resonator overlap capacitance when the disk moves r in radial direction, and $\partial C_i/\partial r$ is the change in electrode-to-resonator overlap capacitance per unit radial displacement at each corresponding port. Retaining only the dominant term in (1.10) at resonance frequency yields:

$$F_i \approx -V_P\left(\frac{\partial C_i}{\partial r}\right)v_i = -\eta_{ei}v_i \tag{1.11}$$

A first order approximation for $\partial C_i/\partial r$ can be obtained from the Taylor expansion of the C_i expression as follows [11]:

$$C_i(r) = C_{oi}\left(1 - \frac{r}{d_o}\right)^{-1} \rightarrow \frac{\partial C_i}{\partial r} = \frac{C_{oi}}{d_o}\left(1 - \frac{r}{d_o}\right)^{-2} \approx \frac{C_{oi}}{d_o} \tag{1.12}$$

which leads to the expression of electromechanical coupling factor η_{ei} as:

$$\eta_{ei} \approx \frac{V_P C_{oi}}{d_o} \tag{1.13}$$

where C_{oi} is the static electrode-to-resonator overlap capacitance at port i.

1.5.3. Frequency Pulling Effect from Electrical Stiffness k_e

Because the electrode-to-resonator capacitance is a nonlinear function of the disk radial displacement, as indicated in (1.12), there are actually many more force components generated than represented in (1.11). In particular, Taylor expanding (1.10) further to the second term yields the electrostatic input force F_i as:

$$F_i = \frac{1}{2} \cdot \frac{C_{oi}}{d_o}\left(V_P^2 - 2V_p v_i + v_i^2 + \frac{2V_P^2 r}{d_o} - \frac{4V_P v_i r}{d_o} + \frac{2v_i^2 r}{d_o}\right)$$
$$= \frac{1}{2} \cdot \frac{C_{oi}}{d_o}\left(\cdots - 2V_p v_i + \frac{2V_P^2 r}{d_o} + \frac{2v_i^2 r}{d_o} + \cdots\right)$$

(1.14)

where the last form includes only terms that can generate components at resonance frequency. Inserting $v_i = V_i \cos\omega_o t$ and $r = \Re\sin\omega_o t$ (where the fact that the displacement r is 90° phase-shifted from v_i has been accounted for) into (1.14) yields:

$$F_i = -\left[\frac{V_p C_{oi}}{d_o}V_i\cos\omega_o t - \left(V_p^2 + \frac{V_i^2}{2}\right)\frac{C_{oi}}{d_o^2}\Re\sin\omega_o t\right]$$

(1.15)

At resonance, the second force term in (1.15) is in phase with the radial displacement. This, together with the fact that it is also proportional to the displacement r, identifies this force component as equivalent to a stiffness, but in this case, one generated via electrical means. In particular, this force component arises from the increase and decrease in electric field strength across the electrode-to-resonator gap as the gap shrinks and grows, respectively, during mechanical resonance vibration. When the disk sidewall gets close to the electrode, the force pulling it into the electrode grows, and vice versa for the other direction, i.e. it decreases as the disk sidewall moves away from the electrode. Thus, rather than acting to oppose displacement, as is the case for mechanical stiffness, this force acts to enhance it, which effectively makes it a negative stiffness at port i, with spring constant equal to:

$$k_{ei} = \left(V_P^2 + \frac{V_i^2}{2}\right)\frac{C_{oi}}{d_o^2} \approx V_P^2 \frac{C_{oi}}{d_o^2}$$

(1.16)

where the last form assumes that V_i is much smaller than V_P—a condition for which the reader is cautioned isn't always the case, such as in micromechanical mixers [22].

The electrical stiffnesses of all electrodes will subtract from the mechanical spring constant of the resonator at the core *lcr* location, changing the resonance frequency of a two port radial contour mode disk resonator to:

$$f_o = \frac{1}{2\pi}\sqrt{\frac{k_r}{m_m}} = \frac{1}{2\pi}\sqrt{\frac{k_m - k_e}{m_m}} = f_{nom}\sqrt{1 - \frac{k_e}{k_m}} \approx f_{nom}\left(1 - \frac{1}{2}\cdot\frac{k_e}{k_m}\right)$$

(1.17)

Where k_r is the effective stiffness of the disk at any point on its perimeter, k_e is the total electrical stiffness contributed by all electrodes that surround the disk, k_m is the purely mechanical stiffness, and f_{nom} is the resonance frequency of the disk structure with zero dc-bias voltage applied, which can be calculated by the following expression:

$$f_{nom} = \frac{\alpha \kappa}{R_d} \sqrt{\frac{E}{\rho}} \tag{1.18}$$

where κ is a parameter dependent upon Poisson's ratio ($\kappa = 0.342$ MHz/μm for polysilion), and α is a mode-dependent scaling factor that accounts for higher order modes ($\alpha = 1$ for the 1st order radial contour mode). The last expression in (1.17) uses the binomial expansion to approximate f_o for the case in which the mechanical stiffness is many times larger than any of the electrical stiffness, which is generally true for devices in this thesis. Rearrange of (1.17) yields the fractional frequency change due to electrical stiffness as:

$$\frac{\Delta f}{f_{nom}} = -\frac{1}{2}\frac{k_e}{k_m} \tag{1.19}$$

1.5.4. Limitations of Conventional Equivalent Circuit Model

Indicated by (1.19), the resonance frequency of a radial contour mode disk resonator will be slightly lower than the mechanical natural frequency of the disk structure, due to frequency pulling effect of the force generated by time-varying changes in electric field strength as vibration changes the parallel-plate capacitive electrode-to-resonator gap. The ratio of electrical stiffness k_e to purely mechanical stiffness k_m actually captures the magnitude of such frequency shift. By inserting the expression of parallel-plate electrode-to-resonator overlap capacitance into (1.16), the total electrical stiffness k_e for a two-port radial contour mode disk resonator can be calculated as:

$$k_e = \frac{V_P^2(C_{o1} + C_{o2})}{d_o^2} = \frac{V_P^2 \epsilon A}{d_o^3} \tag{1.20}$$

where ϵ is the permittivity of the gap material (i.e., vacuum in this case) and A is the total overlap area between the resonator and its electrodes. Changes of any variables in k_e, such as dc-bias voltage noise, capacitance variation due to mechanical vibration, or charging induced bias voltage drift, can cause frequency stability issues for capacitive-gap MEMS resonators [23] [24].

The conventional equivalent circuit in Figure 1.15 models the influence of electrical stiffness on resonance frequency via the arrow through capacitor c_r (that indicates this capacitor is tunable) and by setting the value of c_r equal to $1/(k_m - k_e)$. Although this method for capturing electrical stiffness adequately predicts the resonance frequency, it

does not convey clearly to a circuit designer the impact of electrical stiffness on the overall circuit performance. Modeling the electrical stiffness in this way in fact hides some very important capacitive-gap resonator behaviors when emplaced into certain circuits. This model also encourages designers to dismiss the impact of electrical stiffness, since many designers just neglect the k_e part in the value of c_r when drawing up equivalent circuits.

To remedy the above deficiencies of the conventional equivalent circuit model, the thesis will introduce a more circuit design-friendly model presented in Figure 2.2 that captures the influence of electrical stiffness on device and circuit behavior using a negative capacitance exactly equal in magnitude to the shunt static electrode-to-resonator overlap capacitance C_{oi} at each electrode terminal. In addition, Chapter 2 will further improve this new negative capacitance equivalent circuit such that it can analytically predict anchor loss dominated quality factor for radial contour mode disk resonators.

1.6. Thesis Outline

This dissertation will focus upon design of high-Q resonators and mechanically coupled resonator array composites for RF channel select filter applications. It begins in Chapter 2 with development of a new type of ac small signal equivalent circuit model that not only clearly shows frequency pulling effect from electrical stiffness, but more importantly can analytically predict anchor-loss dominated Q in a circuit-design friendly way. Next, Chapter 3 addresses the extremely high Q requirement from channel select filters by using hollow stem support to suppress energy loss, and confirms the validity of the newly developed equivalent circuit by comparing the measured Q enhancement with what the circuit predicts. Chapter 4 focuses on an in depth discussion of mechanically coupled disk array composites, from coupling theory, to circuit modeling, to design robustness analysis. Compared with a stand-along resonator, a micromechanical disk array composite provides low motional impedance, high equivalent stiffness, and high linearity, all of which are desired by channel select filters. Finally, Chapter 5 presents the design, fabrication and measurement of a 3rd order channel select filter (0.3% bandwidth) based on mechanically coupled flexural mode disk array composites. Chapter 6 finishes with conclusions on the research above and provides a view on the future research direction.

Chapter 2 Anchor Loss Modeling of Contour Mode Disk Resonators

To conveniently model the behavior of a radial contour mode disk resonator in a way that facilitates circuit analysis, the traditional small-signal equivalent circuit in [25] used a core *lcr* tank to model the mechanical vibration of the disk, and a pair of transformers and capacitors in shunt to represent the electromechanical coupling. Although such equivalent circuit adequately predicts the performance of a contour mode disk resonator such as resonance frequency and motional resistance, it hides very important insights on how anchor geometries affect quality factor and fails to capture the anchor loss limited Q. In particular, it models a resonator's quality factor via a resistor r_x, which represents all energy loss mechanisms responsible for limiting the Q of micromechanical resonators, including gas damping, anchor loss, thermoelastic dissipation (TED), phonon-phonon interaction, and phonon-electron interaction [13]. By lumping energy dissipations from different loss mechanisms into one single resistor r_x, such circuit does not convey clearly to a designer the impact of anchor loss on the overall device quality factor, which usually dominates among all loss mechanisms in our cases [11] [26].

To remedy the above deficiencies, this chapter introduces a more insightful equivalent circuit model, which can capture the influence of stem geometries on the magnitude of anchor loss and predict the anchor loss dominated Q for radial contour mode disk resonators. For a center supported disk resonator, motion in the stem causes substrate vibration and generates energy dissipation through the substrate. To model such energy loss, the new equivalent circuit separates the micromechanical disk, the stem, and the substrate, modeling them as an *lcr* tank, a transmission line T-network, and a resistor, respectively.

2.1. Negative Capacitive Equivalent Circuit

Figure 2.1(a) depicts a radial contour mode disk resonator in a typical bias, excitation, and detection scheme. This device comprises a 2μm-thick disk surrounded by two closely spaced (d_o=80nm) electrodes and supported by an anchored stem attached at the center of the disk, where the radial displacement is minimized in each of the mode shapes shown in Figure 2.1 (b), (c), (d), making this attachment location a quasi-nodal point ("quasi", since the stem has finite radius). To minimize transducer loss that might otherwise mask the influence of anchor loss on Q, this device employs a capacitive transducer. The device is excited into resonance via a combination of a dc-bias voltage V_P applied to the conductive
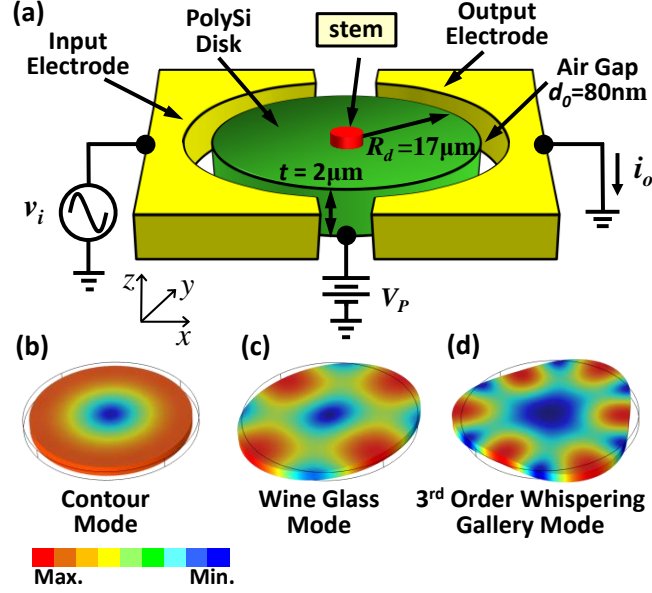
Figure 2.1: (a) Schematic of an all-polysilicon disk resonator in a two-port excitation and sensing configuration. (b) Contour mode shape. (c) Wine glass mode shape. (d) 3rd order whispering gallery mode (WGM) shape. (All simulated via FEM).
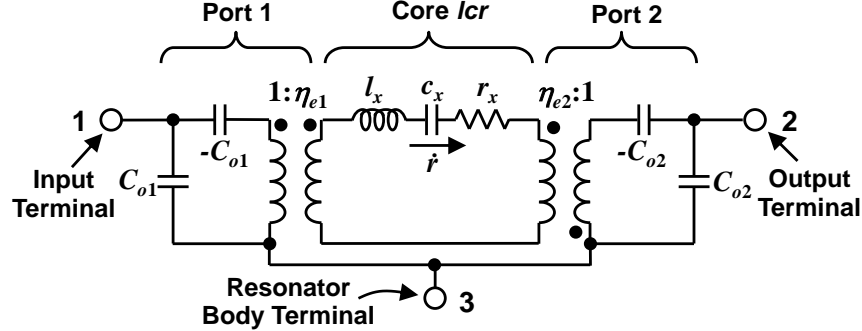
Figure 2.2: Traditional ac small-signal equivalent circuit of a 2-port radial contour mode disk resonator with r_x modeling all energy loss mechanisms, which includes anchor loss, thermal elastic damping (TED), phonon-phonon interactions and phonon-electron interactions.

polysilicon resonant structure and an ac signal v_i applied to the input electrode, which together induce a force at the frequency of v_i that drives the disk into resonance vibration when the frequency of v_i matches the resonance frequency. Once vibrating, the V_P-biased time varying capacitance between the disk and its output electrode generate an output current detectable by measurement instrumentation [11].

To conveniently model and simulate the behavior of micromechanical radial contour mode disk resonators in a way that facilitates circuit analysis, Figure 2.2 shows an ac small-signal electrical equivalent circuit of a capacitive-gap resonator, which includes a core *lcr* tank to model the mechanical vibration, a pair of transformers to represent the electromechanical coupling, and negative capacitances to model the dependence of
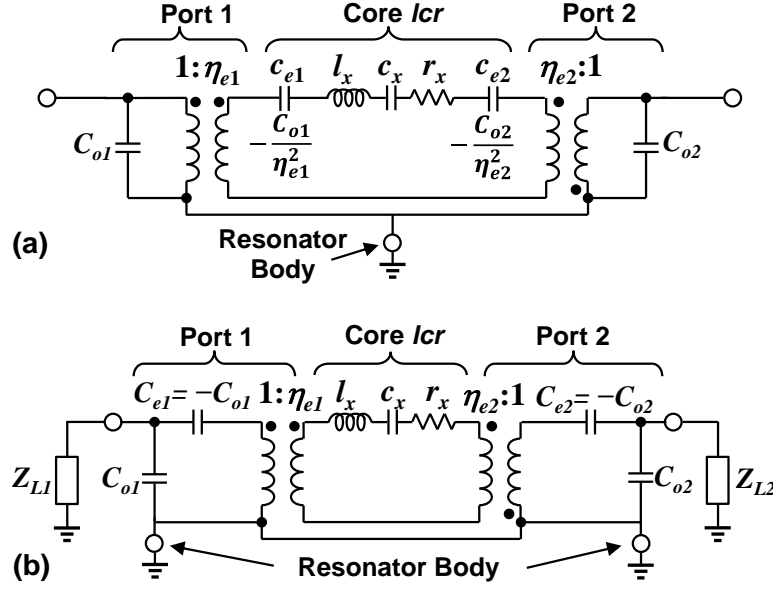
Figure 2.3. Negative capacitance small-signal equivalent circuits for a two-port capacitive-gap micromechanical contour mode disk resonator: (a) Negative capacitance equivalent circuit with electrical stiffness separated from mechanical stiffness. (b) Negative capacitance equivalent circuit with electrical stiffness reflected through transformers to outside the core *lcr* loop.

resonance frequency on electrical stiffness.

To capture the influence of electrical stiffness more clearly, this improved equivalent circuit models the electrical stiffness and mechanical stiffness separately, instead of lumping them all together as shown in Figure 1.15. In general, a spring with stiffness k in mechanical domain can be modeled as a capacitor in electrical domain with values of $1/k$. Parallel combination of stiffness corresponds to series connection of capacitors in an equivalent electrical circuit. To attain the circuit of Figure 2.2, we start with the circuit of Figure 1.15 and first separate c_r into three capacitors: $c_x = 1/k_m$ to model the mechanical stiffness of the resonator structure, and two negative capacitors c_{ei} to model electrical stiffnesses generated at the i port as shown in Figure 2.3(a), which takes the following form:

$$c_{ei} = -\frac{1}{k_{e,i}} = -\frac{d_o^2}{V_P^2 C_{oi}} \tag{2.1}$$

where i denotes the corresponding port. Plugging the expression of micromechanical coupling factor η_{ei} from (1.13) into (2.1) further yields the c_{ei} expression as:

$$c_{ei} = -\frac{d_o^2}{V_P^2 C_{oi}} = -\frac{C_{oi}}{\eta_{ei}^2} \tag{2.2}$$

Here, c_{ei} entirely captures the electrical stiffness, allowing c_x in Figure 2.3(a) to represent purely mechanical stiffness. Further reflecting the negative capacitors c_{ei} through the transformers to outside the core *lcr* loop yields C_{ei} in the circuit of Figure 2.3 (b), where

the physical shunt electrode-to-resonator capacitors C_{oi} are now matched by series negative capacitors of exactly the same values, as indicated by the following expression:

$$C_{ei} = \eta_{ei}^2 c_{ei} = -C_{oi} \tag{2.3}$$

By replacing ω_o in (1.7), (1.8), and (1.9) with nominal radial resonance frequency ω_{nom}, the l_x, c_x, and r_x in the negative capacitance equivalent circuit can be calculated using the following expressions.

$$l_x = m_m \tag{2.4}$$

$$c_r = \frac{1}{\omega_{nom}^2 m_m} \tag{2.5}$$

$$r_x = \frac{\omega_{nom} m_m}{Q} \tag{2.6}$$

Note that the resonance frequency dependency on dc-bias voltage V_P of a radial contour mode disk resonator is now entirely captured by the electromechanical coupling coefficients η_{ei}. Thus, no arrow is needed through the motional capacitor, as needed in the conventional circuit of Figure 1.15. More importantly, the value of the core c_x element stays constant, as it should. The negative C_{oi} is also a static capacitor, just like the positive C_{oi} of the physical shunt electrode-to-resonator capacitance. As shown in the circuit, the physical shunt electrode-to-resonator capacitors C_{oi} are now matched by series negative capacitors of exactly the same values, which will provide very important insights to capture the frequency dependence characteristics of micromechanical resonators [27]. With this circuit, by mere inspection, a designer can now immediately see that the shunt C_{oi} presents the opportunity to effectively negate the electrical stiffness, which will be analyzed in details in Chapter 4.

2.2. Limitations of Traditional Equivalent Circuit

Although the negative capacitance equivalent circuit in Figure 2.2 has already improved from the conventional equivalent circuit and can adequately predict the performance of a contour mode disk resonator such as resonance frequency and motional resistance, it still hides very important insights on how anchor geometries affect quality factor and cannot capture the anchor loss limited Q. In particular, it models the device's quality factor via a resistor r_x, which represents all energy loss mechanisms responsible for limiting the Q of micromechanical resonators, including gas damping, anchor loss, thermoelastic dissipation (TED), phonon-phonon interaction and phonon-electron interaction [13]. In such equivalent circuit, the r_x value is usually back calculated by first measuring the quality factor of the device and then plugging the measured Q's in the equation below:

$$r_x = \frac{\omega_o l_x}{Q} \qquad (2.7)$$

where ω_o is the angular resonance frequency, l_x represents the dynamic mass and Q is the measured quality factor. By lumping all energy dissipation from different loss mechanisms into a single resistor r_x, such circuit does not convey clearly to a designer the impact of anchor loss on the overall device quality factor, which usually dominates among all loss mechanisms in our cases [11] [26].

2.3. Equivalent Circuit Modeling of Anchor Loss

To remedy the above deficiencies, this work introduces a more insightful equivalent circuit model that can capture the influence of stem geometries on anchor loss and predict the anchor loss dominated Q for radial contour mode disk resonators. For a center supported micromechanical disk resonator, the motion in stem causes substrate vibration and generates dissipation of vibration energy through substrate. As shown in the cross section of a radial contour mode disk resonator in Figure 2.4, expansion and contraction of the disk in radial direction will generate vertical displacement on the bottom surface due to Poisson ratio of the structure material. Such vertical displacement maximizes at the center of bottom surface and applies an ac harmonic force on the substrate via the stem, causing vibration in the substrate and generating energy dissipation. To model such energy loss via the stem to the substrate, the new equivalent circuit shown in Figure 2.5 separates the micromechanical disk, the stem, and the substrate, modeling them as a new *lcr* tank, a transmission line T-network, and a resistor, respectively.

2.3.1. Resistor r_o in *lcr* Tank

As the new *lcr* tank in Figure 2.5 exclusively models the disk structure without including the stem or substrate, the resistor r_o only represents non-dominating energy dissipations contributed by sources other than anchor loss, while leaving anchor loss modeling to the transmission line T-network and substrate resistor. In general, a "parallel" combination of Q_i's contributed by different loss mechanisms sets the total Q of a given micromechanical disk resonator, as shown in the following expression:

$$\frac{1}{Q} = \sum_i \frac{1}{Q_i} = \frac{1}{Q_{anc}} + \frac{1}{Q_o} \qquad (2.8)$$

where i indicates the loss mechanism, Q_{anc} stands for the anchor loss limited quality factor, and Q_o represents the intrinsic quality factor contributed by all other energy dissipations, such as thermoelastic damping (TED), phonon-phonon interactions and phonon-electron interactions (Here, gas damping is neglected because devices are tested in vacuum).
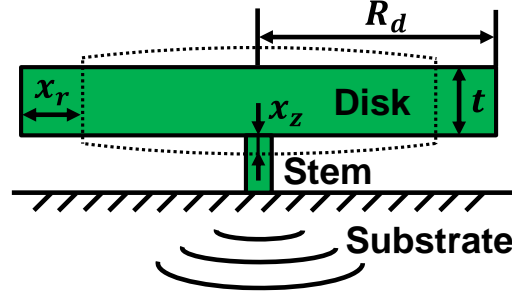
Figure 2.4: Cross sectional view of a micromechanical radial contour mode disk resonator, which illustrates vibration energy dissipation from the disk to the substrate via stem due to Poisson effect from the contour mode vibration.
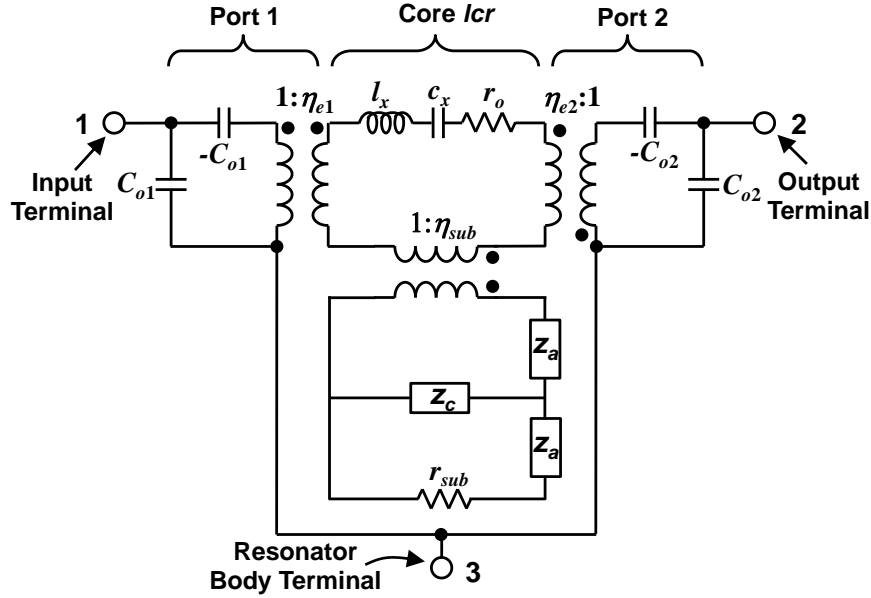
Figure 2.5: The new ac small-signal equivalent circuit of a 2-port radial contour mode disk resonator. Here, the *lcr* tank represents the mechanical disk structure, the transmission line T-network models the stem, and the substrate resistor r_{sub} represents the energy loss to the substrate.

Although TED may set the intrinsic material quality factor for low frequency flexural-mode beam resonators [28], at higher frequencies for RF applications, phonon-phonon interactions replace TED as the dominant intrinsic material loss mechanism. For sub-GHz polycrystalline silicon disk resonators in this work, quality factor limited by phonon-phonon interactions in Akheiser regime (Q_{php}) primarily determines the intrinsic quality factor (Q_o) [13]. The $f \cdot Q_{php}$ product for polysilicon disk resonators in the frequency range below 1 GHz takes the following expression [29]:

$$f \cdot Q_{php} = \frac{\rho V_a^2 (1 + (\omega\tau)^2)}{C_v T \gamma^2 \tau} \tag{2.9}$$

where ρ is the material density, V_a is the acoustic velocity, C_v represents the volumetric heat capacity, ω is the radian frequency of interest, T is the temperature in Kelvin, τ represents the phonon mean free path [29], and γ is the Gruneisen parameter with value around 1 for silicon [30]. For the 155-MHz polysilicon contour mode disk resonator which will be discussed later in this section, the intrinsic material quality factor Q_o can be obtained by plugging the $f \cdot Q_{php}$ product value of $1.72{\times}10^{13}$ calculated from (2.9) into the following equation:

$$Q_o = \frac{f \cdot Q_{php}}{f_o} = \frac{1.72 \times 10^{13}}{155 \times 10^6 \text{Hz}} \approx 1.11 \times 10^5 \tag{2.10}$$

In the new *lcr* tank in Figure 2.5, l_x and c_x take the same expressions as (2.4) and (2.5), while the resistor r_o takes a different form as follows:

$$r_o = \frac{\omega_{nom} l_x}{Q_o} \tag{2.11}$$

where ω_{nom} is the angular resonance frequency with zero-dc-bias voltage, l_x represents the dynamic mass for the resonator being modeled at the core *lcr* location, and Q_o is the intrinsic quality factor limited by phonon-phonon interactions that can be calculated from (2.10). By using intrinsic Q_o to obtain the element value of r_o in the new *lcr* tank, the equivalent circuit in Figure 2.5 separates the anchor loss from total energy dissipations by lumping material intrinsic loss into a single resistor r_o while employing a transmission T-network and a substrate resistor to capture the anchor loss magnitude.

2.3.2. Transmission Line T-Network for Stem

The new equivalent circuit models the stem of a micromechanical disk resonator as a mechanical coupling beam connecting the disk and the substrate. Because an ac harmonic force generated by Poisson effect from the disk applies on the stem and excites it into vibration in the vertical direction, the stem behaves as a vertical mechanical coupling beam vibrating in its extensional direction. In general, a coupling beam can be modeled as an acoustic transmission line—the mechanical analog to the familiar electrical transmission line that takes the following expression:

$$\begin{bmatrix} F_1 \\ \dot{X}_1 \end{bmatrix} = \begin{bmatrix} cos(\alpha l) & jZ_m sin(\alpha l) \\ \dfrac{jsin(\alpha l)}{Z_m} & cos(\alpha l) \end{bmatrix} \begin{bmatrix} F_2 \\ \dot{X}_2 \end{bmatrix} \tag{2.12}$$

where F_i and $\dot{X}_i$ are the force and velocity at corresponding ports, l is the length of the coupling beam. Z_m and α in (2.12) are acoustic characteristic impedance and acoustic wave propagation constant, respectively, which take the form:

Mechanical Coupler

$$\begin{bmatrix} F_1 \\ \dot{X}_1 \end{bmatrix} = \begin{bmatrix} cos(\alpha l) & jZ_m sin(\alpha l) \\ \dfrac{jsin(\alpha l)}{Z_m} & cos(\alpha l) \end{bmatrix} \begin{bmatrix} F_2 \\ \dot{X}_2 \end{bmatrix}$$

Electrical Transmission Line

$$\begin{bmatrix} v_1 \\ i_1 \end{bmatrix} = \begin{bmatrix} cos(\beta l) & jZ_o sin(\beta l) \\ \dfrac{jsin(\beta l)}{Z_o} & cos(\beta l) \end{bmatrix} \begin{bmatrix} v_2 \\ i_2 \end{bmatrix}$$
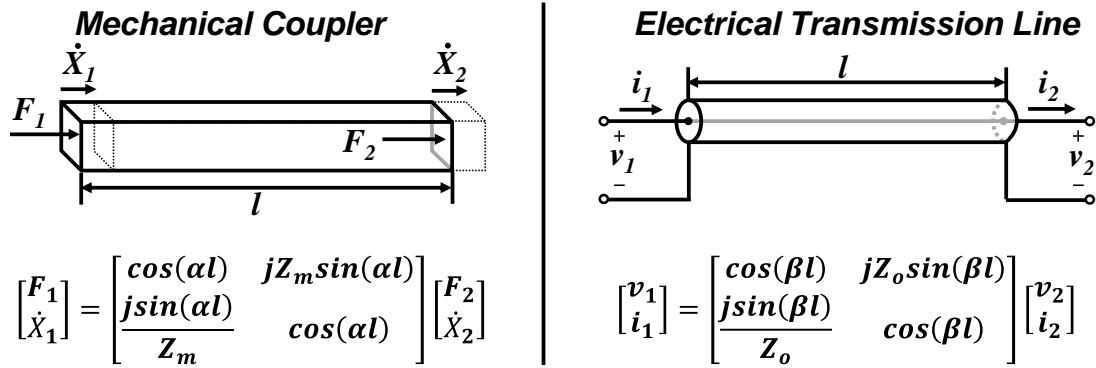
Figure 2.6: Two-port modeling of a mechanical acoustic coupling beam in analogy to an electrical transmission line.
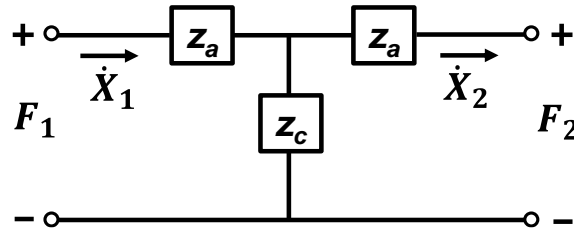
Figure 2.7: T-network modeling of a mechanical acoustic coupling beam with the force (F_i) in analogy to a voltage in electrical domain and the velocity ($\dot{X}_i$) in analogy to a current in electrical domain.

$$\alpha = \frac{\omega}{\sqrt{E_S/\rho_S}}, Z_m = A_s\sqrt{E_s\rho_s} \tag{2.13}$$

where ω is the radian frequency of the acoustic wave, ρ_s is the stem material density, E_s is the Young' Modulus of the stem material, and A_s is stem cross sectional area.

By matching force (F) and velocity ($\dot{X}$) in mechanical domain to voltage (v) and current (i) in electrical domain, Figure 2.6 presents the duality between an acoustic coupling beam and an electrical transmission line. Because the two port modeling of an electrical transmission line can be simplified by using an impedance T-network, a similar transformation can also apply on the mechanical acoustic transmission line, which generates a simplified impedance T-network model as shown in Figure 2.7 [16], with series impedance z_a and shunt impedance z_c taking the following form:

$$z_a = jA_s\sqrt{E_s\rho_s}\, tan\left(\frac{\omega}{\sqrt{E_s/\rho_s}} \cdot \frac{l}{2}\right) \tag{2.14}$$

$$z_c = A_s\sqrt{E_s\rho_s}/j\, sin\left(\frac{\omega}{\sqrt{E_s/\rho_s}} \cdot l\right) \tag{2.15}$$

2.3.3. Displacement Transformer η_s

Because the stem attaches to center of the disk's bottom surface, which is different from the perimeter of the disk where the core lcr tank is derived, a displacement transformer η_s shown in Figure 2.5 needs to take account for the difference between vertical displacement x_z at the disk's bottom surface center and radial displacement x_r at the perimeter of the disk. The radial displacement x_r in a contour mode vibration at the perimeter of a disk resonator takes the form [31]:

$$x_r = u_r(R_d) = AhJ_1(hR_d) \tag{2.16}$$

where A is a driving force dependent coefficient [31], $J_n(x)$ is the Bessel function of the first kind of order n, R_d is the disk radius, and h is a constant defined by (1.6).

The integration of vertical strain ϵ_z over disk thickness will give vertical displacement x_z at the disk's bottom surface. The vertical strain ϵ_z in a disk resonator takes the following expression [32]:

$$\epsilon_z = -\frac{v_d}{E_d}(\sigma_{rr} + \sigma_{\theta\theta}) \tag{2.17}$$

where v_d is Poisson ratio of the disk, E_d is the disk's Young's modulus, σ_{rr} and $\sigma_{\theta\theta}$ are normal stress toward the radial and circumferential directions, respectively, which can be expressed as:

$$\sigma_{rr} = \frac{E_d}{1 - v_d^2}\left(\frac{\partial u_r}{\partial r} + v_d \frac{u_r}{r}\right) \tag{2.18}$$

$$\sigma_{\theta\theta} = \frac{E_d}{1 - v_d^2}\left(v_d \frac{\partial u_r}{\partial r} + \frac{u_r}{r}\right) \tag{2.19}$$

where u_r is the time harmonic radial displacement in radial contour-mode vibration. Substituting (2.18), (2.19) into (2.17) yields the vertical strain ϵ_z at any radial location r as:

$$\epsilon_z(r) = -\frac{v_d}{1 - v_d} A[h^2 J_o(hr)] \tag{2.20}$$

As the stem radius ($R_s \leq 1\mu m$) is significantly smaller than the disk radius ($R_d = 17\mu m$ for the disk resonators used in this chapter), variations in vertical strain within the stem clamp region may be negligible. Figure 2.8 presents the normalized vertical strain $\epsilon_z(r)$ on the disk's bottom surface as a function of radial location r/R_d. The vertical strain within the stem clamp region ($r \leq R_s$) varies less than 0.3%, which is small enough to assume uniform vertical strain distribution in the stem clamp region. Therefore, integrating the vertical strain $\epsilon_z(0)$ over thickness yields the average vertical displacement x_z in the stem clamp region as:
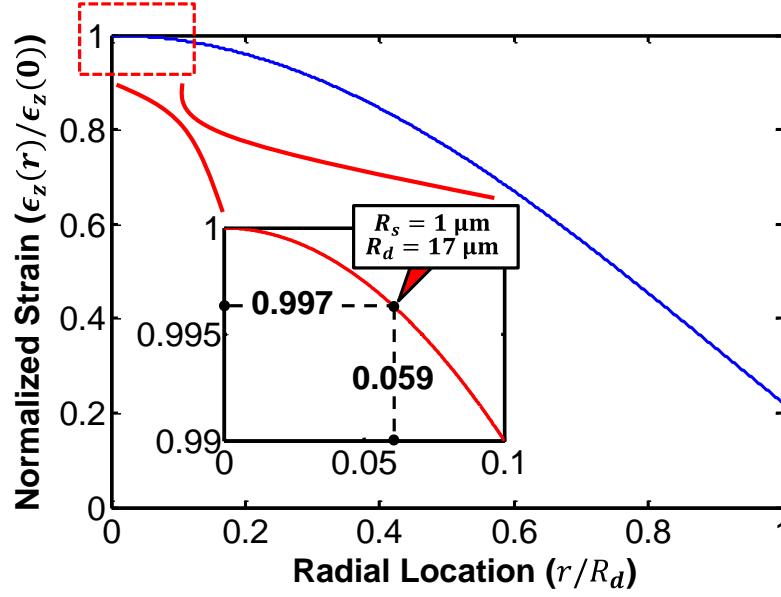
Figure 2.8: The vertical strain on the surface of a disk (normalized to the maximum vertical strain at the surface center of the disk) as a function of radial location for a 17μm-radius contour mode disk resonator with 1μm-radius stem. The zoom-in view indicates very small vertical strain variation in the stem clamp region.

$$x_z(r \le R_s) \approx \int_0^{-\frac{t}{2}} \epsilon_z(0) dz = \frac{v_d}{1 - v_d} A[h^2 J_o(0)] \cdot \frac{t}{2} \tag{2.21}$$

where t is the thickness of the disk. Combining (2.16) and (2.21), the displacement transformer turn ratio η_s takes the form:

$$\eta_s = \frac{x_r}{x_z} = \frac{J_1(hR_d)}{\frac{v_d}{1 - v_d} \cdot \frac{t}{2} [hJ_o(0)]} \tag{2.22}$$

2.3.4. Substrate Resistor r_{sub}

The stem of a radial contour mode disk resonator acts as a longitudinal rod and transfers the Poisson effect induced vertical vibration from the disk structure to the substrate surface, which excites elastic waves propagating into the substrate and dissipates energy. Indicated by the analogy between a mechanical vibration system and an electrical circuit, such energy dissipation can be modeled as a resistor r_{sub}, which takes the following expression:

$$r_{sub} = \frac{1}{2} \cdot \frac{V_{sub,e}^2}{P_{sub,e}} = \frac{1}{2} \cdot \frac{F_{sub,m}^2}{E_{sub,m}/T_m} \tag{2.23}$$
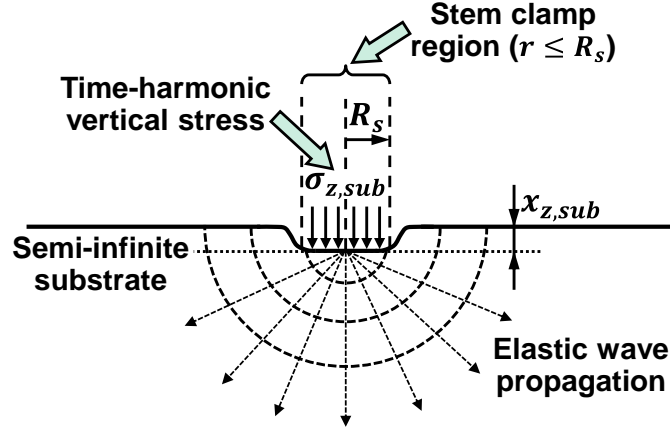
Figure 2.9: Illustration of anchor loss mechanism for a center supported contour mode disk resonator. Here, the time-harmonic vertical stress in the stem clamp region generates elastic wave propagation and causes energy dissipation to the semi-infinite substrate.

where $P_{sub,e}$ represents the electrical power consumption of a resistor, $V_{sub,e}$ is the ac voltage amplitude, $F_{sub,m}$ is the sinusoidal mechanical force amplitude applied on the substrate by the stem, $E_{sub,m}$ stands for the mechanical strain energy dissipated into the substrate in one cycle of vibration, and T_m represents the period of the elastic wave.

To quantify the magnitude of anchor loss, the substrate is modeled as a semi-infinite medium through which elastic waves propagate to infinity and will not reflect back to the resonator [32]. As illustrated in Figure 2.9, the longitudinal vibration in the stem will apply an evenly distributed time-harmonic stress $\sigma_{z,sub}$ on the substrate surface and generate vertical displacement $x_{z,sub}$. The sinusoidal mechanical force $F_{sub,m}$ applied in stem clamp region takes the form as follows:

$$F_{sub,m} = \sigma_{z,sub} \cdot A_s = \sigma_{z,sub} \cdot \pi R_s^2 \tag{2.24}$$

Integrating the product of stress and its corresponding displacement in the stem clamp region gives the mechanical strain energy $E_{sub,m}$ in one cycle of vibration:

$$E_{sub,m} = \pi \int_0^{R_s} \sigma_{z,sub} x_{z,sub} 2\pi r dr \tag{2.25}$$

By using 3D elastic wave equations and their Hankel transforms, the vibration displacement $x_{z,sub}$ can be expressed in terms of $\sigma_{z,sub}$ as [19]:

$$x_{z,sub} = \sigma_{z,sub} R_s^2 \frac{c_L \omega}{2\rho c_T^4} \Pi(\gamma) \tag{2.26}$$

where c_L and c_T are the longitudinal and transverse wave propagation velocities in the substrate, respectively, and $\Pi(\gamma)$ represents the imaginary part of an integral constant which mainly depends on c_L/c_T [33]. By combing (2.25) and (2.26), the energy loss caused by elastic wave propagation into the substrate take the following form:

$$E_{sub,m} = \pi^2 \sigma_{z,sub}^2 R_s^4 \cdot \frac{c_L \omega}{2\rho c_T^4} \Pi(\gamma) \qquad (2.27)$$

Combining Equation (2.23), (2.24), and (2.27) finally yields the expression of the substrate resistor for a radial contour mode disk resonator:

$$r_{sub} = \frac{2\pi\rho c_T^4}{c_L \omega^2 \Pi(\gamma)} \qquad (2.28)$$

Chapter 3 Hollow Stem Disk Resonators

As described in Chapter 2, anchor dissipation via the disk resonator's stem structure dominates the energy loss and therefore limits Q. An obvious way for Q-enhancement is to shrink the stem size to reduce its cross-sectional area and thereby reduce the conduit through which energy can pass from the vibrating disk structure to the substrate. In particular, by reducing stem sizes from 2.0 μm to 1.6 μm, [11] showed a measured Q increase from 5,551 to 14,657 for 405-MHz radial-contour mode disk resonators. In keeping with several theoretical studies in the literature [20] [21] [34], even higher Q's are expected as stem diameters decrease to submicron dimensions.

Unfortunately, there are of course practical barriers to continued scaling of stem diameters. First, as a stem is thinned, its support strength wanes, so there is a minimum stem diameter and length that can support a disk of a given size. Second, even if a stem maintains sufficient strength while scaled to nanometer dimensions, the need to not only form it, but also place it exactly at the disk center, poses fabrication challenges.

The novel idea of hollow stem approach as shown in Figure 3.1 circumvents the above issues by employing a hollow cylinder with thin walls, rather than a single thin solid stem [26]. Since the walls are thin, the cross-sectional area of the stem is still very small. However, as with all hollow cylinders (e.g., pipes, lances, etc.), it still retains much of the strength of a full stem with the same diameter, as summarized by the comparison analysis in Figure 3.1.
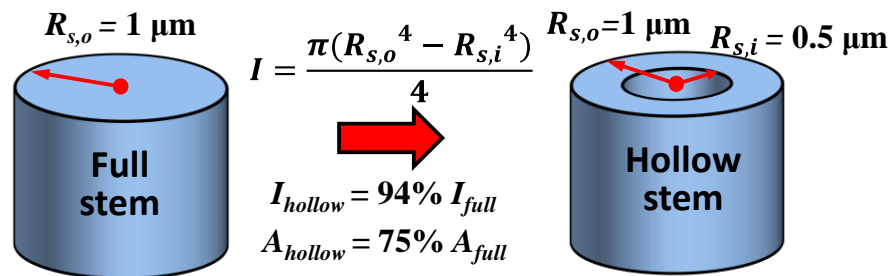
Figure 3.1: Comparison of the bending strength (Second Moment of Inertia I) and the cross sectional area between a full stem with radius of 1 μm and a hollow stem with same outer radius but inner radius of 0.5μm.
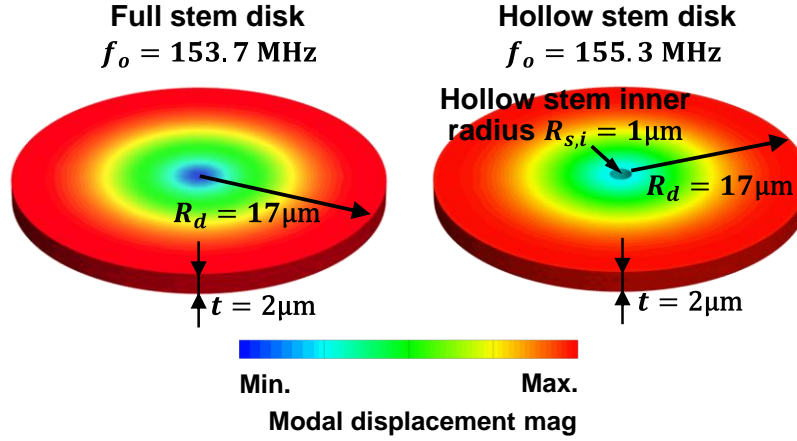
Figure 3.2: FEA mode shape simulation of a conventional disk and a hollow disk with 1μm radius hole in the center. Here, both disks have the same radius of $R_d = 17$μm and thickness of $t = 2$μm.

3.1. Hollow Stem Disk Resonator Equivalent Circuit

For the range of radii of the disks and stems used in this dissertation, replacing the full stem with a hollow stem subtracts very little material such that the change in effective mass and stiffness of the first radial contour mode is negligible. It follows that the resonance frequency and mode shape of the hollow stem disk would be only slightly different than its full stem counterpart. Finite element analysis (FEA) performed on disks with a 17 um radius and 2 um thickness in Figure 3.2 verifies this expectation, and shows the first radial contour modes at 155.3 MHz and 153.7 MHz for the full stem and hollow stem disks, respectively. This difference, caused by the absence of a 1 um radius stem material, is smaller than 1%, trivial enough that the same *lcr* tank model can be shared by both types of disks for calculating the resonance frequency. The FEA result also indicates that the vertical displacement x_z in the stem clamp region and the radial displacement x_r on the perimeter are comparable for both disks, as highlighted by Table I, implying that the displacement transformer turns ratio η_s calculated by (2.22) will also be similar for both types of disks. All these results point to the fact that a hollow disk can share the same equivalent *lcr* tank model and displacement transformer with a full disk.

To apply the new equivalent circuit model on a hollow stem disk resonator requires modification on the transmission line T-network of a full stem discussed in Chapter 2. The

Table I: Comparison of modal displacement for conventional disk and hollow disk with 1 μm radius hole in the center

	Modal displacement		η_s	Resonance frequency (MHz)
	x_z	x_r		
Full disk	0.0590	0.990	16.78	155.3
Hollow disk	0.0593	0.991	16.71	153.7
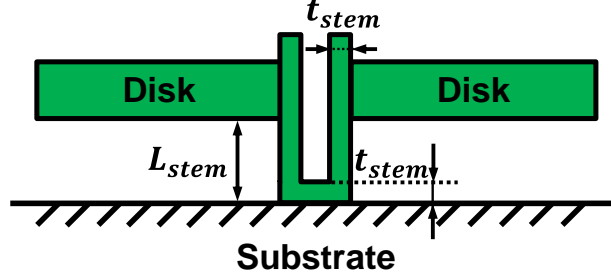
Figure 3.3: Schematic cross sectional view of a hollow stem disk resonator fabricated by using self-aligned stem fabrication process [11].
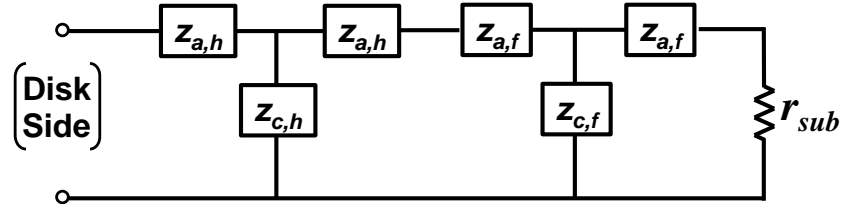
Figure 3.4: Small signal equivalent circuit of a fabricated hollow stem attached to a silicon substrate using similar fabrication process in [11]. The two transmission line T-networks in series model the hollow part and solid part of a self-aligned hollow stem structure. The resistor r_{sub} represents the silicon substrate.

hollow stem is generated by partially refilling a stem hole in the disk structure with a very thin layer of polysilicon material (which will be discussed in more details in section 5.4). As shown in the cross section view of Figure 3.3, a fabricated hollow stem structure will actually have two parts: a hollow pipe on the top that is connected to the disk, and a solid stem portion at the bottom attached to the substrate. Therefore the equivalent circuit model of a fabricated hollow stem should include the transmission line T-network models for both portions in series, as shown in Figure 3.4.

By applying the approximation of a thin shell under axial excitations, the hollow pipe transmission line T-network impedances take the following expressions [35]:

$$z_{a,h} = jA_h\sqrt{E_s\rho_s} \; tan\left(\frac{\omega}{\sqrt{E_s/\rho_s}} \cdot \frac{L_{stem} - t_{stem}}{2}\right) \tag{3.1}$$

$$z_{c,h} = A_h\sqrt{E_s\rho_s}/j \; sin\left(\frac{\omega}{\sqrt{E_s/\rho_s}} \cdot (L_{stem} - t_{stem})\right) \tag{3.2}$$

where L_{stem} is total length of the hollow stem structure, t_{stem} is the hollow stem wall thickness, as indicated in Figure 3.3, and A_h is the cross sectional area of the hollow pipe part, which takes the form:

$$A_h = 2\pi\left(R_{s,o} - \frac{t_{stem}}{2}\right)t_{stem} \tag{3.3}$$
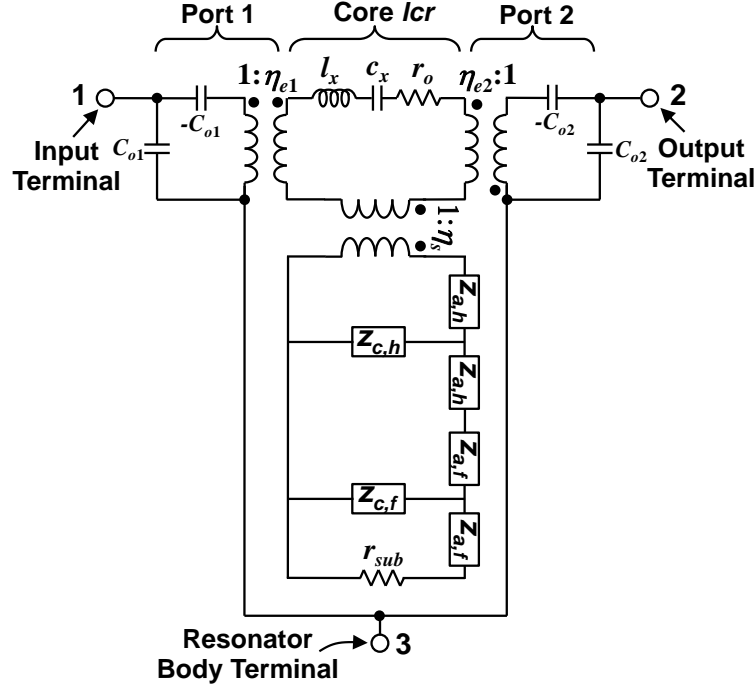
Figure 3.5: The new ac small-signal electrical equivalent circuit of a hollow stem radial contour mode disk resonator.

where $R_{s,o}$ represents the outer radius of the hollow stem structure. For the bottom solid stem part which directly connects to the substrate, the T-network impedances can be calculated as:

$$z_{a,f} = jA_f\sqrt{E_s\rho_s}\, tan\left(\frac{\omega}{\sqrt{E_s/\rho_s}} \cdot \frac{t_{stem}}{2}\right) \tag{3.4}$$

$$z_{c,f} = A_f\sqrt{E_s\rho_s}/j\, sin\left(\frac{\omega}{\sqrt{E_s/\rho_s}} \cdot t_{stem}\right) \tag{3.5}$$

where $A_f = \pi R_{s,o}^2$ is the cross sectional area of the full stem part. Replacing the transmission line T-network model of a full stem with that of a hollow stem generates a complete equivalent circuit model for a hollow stem contour mode disk resonator, as shown in Figure 3.5, which can capture the magnitude of energy dissipation through the disk stem and predict anchor loss limited Q.

The hollow stem resonators are fabricated on a N-type <100> silicon wafer with thickness of 625μm, which is much larger than the typical dimensions of a hollow stem disk resonator and thereby can be considered as a semi-infinite medium with no acoustic waves reflected back. Plugging the material properties of N-type <100> silicon into (2.28) will give the numerical value of the substrate resistor r_{sub}, which represents the energy loss in the silicon substrate.

Table II: Comparison of design variables and equivalent circuit element values for 155-MHz hollow stem contour mode disk resonators with different stem wall thickness

	Parameter	Source	Hollow Stem		Solid Stem	Units
Design Variables	Disk Radius, R_d	Layout	17	17	17	μm
	Hollow Stem Outer Radius, $R_{s,o}$	Layout	1	1	1	μm
	Stem Inner Radius, $R_{s,i}$	Fabrication	0.8	0.5	N/A	μm
	Stem Wall Thickness, t_{stem}	Fabrication	0.2	0.5	N/A	μm
	Resonance Frequency, f_o	(1.18)	155.4	155.4	155.4	MHz
	Electrode Span Angle, θ	Layout	156	156	156	(°)
	Disk Thickness, t	Fabrication	2	2	2	μm
	Intrinsic Quality Factor, Q_o	(2.10)	111,000	111,000	111,000	N/A
	Electrode-to-Resonator Gap, d_o	Fabrication	80	80	80	nm
	DC Bias Voltage, V_P	N/A	5	5	5	V
Equivalent Circuit Elements	Equivalent Inductance, l_x	(1.5), (1.7)	3.1868×10^{-12}	3.1868×10^{-12}	3.1868×10^{-12}	H
	Equivalent Capacitance, c_x	(2.5)	3.2936×10^{-7}	3.2936×10^{-7}	3.2936×10^{-7}	F
	Equivalent Resistance, r_o	(2.11)	2.8023×10^{-8}	2.8023×10^{-8}	2.8023×10^{-8}	Ω
	Overlap Capacitance, $C_{o1} = C_{o2}$	[11]	10.245	10.245	10.245	fF
	Electromechanical Coupling, $\eta_{e1} = \eta_{e2}$	(1.13)	6.4034×10^{-7}	6.4034×10^{-7}	6.4034×10^{-7}	N/A
	Displacement Ratio, η_s	(2.22)	16.77	16.77	16.77	N/A
	Characteristic Impedance, $Z_{m,h}$	(2.13)	2.1007×10^{-5}	4.3764×10^{-5}	N/A	Ω
	Characteristic Impedance, $Z_{m,f}$	(2.13)	5.8352×10^{-5}	5.8352×10^{-5}	5.8352×10^{-5}	Ω
	Hollow Stem Impedance, $z_{a,h}$	(3.1)	6.3495×10^{-7}j	5.2899×10^{-7}j	-1.058×10^{-6}j	Ω
	Hollow Stem Impedance, $z_{c,h}$	(3.2)	-3.4782×10^{-4}j	-0.0018j	0.0016j	Ω
	Solid Stem Impedance, $z_{a,f}$	(3.4)	7.0532×10^{-7}j	1.7637×10^{-6}j	3.5307×10^{-6}j	Ω
	Solid Stem Impedance, $z_{c,f}$	(3.5)	-0.0024j	-9.6616×10^{-4}j	-4.8396×10^{-4}j	Ω
	Equivalent Substrate Resistance, r_{sub}	(2.28)	0.0068	0.0068	0.0068	Ω
	Predicted Quality Factor	Equivalent Circuit	40,751	13,279	11,313	N/A

3.2. Design Example

This dissertation designs several 155-MHz hollow stem contour mode disk resonators with different stem wall thicknesses and analyzes Q enhancement effect from hollow stems by using the new equivalent circuit model. Table II summarizes the design parameters, the equivalent circuit variables, and the predicted quality factors of three different resonator designs which have the same disk radius ($R_d = 17$ μm) and stem outer radius ($R_{s,o} = 1$ μm), but different hollow stem wall thicknesses. The equivalent circuit predicts that the 155-MHz polysilicon hollow stem disk resonator with 200nm wall thickness will increase the contour mode quality factor by 3.6× to 40,751, compared with its full stem counterparts, which theoretically verifies the Q-enhancement effect from hollow stems.

3.3. Fabrication Process

The fabrication process for the hollow stem devices in this work leverages heavily the self-aligned stem process of [11] that not only eliminates disk-to-stem misalignment, but also allows for different stem and disk film thickness, thereby greatly facilitating manufacture of hollow stems. The process begins with layer depositions and patternings (where appropriate) for the substrate ground plane and contacts (not shown), polysilicon interconnects, bottom sacrificial layer, and structural polysilicon capped by an oxide etch hard mask, all identical to those used in [11]. Like [11], instead of using an anchor mask to first define the stem then another mask aligned to the first to define the disk structure, this process defines both the stem hole position and the disk edges all in one mask, effectively eliminating the possibility of stem misalignment. This maximizes the Q of the ensuing device, since it allows centering of the stem precisely at the disk nodal location. After the single-mask lithography defining the disk and stem hole, the doped polysilicon structural layer is patterned through the oxide hard mask, then a sacrificial sidewall spacer oxide (to define the gap) is deposited via LPCVD to yield the cross-section of Figure 3.6(a).
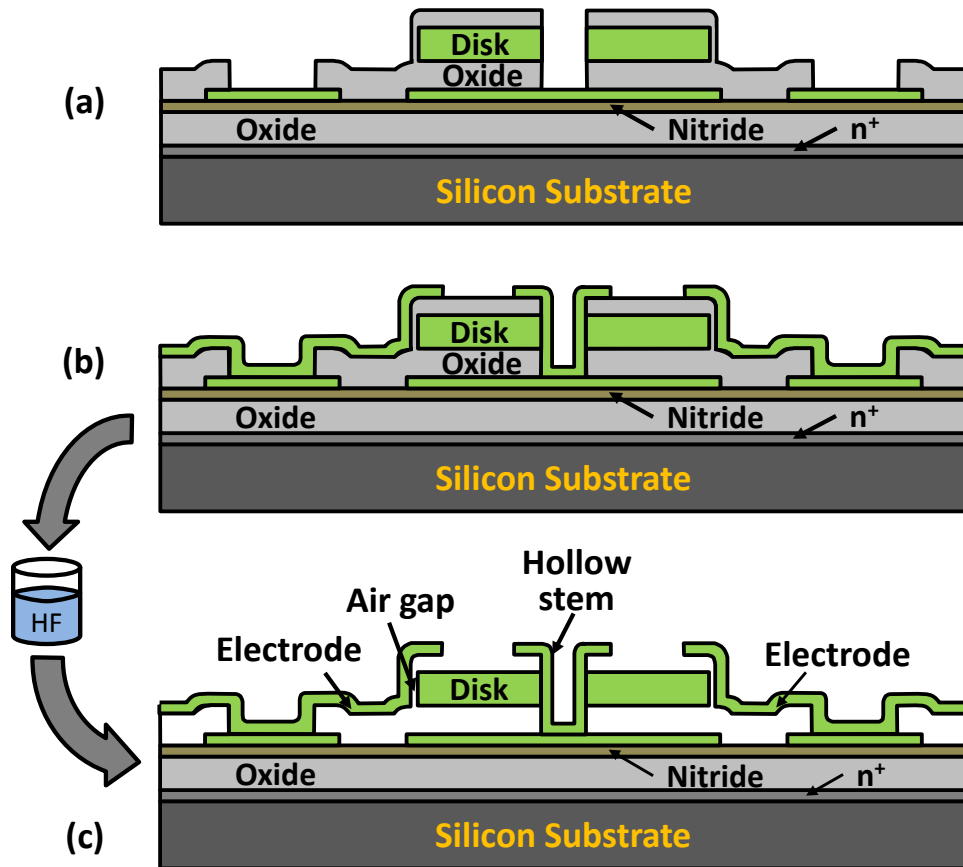
Figure 3.6: Cross-sections showing the last few steps in the fabrication process for hollow stem, small-lateral-gap, all-polysilicon disk resonators.
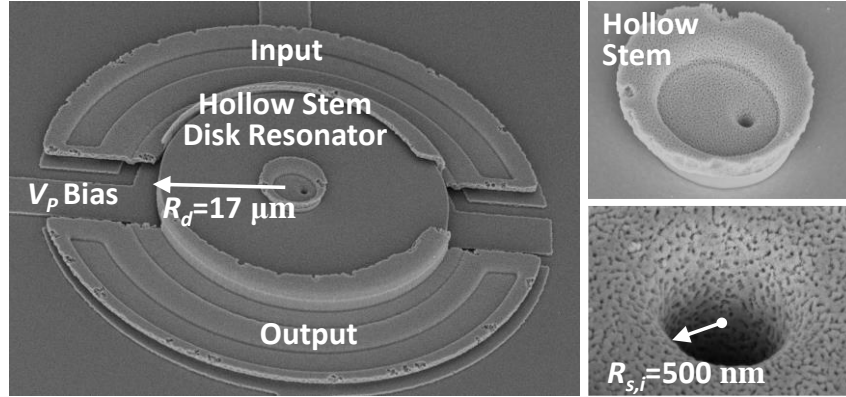
Figure 3.7: SEM's of a fabricated polysilicon hollow stem disk resonator with zoom-in's to its hollow stem structure. The halo around the hollow stem results from over etch of the oxide hard mask when etching the stem via.

At this point, the process flow deviates from that of [11]. In particular, instead of depositing a 2μm thick polysilicon to fully refill the 1μm~3μm diameter stem holes, as was done previously, a very thin layer (less than 500nm) insufficient to refill the stem holes is deposited via LPCVD at 585℃ followed by $POCl_3$ doping. The conformity of LPCVD polysilicon allows the film to follow the contours of the stem hole, even at corners. The input electrode, output electrode and stem are then patterned by another mask lithography followed by polysilicon DRIE etching, as shown in Figure 3.6(b).

Wafers are then immersed in 49 wt. % hydrofluoric acid for ~30 min. to etch away sacrificial oxide and release the structures, leaving the final cross-section of Figure 3.6(c). Figure 3.7 presents the SEM of a fabricated device with zoom-in's on its stem, which features 500nm-thick walls in a 1μm-outer radius stem hole, resulting in a 500nm-radius hollow region. In addition to the thin-walled stem, the SEM of Figure 3.7 also shows electrodes with equally thin walls. Like the stems, the electrodes also benefit from the increased strength of a curved geometry.

3.4. *Q* Enhancement for Radial Contour Mode

To gauge the *Q*-enhancement of hollow stems and verify the efficacy of the transmission line based hollow stem equivalent electrical circuit for *Q* prediction, measurements on fabricated devices focus on comparison of conventional 1μm-radius full stem disk resonators with hollow stem disk resonators employing the same outer stem radius, but different stem wall thicknesses of 200nm and 500nm. The devices were tested using the mixing measurement method described in [22] (that allows more accurate measurement of mechanical *Q*) under a 2μTorr vacuum environment generated by a Lakeshore FWPX cryogenic probe station. Although high frequency micromechanical resonators are less susceptible to gas damping, so are able to reach *Q*'s on the order of 10,000 in air [15], vacuum is still needed to measure *Q*'s above this.
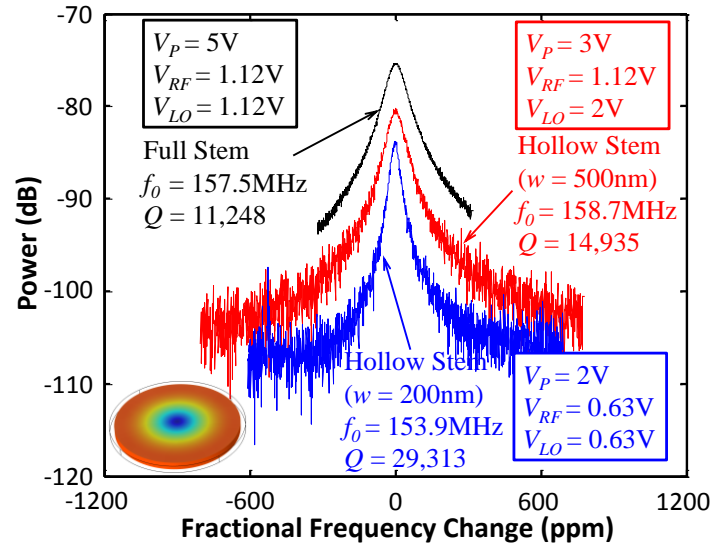
Figure 3.8: Comparison of frequency characteristics for full stem and hollow stem all-polysilicon disk resonators vibrating in the radial-contour mode.

3.4.1. Q Enhancement of Hollow Stem Support

Figure 3.8 combines the measured frequency characteristics of a full stem radial-contour mode disk resonator together with ones sporting 500nm-wall and 200nm-wall hollow stems, all with identical 17-μm radii. To facilitate interpretation of the data, Figure 3.8 plots measured output power along the y-axis against fractional frequency change relative to the resonance frequency of each device along the x-axis. Here, the 200nm-wall hollow stem device achieves a Q of 29,313 at 153.9 MHz, which is more than 2.6× higher than its identically-dimensioned full stem counterpart. The 500nm-wall hollow stem device also provides an improvement, although smaller, at about 1.3× better than the full stem case. The smaller the hollow stem wall thickness, the larger the improvement in Q, all confirming the discussion of Chapter 3.

As indicated by the dc-bias voltage values used in mixing measurements for Figure 3.8, the 200nm-wall hollow stem device could not accept voltages as large as used for the 500nm-wall hollow stem and full stem devices, since the former tended to pull into its electrodes when voltages exceeded 3V. This explains the lower peak current measured for this device despite its much higher Q. It also reveals a limitation of the hollow stem approach, where the thinner electrode over-hang shown in Figure 3.7 compromises the maximum dc-bias voltage sustainable across the electrode-to-resonator gap before pull-in in vertical direction. As mentioned in Section 3.1 and Section 3.3, although the cylindrical and curved geometries of the stem and electrodes, respectively, do help to strengthen them in the lateral direction, they seem not as strong as full stem or thicker counterparts in the vertical direction because of electrode over-hang. In the future, an improved fabrication process with CMP (chemical mechanical planarization) process that can eliminate
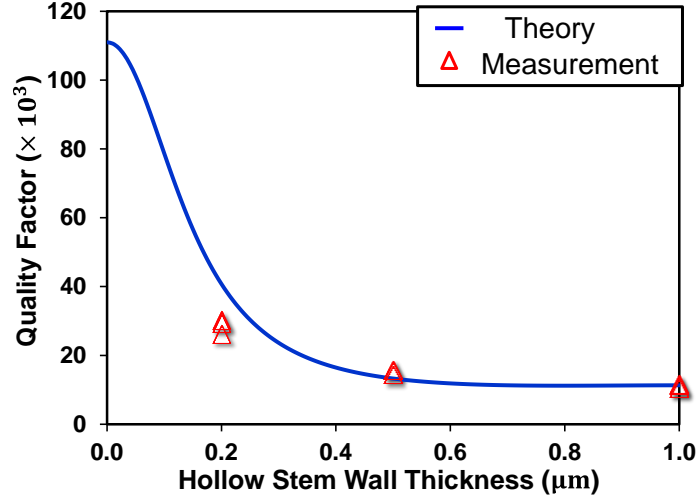
Figure 3.9: Comparison of measured Q's and predicted Q's by the new hollow stem equivalent circuit for hollow stem disk resonators with same outer stem radius ($R_{s,o} = 1\mu m$) but different stem wall thicknesses.

Table III: Quality factor values for solid stem disk resonators and hollow stem disk resonators with different stem wall thickness.

	Hollow Stem ($R_{s,o} = 1$ μm)		Solid Stem ($R_s = 1$ μm)
	Stem Wall Thickness (200nm)	Stem Wall Thickness (500nm)	
Theoretically predicted Q	40,751	13,279	11,313
Measured Q	26,169	15,834	11,556
	30,291	15,624	11,248
	29,313	14,387	10,583

electrode over-hangs would improve the vertical direction electrode strength of hollow stem devices, which can solve this electrode strength compromise and allow the same pull-in voltage for hollow stem disk resonators as its full stem counterparts.

3.4.2. Measurement vs. Theory

To demonstrate the efficacy of the hollow stem equivalent circuit model for anchor loss modeling and Q prediction, Figure 3.9 compares the theoretically predicted Q versus measured Q for hollow stem radial contour-mode disk resonators with different hollow stem wall thicknesses of 200 nm, 500 nm and 1 um, with 3 sets of measurement data points for each particular type of disk resonator. As summarized in Table III, the measured Q's for each type of resonators are very consistent and the measurement data matches quite well with theoretical prediction, especially for full stem disk resonators and hollow stem disk resonators with 500nm sidewall thickness. This indicates that the transmission line T-network based hollow stem equivalent circuit correctly captures the magnitude of anchor loss for contour-mode disk resonators.
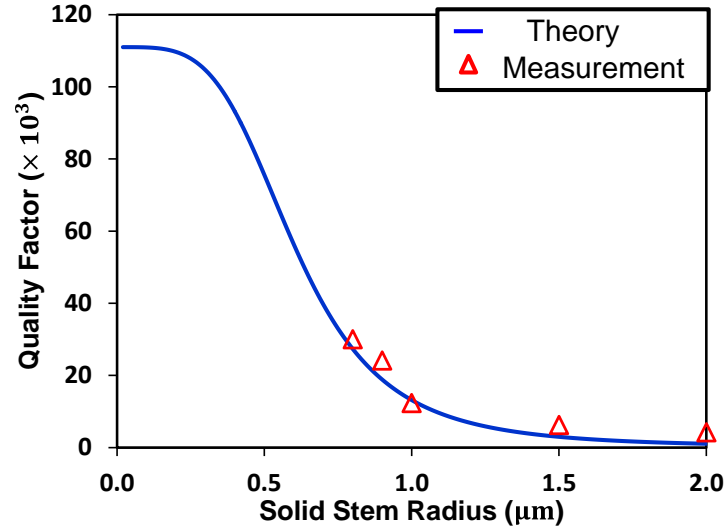
Figure 3.10: Comparison of previously measured *Q's* in [11] and theoretically predicted *Q's* by the transmission line T-network based equivalent circuit for 18μm-radius polysilicon contour-mode disk resonators with different full stem sizes.

For hollow stem disk resonators with 200 nm wall thickness, relatively large discrepancies exist between theoretical prediction and measurement data. This may be attributable to the thickness variance from the polysilicon LPCVD deposition step during stem hole refilling. As shown in the theoretical *Q* curve of Figure 3.9, a very small change in hollow stem wall thickness would result in dramatic *Q* variation if the hollow stem sidewall is very thin. For example, a 50 nm increase in hollow stem wall thickness from 200 nm to 250 nm would reduce *Q* from 40,751 to 30,331, which corresponds to a 26% change, while for thicker wall thickness changing from 500 nm to 550 nm, *Q* would only degrade from 13,279 down to 12,424, which is only a 6% difference. By accounting for the difference between target thickness and real measured thickness of the LPCVD polysilicon deposition, the discrepancies between theoretical prediction and measurement data for the 200nm wall thickness hollow stem devices may shrink, which could provide more precise predictions for hollow stem resonators with different wall thickness.

3.4.3. Quality Factor vs. Full Stem Size

The transmission line T-network based equivalent circuit also predicts very accurate *Q* for full stem devices with different stem sizes. The solid line in Figure 3.10 plots the predicted *Q's* versus stem sizes for the 18μm-radius conventional full stem polysilicon disk resonators presented in [11]. The equivalent circuit indicates a *Q* improvement from 1,100 to 27,000 when the stem radius reduces from 2 μm to 0.8 μm. The predicted *Q* enhancement trend matches well with the previously measured data points, which further validates the use of transmission line T-network based equivalent circuit to model anchor loss limited *Q*. Without the need to perform FEM simulations, such an equivalent circuit greatly eases the quality factor prediction for radial contour mode disk resonators.
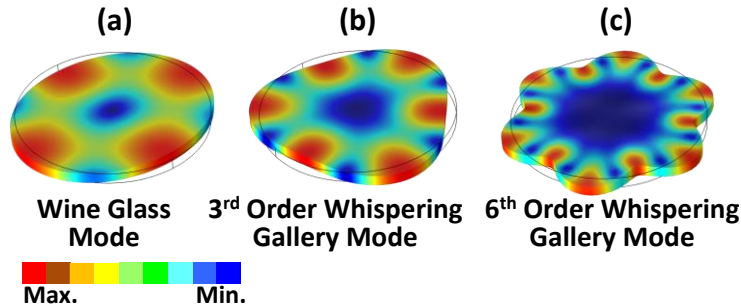
Figure 3.11: FEA mode shapes of a 17µm-radius polysilicon disk resonator. (a) Wine glass mode shape. (b) 3rd order whispering gallery mode (WGM) shape. (c) 6th order whispering gallery mode shape.

3.5. *Q* Enhancement for Other Different Mode Shapes

To gauge the degree to which hollow stem design really suppresses energy loss to the substrate, the measurements also compare their efficacies for disks vibrating in each of the mode shapes depicted in Figure 3.11(a)-(c). In particular, the FEM simulations shown actually depict displacements, where the darker the blue color, the less the displacement. A focus on the anchors reveals that whispering gallery modes, including the wine-glass mode, should allow much higher *Q*'s than radial-contour modes if anchor losses dominate. In addition, hollow stem design should be less necessary for higher whispering gallery modes if high *Q*'s are desired.

3.5.1. Wine Glass Mode

Although the input and output electrodes of the device under test are designed for radial-contour mode vibration, they are also able to excite and detect the wine glass mode depicted in Figure 3.11(a), since both modes have large vibration amplitudes centered over the output electrodes. Figure 3.12 presents a plot similar to that of Figure 3.10, but this time comparing wine glass modes for the different devices. The highest *Q* is now 45,138 at 112 MHz, again for the 200nm-wall hollow stem disk. As with the radial contour mode, the *Q*'s of the wine-glass mode also improve with decreasing hollow stem thickness, with a 2.9× improvement for the 200nm-wall hollow stem versus full stem.

3.5.2. Whispering Gallery Modes

The wine-glass mode is actually just one of the many whispering gallery modes [36] of the disk structure shown in Figure 3.11(a)-(c). In the wine-glass mode, there are two positive vibration amplitude maxima, making it a 2nd order whispering gallery mode (WGM). The mode in Figure 3.11(b) is a 3rd order WGM with 3 maxima. Whispering gallery modes differ from the radial-contour mode in that their acoustic wave propagates
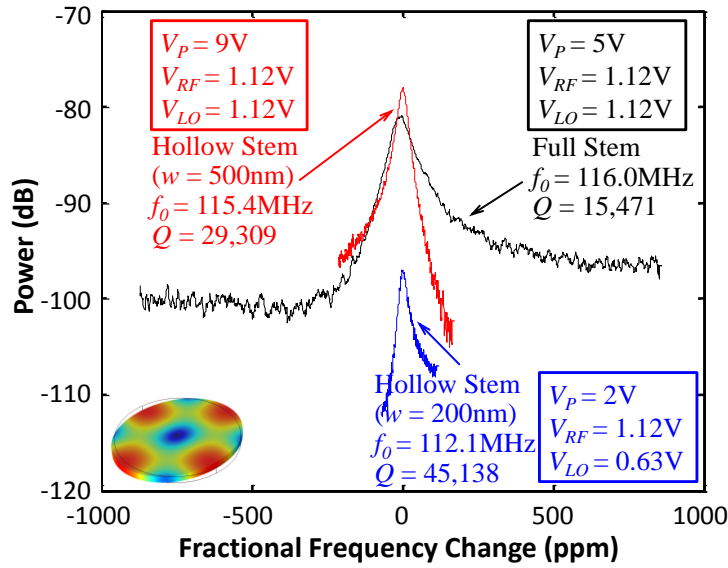
Figure 3.12: Comparison of frequency characteristics of full stem and hollow stem all-polysilicon disk resonators vibrating in the wine glass mode.

around the disk periphery, rather than the radial direction. Thus, while the radial-contour mode undergoes tremendous volume expansion and contraction during vibration, a whispering gallery mode conserves its volume, resulting in less displacement near the center of the disk, hence less Poisson expansion along the z-axis at the stem location. This then leads to smaller energy loss to the substrate and higher Q, which is consistent with the measurement results showing that wine glass mode Q for the 200nm-wall hollow stem disk in Figure 3.12 is larger than the highest posted by the radial-contour mode devices of Figure 3.8.

Higher order WGM's, such as the 3rd order one of Figure 3.11(b), further exhibit a dramatically larger displacement-free area around their stems than lower order ones, as shown in the displacement FEM simulations of Figure 3.11(a). This indicates that the former should lose less energy through the stem to the substrate no matter the type of stem, suggesting that higher order whispering gallery modes should post even higher Q's that are less dependent upon stem design, i.e., the Q should be high whether or not a hollow stem is used.

To confirm the above, Figure 3.13 presents a plot similar to that of Figure 3.12 and Figure 3.8, but this time comparing 3rd order WGM's for the different devices. The highest measured Q is now 93,231 at 177.9 MHz, again for the 200nm-wall hollow stem disk. As predicted, this is much higher than exhibited by the other modes depicted in Figure 3.12 and Figure 3.8. Although impressive, the Q of this device is only 1.4× higher than that of the same mode of the full stem device, which posts a Q of 65,012 at 176.2 MHz that is still quite large. Thus, hollow stem design is still beneficial for whispering gallery modes, but its benefits over a full stem diminish as mode order increases.
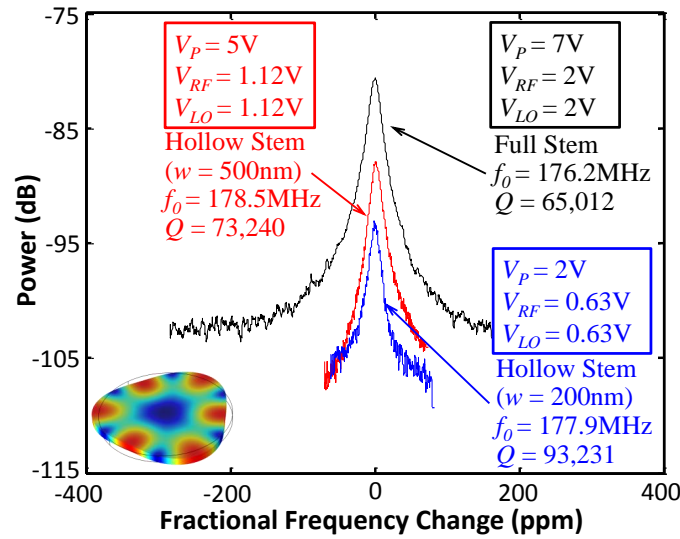
Figure 3.13: Comparison of frequency characteristics for full stem and hollow stem all-polysilicon disks vibrating in the 3rd-order whispering gallery mode.
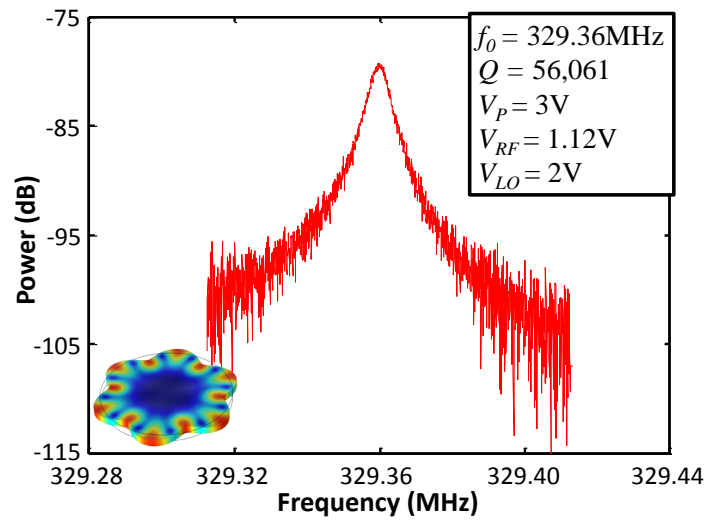
Figure 3.14: Measured frequency characteristic for a hollow stem polysilicon disk resonator vibrating in its 6th order whispering gallery mode.

As a final UHF demonstration, Figure 3.14 plots the frequency characteristics of a 17μm-radius disk employing a 500nm-thick hollow stem to achieve a Q of 56,061 at 329 MHz while vibrating in its 6th order whispering gallery mode as shown in Figure 3.11(c).

Chapter 4 Mechanically Coupled Disk Array Composites

A mechanically coupled disk array composite can lower the motional resistance R_x by summing together the in-phase output current of an array of identical resonators [12], which is highly desired for front-end channel-select filters that interface with widely used $50\,\Omega$ RF components. In addition, the coupled micromechanical disk array boosts the equivalent stiffness of the device, as discussed in Chapter 1, which is essential to lower the coupling beam to resonator stiffness ratio and achieve a narrow bandwidth filter. By using proper electrode phasing design and employing high-Q resonators, such array composite shows uncompromised performance even with design errors and fabrication process variations. As a side benefit, array composites can also enhance frequency stability by creating a large electrode-to-resonator capacitance (C_o) generated by the parallel combination of input/output electrodes overlapping each resonator, which reduces the efficacy of the bias voltage-controlled electrical stiffness and in turn negates k_e induced frequency shift. Therefore, an array composite will also have enhanced frequency stability against environmental fluctuations that changes k_e, such as acceleration, power supply noise, dielectric charging, etc.

This chapter first introduces the schematic and equivalent circuit of mechanically coupled radial contour mode disk array composites. Then it follows by showing equivalent circuit simulation results that indicate such high Q mechanically coupled arrays with proper electrode phasing design will work appropriately even with coupling beam length design errors and frequency mismatches among constituent resonators. After going through the improved fabrication process of capacitive-gap polysilicon disk resonators, it shows measurement results that confirm the efficacy of motional resistance improvement, proves the robustness of mechanically coupled arraying method, demonstrates the frequency stability enhancement effect, and finally verifies the accuracy of the negative capacitance equivalent circuit model by comparing with measured data that includes plots of frequency versus dc-bias voltages

4.1. Schematic of Radial Contour Mode Disk Array Composite

Figure 4.1 presents a one-dimensional (1D) two-port micromechanical disk array-composite constructed by mechanically linking individual disk resonators via coupling beams and electrically combining each input/output electrode to generate I/O ports. Here, coupling of resonators yields a multi-mode system that has N vibration modes, where N is
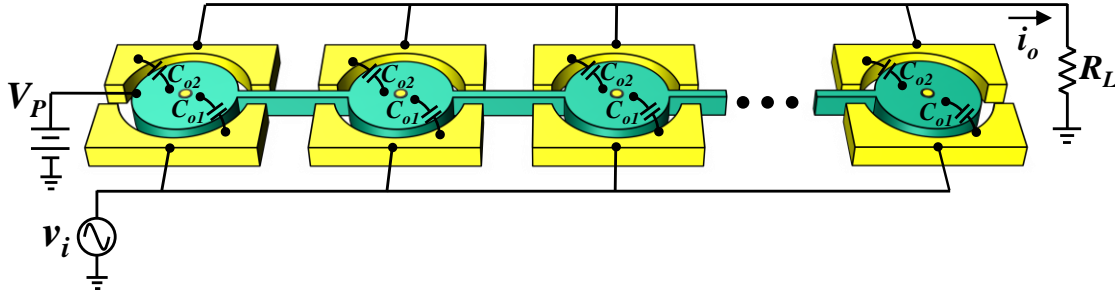
Figure 4.1: Schematic of a radial contour mode array composite with disks linked by λ/2 coupling beams to enforce in phase vibration of each individual resonator.
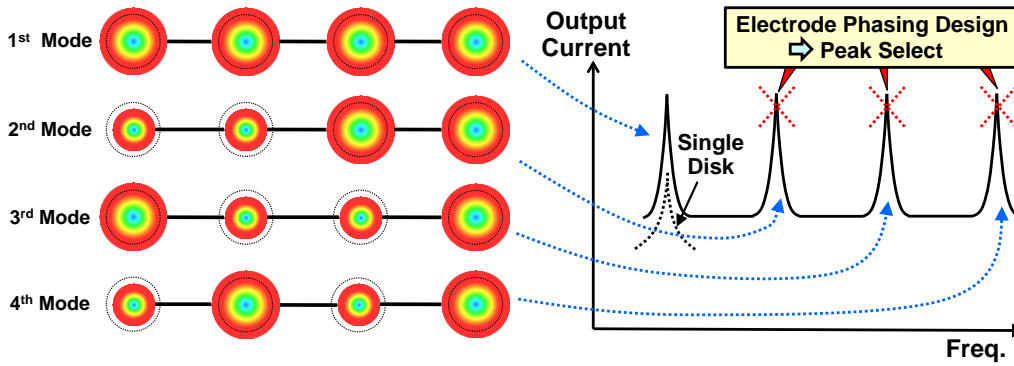
Figure 4.2: FEA simulated mode shapes of a mechanically coupled four-resonator radial contour mode disk array.

the number of coupled resonators. For example, a 4-resonator disk array-composite will have four mode shapes with each mode at different frequencies, as shown in the 2D FEM simulation results in Figure 4.2. At each mode, all resonators vibrate at precisely the same frequency [16], allowing their outputs to be combined to boost input and output currents, thereby decreasing the motional resistance and increasing power handling.

4.1.1. Half-wavelength Couplers

As described in [8], the mechanical connection of resonators in Figure 4.1 actually realizes a multi-pole filter structure that now has several modes of vibration. Each modal peak corresponds to a state where all resonators are vibrating at exactly the same frequency. The FEA simulated modal response in Figure 4.2 shows the different modes of similar structure with 4 constituent resonators, which are distinguishable by the relative phase response of each resonator.

To only select the desired in-phase mode (1st mode) for a micromechanical disk array, it is advantageous to first separate other unwanted modes as far apart as possible. Since the frequency separation is proportional to the stiffness of mechanical couplers, according to Chapter 1, the first step in selecting a single mode, while suppressing others, is to couple resonators with very stiff springs. Ideally, coupling beams with lengths corresponding to

Mechanical Coupler　　　　　　**Electrical Transmission Line**

$$\begin{bmatrix} F_1 \\ \dot{X}_1 \end{bmatrix} = \begin{bmatrix} cos(\alpha l) & jZ_m sin(\alpha l) \\ \dfrac{jsin(\alpha l)}{Z_m} & cos(\alpha l) \end{bmatrix} \begin{bmatrix} F_2 \\ \dot{X}_2 \end{bmatrix} \qquad \begin{bmatrix} v_1 \\ i_1 \end{bmatrix} = \begin{bmatrix} cos(\beta l) & jZ_o sin(\beta l) \\ \dfrac{jsin(\beta l)}{Z_o} & cos(\beta l) \end{bmatrix} \begin{bmatrix} v_2 \\ i_2 \end{bmatrix}$$
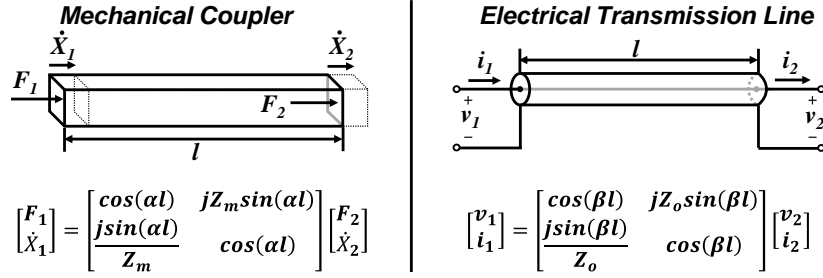
Figure 4.3: Two-port modeling of a mechanical acoustic coupling beam in analogy to an electrical transmission line.

half-wavelength of acoustic waves propagating in a resonator will shift the undesired resonance modes to infinity. As first demonstrated in [12], the use of half-wavelength couplers both insures that all resonators vibrate in phase, as shown in the 1st mode in Figure 4.2; and spreads the mode frequencies apart, making it easier to select a specific mode (when only one is wanted, e.g., in an oscillator application) by proper electrode phasing. The beam length of a half-wavelength coupling can be expressed as:

$$l_s = \frac{\lambda}{2} = \frac{\sqrt{E/\rho}}{2f} = \pi \frac{\sqrt{E/\rho}}{\omega} \qquad (4.1)$$

where ω is the radian frequency of the acoustic wave, ρ is the material density, E is the Young' modulus of the beam material, and λ is the full-wavelength of the acoustic wave propagating in coupling beams.

It should be noted that the use of half wavelength coupling beams serves to spread the undesired modal peaks of the array structure in Figure 4.2 to infinity, which facilitates the selection of one, and only one, of the modes. Once a single mode is selected, the structure practically behaves as a single resonator, but with a current handling ability equal to the sum of all constituent resonators. Thus, an N-resonator array can handle N times more power and achieve N times smaller motional resistance than a single resonator.

In general, fabrication variations and design errors exist, which may not be able to generate exact half-wavelength coupling beams and thereby can only separate the peaks by finite distance in frequency domain. However, because each mode exhibits a unique resonator phasing, a single mode can still be selected by choosing the input ac signal and output electrode configuration to match the phasing of the desired mode, e.g. directly connecting all output electrodes together will effectively cancel the output current from the mode shapes in which resonators vibrate out-of-phase, such as the 2nd-4th modes in Figure 4.2.

4.1.2. Equivalent Circuit of Mechanically Coupled Array Composites

As shown in Figure 4.3, a coupling beam can be modeled as an acoustic transmission line—the mechanical analog to the familiar electrical transmission line that takes the following expression by using an ABCD matrix:
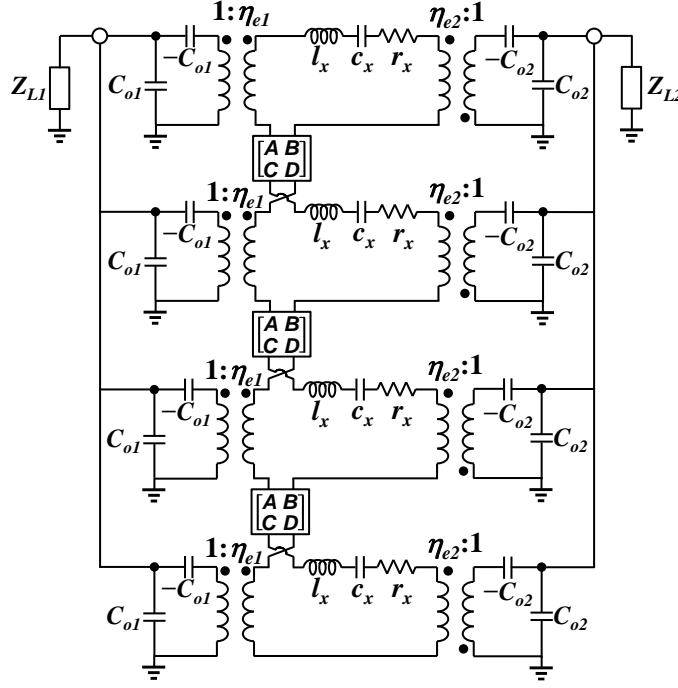
Figure 4.4: Small-signal equivalent circuit of a 4-resonator disk array-composite with two-port ABCD matrix model to capture the behavior of mechanical couplers.

$$\begin{bmatrix} F_1 \\ \dot{X}_1 \end{bmatrix} = \begin{bmatrix} A & B \\ C & D \end{bmatrix} \begin{bmatrix} F_2 \\ \dot{X}_2 \end{bmatrix} = \begin{bmatrix} cos(\alpha l) & jZ_m sin(\alpha l) \\ \dfrac{jsin(\alpha l)}{Z_m} & cos(\alpha l) \end{bmatrix} \begin{bmatrix} F_2 \\ \dot{X}_2 \end{bmatrix} \tag{4.2}$$

where F_i and $\dot{X}_i$ are the force and velocity at corresponding ports, l is the length of the coupling beam. Z_m and α in (4.2) are acoustic characteristic impedance and acoustic wave propagation constant, respectively, which take the forms:

$$\alpha = \frac{\omega}{\sqrt{E/\rho}}, Z_m = A_c\sqrt{E\rho} \tag{4.3}$$

where ω is the radian frequency of the acoustic wave, ρ is the material density, E is the Young' modulus of the beam material, and A_c is the beam cross sectional area.

Because a $\lambda/2$ array coupling is a strong coupling compared with that of a narrowband filter in [37], the coupled mechanical system in this work behaves as a wideband system, in which the coupling beams cannot be modeled as simple LC T-networks. Therefore a full ABCD matrix modeling of coupling beams is necessary for mechanically coupled array composites. By using the ABCD matrix model for a mechanical coupler and the traditional equivalent circuit of a contour mode disk resonator, Figure 4.4 develops an electrical equivalent circuit model of a 4-resonator array composite that can accurately capture its resonance frequency and motional resistance. Because an in-phase vibration of two adjacent disk resonators will generate forces with opposite directions on the two sides of
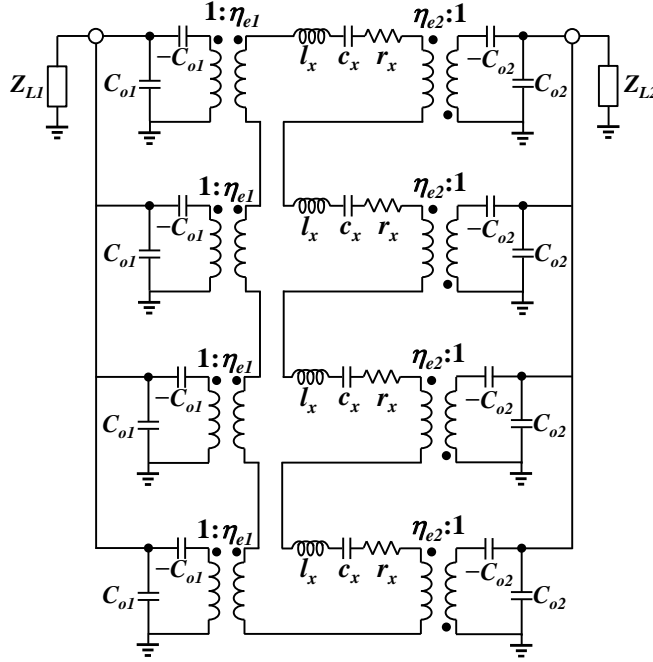
Figure 4.5: Modified equivalent circuit of a 4-resonator disk array-composite with half-wavelength coupling beams.

the mechanical coupler, the two-port ABCD matrix model in Figure 4.4 that represents a mechanical coupler actually connects adjacent resonators with opposite polarities by using crisscrossed pins on one side.

For a micromechanical disk array with $\lambda/2$ couplers, plugging (4.1) and (4.3) into (4.2) yields the force and velocity relationships at the two ports of the mechanical coupler as:

$$F_1 = -F_2 \, , \dot{X}_1 = -\dot{X}_2 \tag{4.4}$$

which means the force and velocity on the two sides of the mechanical coupler will have the same magnitude but opposite directions. Such condition indicates that adjacent disk resonators connected by the half-wavelength coupling beam will vibrate in-phase, and thereby enforce only the desired 1st mode with all other unwanted modes eliminated, as shown in the 4-resonator disk array case in Figure 4.2. For the case of half-wavelength coupling, a simple series connection can replace the ABCD matrix model and generate a modified 4-resonator disk array equivalent circuit as shown in Figure 4.5. To further simplify the equivalent circuit model of $\lambda/2$ coupled disk array composite, series or shunt combinations of a single disk resonator's equivalent circuit element values lead to a lumped circuit as shown in Figure 4.6.

Because a micromechanical disk array-composite ideally behaves like a single disk resonator when only the in-phase mode is selected, its equivalent circuit will use the same schematic and topology as that of a single disk resonator, as shown in Figure 4.6(a). For a disk array with N mechanically coupled disk resonators, the stiffness k_m, mass m_m, damping b_m, electromechanical coupling factor η_{ei}, and electrode-to-resonator overlap
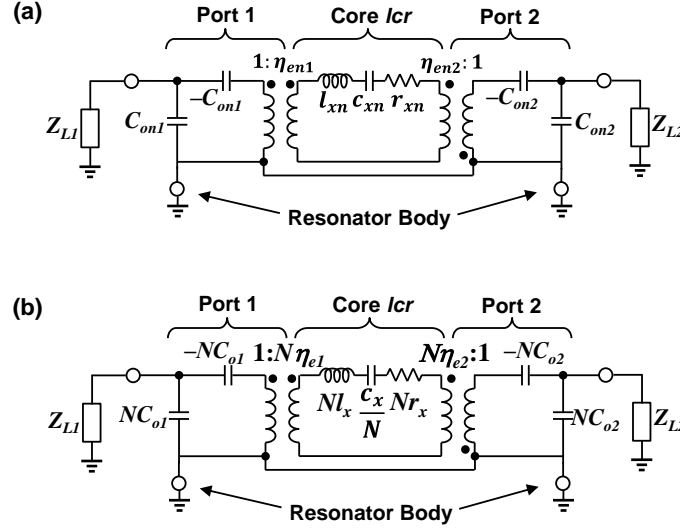
Figure 4.6: (a) Negative capacitance equivalent circuit of a disk array composite. With only the in-phase mode selected, the structure practically behaves like a single resonator, making it share the same equivalent circuit topology as a single disk resonator. (b) Negative capacitance equivalent circuit of a disk array with N resonators based on element values in the single resonator equivalent circuit in Figure 2.2.

capacitance C_{oi} are all N times larger than for a single disk resonator. Thus, simple multiplication or division by N is all that is needed to derive coupled array equivalent circuit element values from those of a single disk resonator, as shown in Figure 4.6(b).

4.2. Resilience Against Design Errors & Process Variations

Ideally, a half-wavelength mechanically coupled disk array-composite will perform as a single disk resonator but with smaller motional resistance, higher equivalent stiffness, and better power handling capability. In reality, it is challenging to achieve an exact half-wavelength coupling condition because the acoustic impedance presented by a coupling beam is discontinuous at $\lambda/2$ with infinite value [16], which indicates that the acoustic impedance will change dramatically and thereby impact the arrays' performance if the designed beam length slightly mismatches the real half-wavelength due to fabrication process variations or design errors. However, the following analysis indicates that a mechanically coupled disk array composite can tolerate these errors by using high-Q resonators and employing appropriate electrode phasing design. With resilience against design errors and process variations, one CAD design can potentially apply on devices with different materials, e.g. polysilicon and polycrystalline diamond resonators can share the same CAD design. Although the half-wavelength may be slightly off, theory and measurements indicate that it will not dramatically impact the in-phase mode selection of resonator array composites.
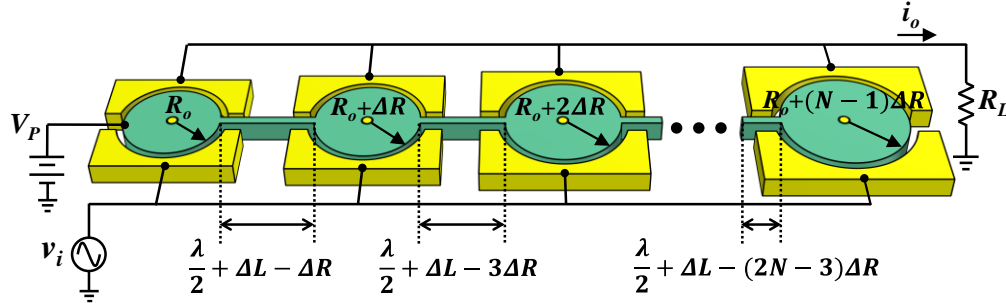
Figure 4.7: Schematic of an *N*-resonator disk array with design errors and process variations from fabrication process. Here, ΔL represents the coupling beam length design error and ΔR models the matching tolerance from fabrication process.

4.2.1. Fabrication Process Variations

Fabrication process such as film deposition, lithography, and ion plasma etching will generally cause variations in disk resonators' thickness and radius, leading to frequency deviations among individual resonators in an array. As the resonance frequency of a radial contour mode disk resonator is independent of thickness in the 1st order, this work assumes that the variation in disk radius ΔR causes frequency variations, as indicated in Figure 4.7. To do a simple comparison and save simulation time, Figure 4.7 only assumes that the disk radius varies in one direction with even distribution. Readers should be cautious that it only represents one case and a more completed study on variations should be based on Monte Carlo analysis.

Although the resonance frequency of each individual coupled resonator varies from each other, the multi-mode mechanical system will still vibrate at the desired mode at one frequency, but now with phase shifts in between each resonators due to mismatches between individual resonators. This will impact the output current combination and thereby degrade the motional resistance improvement of an array-composite. However, such phase-shift can be minimized to an extent that has minimal impact on the array composite's performance by employing very high-*Q* resonators, e.g., resonators with $Q > 10{,}000$.

From vibration principle point of view, the forced response of a system with multi-degree of freedom can represent the mechanical behavior of a disk array composite [38]. For a multi-degree of freedom system with no damping, the vibration of each element will be either in-phase or 180º out-of-phase, regardless of mismatches between each constituent spring-mass system. As capacitive-gap transduced micromechanical disk resonators have already achieved very high *Q*'s over 160,000 at 61 MHz [12] and larger than 29,000 at ~155 MHz [26], the damping factors for these devices are so small that the mechanically coupled array composite can be approximated as an undamped system, which enforces each individual resonator to vibrate almost in-phase even with mismatches. By assuming a 316 ppm standard deviation for a 32μm radius polysilicon disk resonator [39], the calculated standard deviation of disk radius is ~10.1nm, which corresponds to an approximate 800 ppm of resonance frequency standard deviation for a 12.8μm contour

TABLE IV: COMPARISON OF PHASE SHIFT VERSUS QUALITY FACTOR FOR A 4-RESONATOR DISK ARRAY AND 8-RESONATOR DISK ARRAY WITH DESIGN ERRORS AND MISMATCH FROM FABRICATION PROCESS.

Array Type	ΔR (nm)	Δf (ppm)	Resonator Number	$Q = 100$		$Q = 1,000$		$Q = 10,000$	
				Phase Shift from Input (°)	Max. Phase Shift (°)	Phase Shift from Input (°)	Max. Phase Shift (°)	Phase Shift from Input (°)	Max. Phase Shift (°)
4-resonator disk array	20.5	1600	1	178.22	2.29	179.36	0.24	178.00	0.02
			2	179.04		179.45		178.01	
			3	179.96		179.55		178.02	
			4	180.51		179.60		178.02	
8-resonator disk array	8.8	686	1	166.97	17.77	177.32	2.95	179.12	0.30
			2	168.93		177.70		179.15	
			3	172.06		178.28		179.21	
			4	175.64		178.89		179.28	
			5	179.05		179.43		179.33	
			6	181.86		179.85		179.38	
			7	183.79		180.13		179.41	
			8	184.74		180.27		179.42	

mode disk resonator. With a 99.7% confidence that the analyzed model will have a worse matching compared with the real case, the equivalent circuit of array-composites employs 6σ as the maximum frequency variation between resonators in Figure 4.7, which corresponds to a ΔR of 20.5nm for a 4-disk resonator array and ΔR of 8.8nm for a 8-resonator disk array. In addition, the equivalent circuit assumes a 10% design error in $\lambda/2$ coupling beam length as the acoustic velocity of the fabricated material usually deviates slightly from what is assumed in analytical calculation.

Table IV summarizes the phase shift comparison of each individual resonator's displacement versus Q for a 4-resonator disk array and 8-resonator disk array with coupling beam design errors and frequency mismatches from fabrication process. The maximum phase shift between constituent resonators in an array composite reduces by over 50× when Q improves from 100 to 10,000. Both 4-resonator disk array and 8-resonator disk array show phase shift no larger than 0.3º with $Q > 10,000$, which basically has negligible impact on output current combination. In addition, Table IV indicates that the more resonators in an array composite, the higher Q is needed to enforce in-phase response of each constituent resonator when design errors and fabrication mismatch exist.

4.2.2. Design Errors

In addition to the phase-shift issue that can be corrected by employing very high Q resonators, design errors in the length of coupling beams will lead to finite separation of unwanted vibration modes, which may introduce undesired resonance peaks in the frequency response spectrum of an array composite. Figure 4.8 presents the mode separation effect versus coupling beam length for a 4-resonator mechanically coupled multi-degree system. With $\lambda/2$ being a sensitive design point, even a 1% design error in
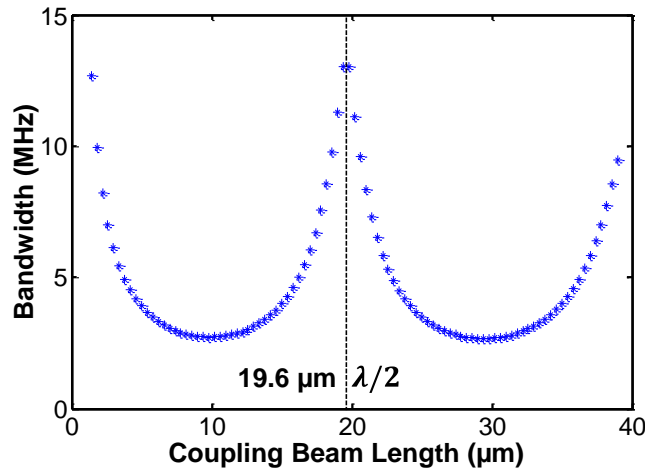
Figure 4.8: The magnitude of mode separation versus coupling beam length for a 213MHz polysilicon mechanically coupled 4-resonator disk array composite with 0.5 μm width coupling beam. Here, the bandwidth of this multi-degree mechanical system represents the effectiveness of mode-separation by mechanical couplers.

$\lambda/2$ coupling beam will cause mode separation to drop from infinite to ~13MHz, according to Figure 4.8, which makes devices vulnerable to spurious modes. Appropriate phasing of output current from each individual resonators will help to cancel the total output current from undesired modes. For a 4-resonator disk array composite as shown in Figure 4.2, a direct connection of the I/O electrodes in each constituent resonator will largely cancel the output current from other undesired vibration modes because of out-of-phase vibration in between resonators, which leaves output current only from the desired in-phase mode.

As shown in the simulation result in Figure 4.9(a), the frequency response of individual resonators in a 4-resonator disk array with half-wavelength design errors and resonance frequency mismatch will actually have 4 resonance peaks, with each representing different mode shapes in Figure 4.2, respectively. By designing appropriate electrode phasing (e.g. direct connection of all input & output electrodes for in-phase mode selection), Figure 4.9(b) indicates that a large part of the output current from undesired modes will cancel out, and thereby lead to a clean array-composite response which is very similar to a single disk resonator. Designers actually have freedom to select any specific modes by choosing different electrode phasing topologies, e.g., adding 180º phase shift to the output ports of resonator 1&2 will only select the 2nd mode in Figure 4.2 with output current of all other modes cancelled out. Therefore an appropriate electrode phasing will to some extent relax the $\lambda/2$ design accuracy requirement, even though the half-wavelength is a discontinuous point as indicated in Figure 4.8.
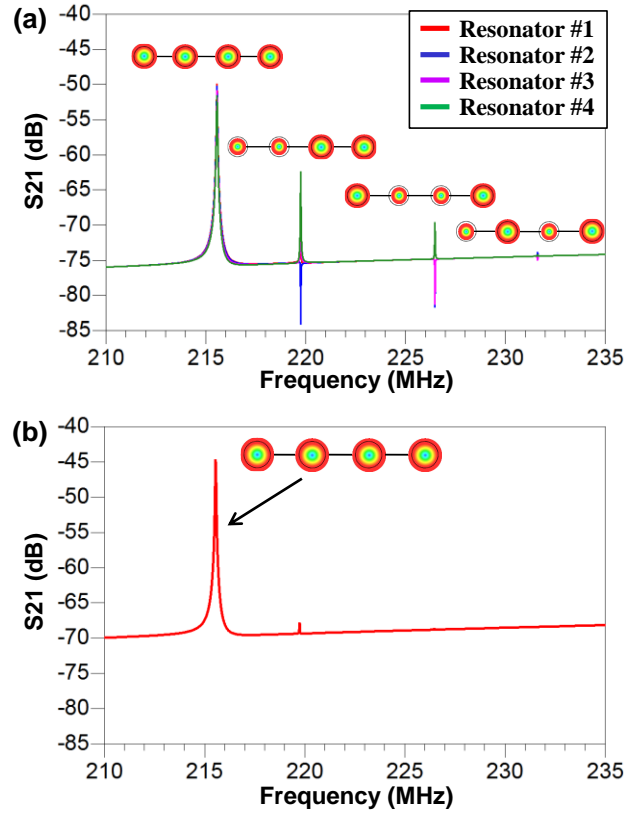
Figure 4.9: (a) Frequency response of each individual resonator in a 4-resonator disk array with 1600 ppm resonance frequency shift in between adjacent resonators and 10% $\lambda/2$ design errors. Here, the input electrodes of all resonators are tied together with input excitation voltage, with output electrode left separately to observe the output current from each vibration mode. (b) Frequency response of a 4-resonator disk array with all input electrodes connected to input excitation voltage and output electrodes all tied to the same sensing port.

4.3. Frequency Stability Enhancement of a Disk Array Composite

Oscillators referenced to very high Q capacitive-gap transduced MEMS resonators have already made inroads into the low-end timing market, and research devices have been reported to satisfy GSM phase noise requirements [12] [40] [41]. However, like any other oscillators, environmental fluctuations such as external vibrations, bias voltage noise, or charging, may greatly degrade this performance [23] [24]. A very important factor that affects resonance frequency is the electrical stiffness k_e, which can induce frequency instability and potentially set lower limits on not only short-term frequency stability, but long-term as well. As the electrical stiffness k_e of a capacitive-gap MEMS resonator is often determined by dc-bias voltage V_P, electrode-to-resonator overlap capacitance C_o, and the capacitive gap spacings d_o, environmental fluctuations that disturb any of these parameters will cause instability in electrical stiffness and generate frequency shift, as shown in Figure 4.10. For instance, theoretical analysis of micromechanical wine-glass
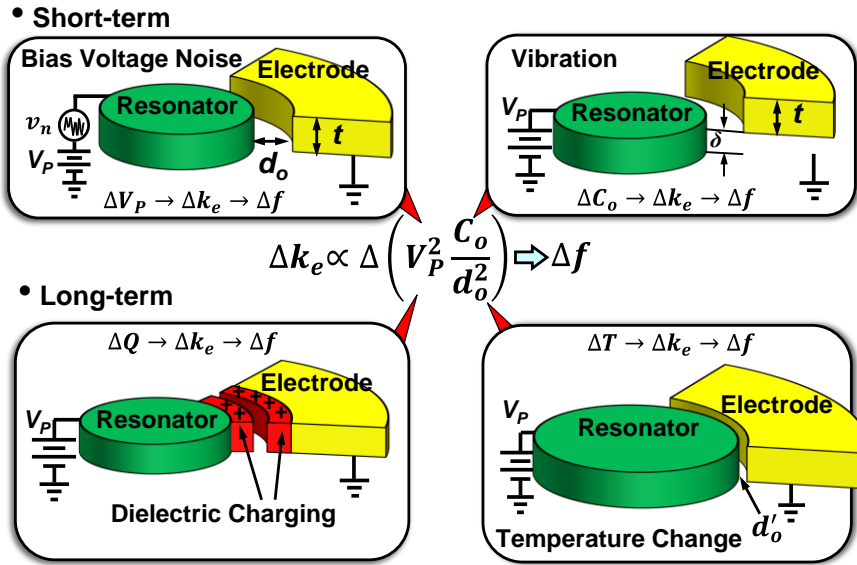
Figure 4.10: Various factors that can contribute to electrical stiffness induced frequency instability, which includes bias voltage noise, environment vibration, dielectric charging, and temperature drift.

disk resonators reveals that acceleration-induced changes in electrode-to-resonator gap spacing or overlap area that in turn induce shifts in electrical stiffness dominate among sources that shift frequency during accelerations [42]. In addition, noise or drift on the power supply manifests as fluctuations on the resonator dc-bias V_P that obviously destabilize the electrical stiffness, and thereby, resonance frequency [23].

Compared with stand-alone single disk resonator, mechanically coupled array composite can improve its frequency stability against the above mentioned environmental fluctuations. The key to enhanced frequency stability is the electrode-to-resonator capacitance (C_o) generated by the parallel combination of input/output electrodes overlapping each resonator in the array that in turn reduces the efficacy of the bias voltage-controlled electrical stiffness [27]. Here, an equivalent circuit based on negative capacitance provides improved visualization that helps to identify methods to suppress electrical stiffness induced frequency variation. The circuit model indicates that the more resonators in an array, the smaller the frequency shift imposed by a given bias voltage change. Both modeling and measurement suggest that the most stable MEMS-based oscillators (e.g., against supply noise and acceleration) are ones that utilize mechanically-coupled arrays of resonators.

4.3.1. Electrical Stiffness Induced Frequency Shift

The electrical stiffness of all electrodes will subtract from the mechanical spring constant of the resonator at the core *lcr* location, changing the resonance frequency of a two port radial contour mode disk resonator to:

$$f_o = \frac{1}{2\pi}\sqrt{\frac{k_r}{m_m}} = \frac{1}{2\pi}\sqrt{\frac{k_m - k_e}{m_m}}$$

$$= f_{nom}\sqrt{1 - \frac{k_e}{k_m}} \tag{4.5}$$

$$\approx f_{nom}\left(1 - \frac{1}{2}\cdot\frac{k_e}{k_m}\right)$$

Where k_r is the effective stiffness of the disk at any point on its perimeter, k_e is the total electrical stiffness contributed by all electrodes that surround the disk, k_m is the purely mechanical stiffness, and f_{nom} is the resonance frequency of the disk structure with zero dc-bias voltage applied. The last expression in (4.5) uses the binomial expansion to approximate f_o for the case in which the mechanical stiffness is many times larger than any of the electrical stiffness, which is generally true for devices in this dissertation. Rearrange of (4.5) yields the fractional frequency change due to electrical stiffness as:

$$\frac{\Delta f}{f_{nom}} = -\frac{1}{2}\frac{k_e}{k_m} \tag{4.6}$$

Indicated by (4.6), the resonance frequency of a radial contour mode disk resonator will be slightly lower than the mechanical natural frequency of the disk structure, due to frequency pulling effect of the force generated by time-varying changes in electric field strength as vibration changes the parallel-plate capacitive electrode-to-resonator gap. The ratio of electrical stiffness k_e to purely mechanical stiffness k_m actually captures the magnitude of such frequency shift. By inserting the expression of parallel-plate electrode-to-resonator overlap capacitance into (1.16), the total electrical stiffness k_e for a two-port radial contour mode disk resonator can be calculated as:

$$k_e = \frac{V_P^2(C_{o1} + C_{o2})}{d_o^2} = \frac{V_P^2 \epsilon A}{d_o^3} \tag{4.7}$$

where ϵ is the permittivity of the gap material (i.e., vacuum in this case) and A is the total overlap area between the resonator and its electrodes. Changes of any variables in k_e, such as dc-bias voltage noise, capacitance variation due to mechanical vibration, or charging induced bias voltage drift, can cause frequency stability issues for capacitive-gap MEMS resonators [23] [24].

4.3.2. Mitigation of Electrical Stiffness

To capture the influence of electrical stiffness more clearly, the negative capacitance equivalent circuit shown in Figure 2.2 models the influence of electrical stiffness on device

and circuit behavior by using a negative capacitance exactly equal in magnitude to the shunt static electrode-to-resonator overlap capacitance C_{oi} at each electrode terminal [25]. Note that the negative C_{oi} is also a static capacitor, just like the positive C_{oi} of the physical shunt electrode-to-resonator capacitance. With this circuit, by mere inspection, a designer can now immediately see that the shunt C_{oi} presents the opportunity to effectively negate the electrical stiffness, suppress frequency changes induced by electrical stiffness, and thereby stabilize the frequency against all variables in (4.7)—something highly desirable in some oscillator applications.
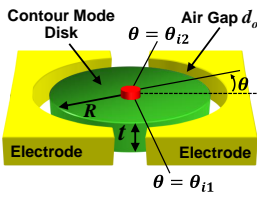
In order for the static electrode-to-resonator capacitor C_{oi} to negate the electrical stiffness represented by $-C_{oi}$, approximately same amount of current should flow through C_{oi} and $-C_{oi}$, which indicates that C_{oi} should pass most of the current flowing into the parallel combination of C_{oi} and Z_{Li}. In other words, the impedance of Z_{Li} should be much larger than that of C_{oi}, or:

$$|Z_{Li}| \gg \frac{1}{\omega_o C_{oi}} \tag{4.8}$$

From (4.8), to reduce electrical stiffness, both Z_{Li} and C_{oi} should be large. If Z_{Li} has no reactive component, operation at high frequency will also suppress electrical stiffness. However, increasing operating frequency may conflicts application requirement because the resonance frequency is usually application oriented, which means a designer may not have the freedom to change it. In addition, as a resonator might be used with reconfigurable drive and sense circuits that present non-constant loads, it would be also challenging to achieve better frequency stability by purely relying on optimizing load impedances. These two, together, lead to the only practical choice to enhance frequency stability against electrical stiffness, which is to boost a resonator's electrode-to-resonator's overlap capacitance C_o, e.g., utilizing resonators with solid dielectric gaps [43] [44], or building array of resonators.

The mechanically coupled array composite in this chapter will boost the electrode-to-resonator overlap capacitance by N times (N is the number of coupled resonators), which will obviously contributes to enhance frequency stability according to (4.8). Note that although the electrical stiffness goes up by N according to (4.7), so does the mechanical stiffness, so their ratio k_e/k_m remains the same and the fundamental efficacy by which k_e pulls the frequency, as governed by (4.5), does not increase. Instead, with C_{oi} presenting a much smaller impedance, more current flows through C_{oi} than Z_{Li}, allowing it to cancel more of C_{ei}, thereby negating the electrical stiffness induced frequency instability via circuit interaction.

Table V: Radial contour mode disk array design equations and procedure summary

Objective/Procedure	Parameter	Relevant Design Equations for a Given Parameter	Eq.
	Solve For δ	$$\delta \times \frac{J_0(\delta)}{J_1(\delta)} = 1 - \nu$$	(4.9)
	Angular Resonance Frequency ω_{nom}	$$\omega_{nom} = \frac{\delta}{R}\sqrt{\frac{E}{\rho(1-\nu^2)}}$$	(4.10)
Given: ω_{nom}, V_P, N, R_{xij} (= resistance between terminals i and j). Find: R, d_o. 1. Choose E, ρ, and ν by choice of structural material. 2. Choose thickness t. 3. Use (4.10) to find the R needed to achieve ω_{nom}. Use (4.9) to get δ in the process. 4. Use (4.14) to find the d_o needed to achieve R_{xij}. 5. (4.11), (4.12) and (4.13) yield all needed values in the ac small signal equivalent circuit in Figure 4.6(a).	Core Equiv. Circuit Elements	$$l_{xn} = Nm_m = N\frac{2\pi\rho t \int_0^R rJ_1^2(hr)\,dr}{J_1^2(hR)},$$ $$h = \sqrt{\frac{\omega_{nom}^2\rho}{\left(\frac{2E}{2+2\nu} + \frac{E\nu}{1-\nu^2}\right)}}$$ $$c_{xn} = \frac{1}{Nk_m} = \frac{1}{\omega_{nom}^2 Nm_m}, \quad r_{xn} = \frac{\omega_{nom}Nm_m}{Q}$$	(4.11)
	Static Overlap Capacitor	$$C_{oni} = N\frac{\epsilon_o(\theta_{i2}-\theta_{i1})Rt}{d_o}$$	(4.12)
	Electro-mechanical Coupling Coefficient	$$\eta_{eni} = V_P\frac{C_{oni}}{d_o}$$	(4.13)
	Motional Resistance	$$R_{xij} = \frac{r_{xn}}{\eta_{eni}\eta_{enj}}$$	(4.14)

4.4. Design Examples: 213-MHz Contour Mode Disk Arrays

Table V summarizes the needed expressions (reference to Figure 4.6(a) for variables) while also succinctly presenting a design flow to achieve a radial-contour mode disk array composite with N resonators like that of Figure 4.1 with specific operating frequency and motional resistance R_x. This section also designs several 213-MHz ($R = 12.8$ μm) radial contour mode disk arrays employing various number of mechanically coupled resonators ($N = 1, 8, 16,$ and 50). The measurement results of motional resistance improvement, design robustness, and frequency stability enhancement on these device will be analyzed in Section 4.6. Table VI summarizes the design parameters, equivalent circuit variables, and

Table VI: Comparison of design variables and equivalent circuit element values for 215-MHz radial contour mode disk arrays with different number of mechanically-coupled resonators.

	Parameter	Source	Number of Resonators				Units
			1	8	16	50	
Design Variables	Number of Resonators, N	N/A	1	8	16	50	N/A
	Disk Radius, R	Layout	12.8	12.8	12.8	12.8	μm
	DC Bias Voltage, V_P	N/A	9	9	9	9	V
	Disk Thickness, t	Fabrication	2	2	2	2	μm
	Electrode-to-Resonator Gap, d_o	Fabrication	50	50	50	50	nm
	Natural Frequency, f_{nom}	Equation (4.10)	215	215	215	215	MHz
	Coupling Beam Length l	Layout	21.2	21.2	21.2	21.2	μm
	Electrode Span Angle, θ	Layout	133	133	133	133	(°)
	Quality Factor, Q	Measurement/ Estimate	10,000	10,000	10,000	10,000	N/A
Equivalent Circuit Elements	Equivalent Inductance, l_{xn}	Equation (4.11)	1.81×10^{-12}	1.45×10^{-11}	2.89×10^{-11}	9.03×10^{-11}	H
	Equivalent Capacitance, c_{xn}	Equation (4.11)	3.03×10^{-7}	3.79×10^{-8}	1.89×10^{-8}	6.06×10^{-9}	F
	Equivalent Resistance, r_{xn}	Equation (4.11)	2.44×10^{-7}	1.95×10^{-6}	3.91×10^{-6}	1.22×10^{-5}	Ω
	Overlap Capacitance, $C_{on1} = C_{on2}$	Equation (4.12)	9.2	73.8	148	462	fF
	Electromechanical Coupling, $\eta_{en1} = \eta_{en2}$	Equation (4.13)	1.46×10^{-6}	1.17×10^{-5}	2.33×10^{-5}	7.29×10^{-5}	N/A
	Electrical Stiffness Induced Frequency Shift $(f_o - f_{nom})/f_{nom}$	Equivalent Circuit of Figure 4.6(b)	-71.3	-56.6	-38.7	-19.8	ppm

electrical stiffness induced frequency shift for four different type of disk array designs which have the same disk radius ($R = 12.8$ μm) and coupling beam length, but different number of resonators. The negative capacitance equivalent circuit predicts that the 213-MHz 50-resonator disk array will reduce the frequency shift caused by 9 V dc-bias voltage variation by 3.6× to -19.8 ppm, compared with the -71.3 ppm shift of a stand-alone single disk resonator, which theoretically verifies the frequency stability enhancement effect from micromechanical coupled disk arrays.

4.5. Fabrication Process

The fabrication process for the all-polysilicon contour mode disk resonator arrays of this work deviates from previous ones, such as that of [11], in that it does not use self-aligned peg-stem anchors and it employs chemical mechanical polishing (CMP) to remove electrode overhangs. The process begins with film depositions and etches identical to those of [11] to achieve the substrate isolation layer, polysilicon interconnects, and the bottom sacrificial layer. At this point, unlike previous self-aligned processes, a mask is used to define, pattern, and etch stem anchor holes into the bottom sacrificial oxide, followed by a
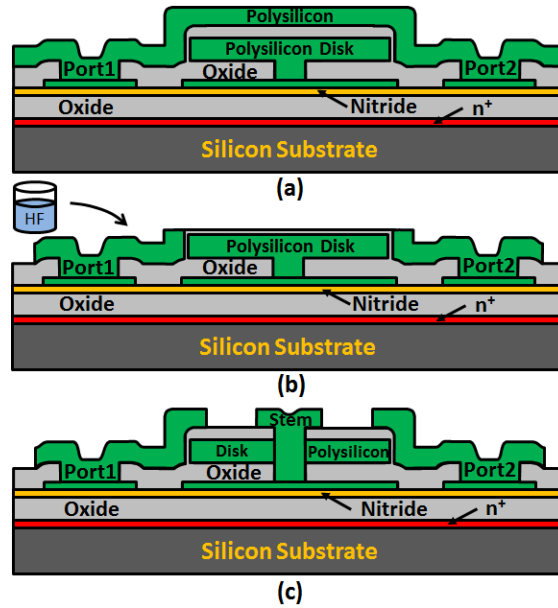
Figure 4.11: Cross-sections showing the last few steps in the fabrication process for a 215-MHz all-polysilicon disk resonators with CMPed electrodes (a. b), and a comparison to previous work's fabrication process, (c).

2-µm LPCVD in-situ doped polysilicon film that fills the holes to form the stems and serves as the resonator structural material. Here, an AMSL300 DUV Stepper is used to realize very precise alignment, with less than 100nm error—good enough to achieve Q's comparable to those of devices with self-aligned stems.

After depositing an oxide hard mask over the structural polysilicon, disk devices and coupling links are patterned and etched as before, the gap-defining sacrificial sidewall oxide spacer is deposited, electrode to interconnect contact vias are etched, and the polysilicon electrode material LPCVD'ed 3-µm thick, all to yield the cross-section of Figure 4.11(a). At this point, the process again deviates from that of [11] in that before patterning and etching the electrodes, the top polysilicon is first CMP'ed down to the hard mask. This step removes the electrode overhangs of Figure 4.11(a), achieving the final cross section of Figure 4.11(b). When compared to the previous cross section of [11], cf. Figure 4.11(c), this new process greatly increases the pull-in voltage of these devices, where contact between the disk and the electrode overhang is often the first to occur when dc-bias voltages increase. As before, devices are released in 49 wt. % hydrofluoric acid for ~40min.

Figure 4.12 presents the SEM of the fundamental element of micromechanical disk arrays — a 213-MHz stand-alone radial contour mode disk resonator fabricated using the process flow described above. Clearly indicated by Figure 4.12, there are no electrode overhangs above the disk structure, which can potentially increase the maximum dc-bias voltage that the device can tolerate. Figure 4.13, Figure 4.14, and Figure 4.15 present SEMs of fabricated 213-MHz 50-nm capacitive-gap transduced half-wavelength-coupled disk arrays employing 8, 16, and 50 resonators, respectively, in straight line and rectangular placement configurations.
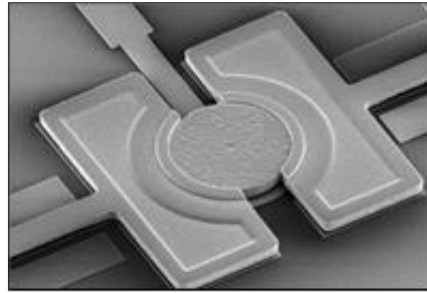
Figure 4.12: SEM of a 213-MHZ stand-alone contour mode disk resonator with 50nm capacitive gap.
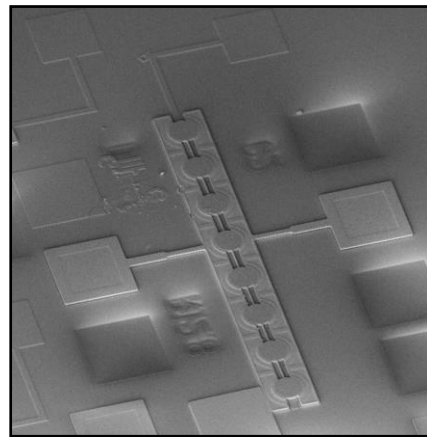
Figure 4.13: SEM of a 213-MHZ 50nm capacitive-gap contour mode disk array employing 8 resonators.
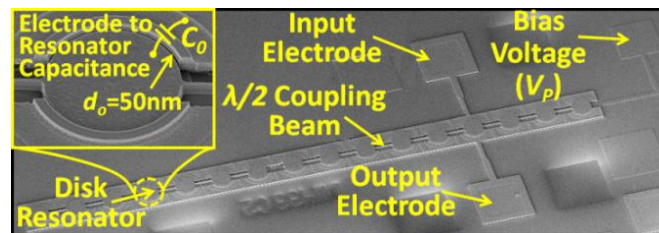
Figure 4.14: SEM of a 213-MHZ 50nm capacitive-gap contour mode disk array employing 16 resonators.
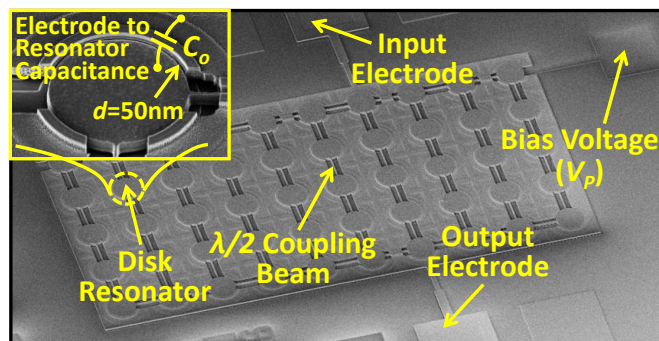
Figure 4.15: SEM of a 213-MHZ 50nm capacitive-gap contour mode disk array employing 50 resonators.
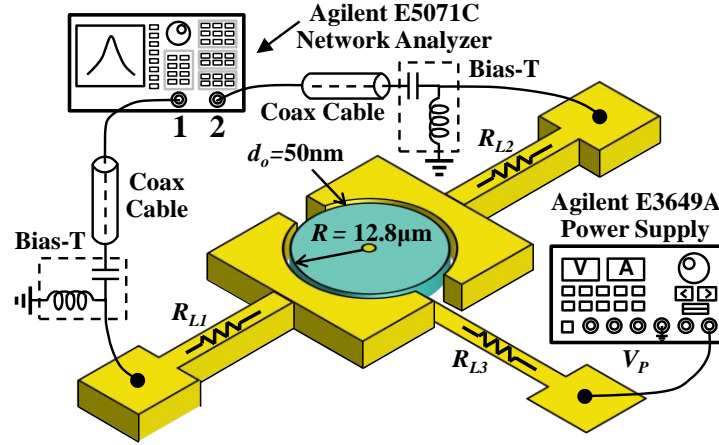
Figure 4.16: S21 direct measurement setup for a polysilicon 213-MHz capacitive-gap radial-contour mode disk resonator.

4.6. Measurement Results

To demonstrate the efficacy of array design techniques discussed in Section 4.1 and 4.2, measured frequency response of S parameters are in order, for both mechanically coupled disk array-composite resonators using various numbers of resonators, as well as for a single stand-alone disk for comparison. In addition, measured plots of resonance frequency versus dc-bias voltage on these devices also gauge the degree to which arraying enhances frequency stability against electrical stiffness changes. To this end, measurements were made under a 2μtorr vacuum environment in a Lakeshore FWPX vacuum probe station in the direct two-port excitation and sensing scheme. Figure 4.16 presents the direct two-port measurement setup used in this work for a radial contour mode disk resonator, which records the S21 parameter of the devices to observe the resonance frequency by using an Agilent E5071C network analyzer.

4.6.1. Stand-Alone Contour Mode Disk Resonators

Figure 4.17 presents the frequency spectrum of a stand-alone radial contour mode disk resonator with 12.8 μm radius and 50-nm capacitive gap measured under vacuum using the two-port setup shown in the figure inset and a dc-bias voltage of 25 V. As shown, this device exhibits $Q > 14,000$ at 213.9 MHz, which is good enough to enforce in-phase response for array-composites with design errors and frequency mismatches, as described in Section 4.2. The dc-bias voltage goes up to 25 V because of improved fabrication process with CMP'ed electrodes, which is about 1.7× higher than the previously reported 15 V by similar capacitive-gap devices at the same frequency without CMP process [25]. With dc-bias voltage of 25 V and Q of 14,260, the motional resistance extracted from the plot reaches 12.1 kΩ.
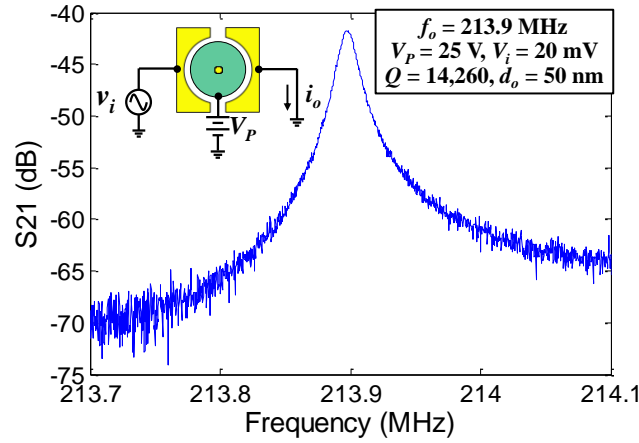
Figure 4.17: Frequency spectrum of a 50 nm-gap capacitive-gap single disk ($R = 12.8$ μm) resonator vibrating in radial contour mode shape.
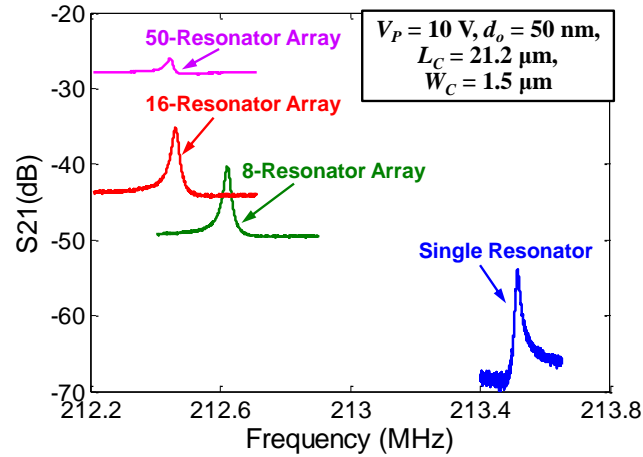
Figure 4.18: Frequency response spectra for a 213-MHz stand-alone disk resonator and mechanically coupled disk resonator array-composites with 8, 16, and 50 resonators.

4.6.2. Mechanically-Coupled Resonator Arrays

Figure 4.18 presents frequency characteristics measured using two-port configurations under vacuum for a stand-alone radial contour mode disk resonator, and eight-, sixteen-, and fifty-resonator coupled disk arrays with resonance peak heights clearly increasing with the number of resonators coupled. To allow for direct comparison of motional resistance, same dc-bias was applied to each device for measurement, and a low ac drive level (less than 100 mV) was used to avoid nonlinearity. Table VII presents a comparison of R_x values for each of these devices, clearly showing decrease in R_x with increase in the number of resonators. The 50-resonator disk array achieves a motional resistance of 1.9 kΩ, which is a 26× improvement over the single disk resonator. Note that the deviations in Q for arrays

TABLE VII: 213-MHz *N*-RESONATOR DISK ARRAY PARAMETERS AND MEASURED PERFORMANCE

N	Measured R_x (kΩ)	R_x Reduction	Q (Mea.)	Q-Normalized R_x Reduction	Overlap Cap. C_{oi} [fF]	R_{L1} [kΩ]	R_{L2} [kΩ]	R_{L3} [kΩ]	Relative Peak dB (Sim.)	Relative Peak dB (Mea.)
1	49.3	1×	19,520	1×	9.2	0.3	0.3	1.56	16.3	15
8	10.2	4.8×	11,532	8.1×	73.8	0.3	0.3	4.04	12.9	9.5
16	5.7	8.7×	10,792	15.7×	148	0.3	0.3	5.24	5.3	8.0
50	1.9	26.1×	10,965	46.5×	462	0.3	0.3	2.92	2.8	2.6

versus stand-alone resonator seen in Table VII are partially responsible for non-matching R_x reduction factors (which are not exactly equal to the number of resonators). For a fair comparison, Table VII also calculates the R_x reduction factors with normalized Q (normalized by multiplying R_x of each resonator by its Q). The Q-normalized R_x reduction factors of 8.1×, 15.7×, and 46.5×, exhibited by eight-, sixteen-, and fifty-resonator mechanically coupled resonator arrays, respectively, show good matching between reduction factor and number of resonators. The degradation in Q may be attributable to the unbalanced coupled resonators in a mechanically coupled array, e.g., the resonators at the two ends only have coupling beams at one side as shown in Figure 4.1, which leads to unbalanced forces during vibration, generates more energy loss via stem, and thereby limits Q. Although the reported Q's of arrays in Table VII are slightly lower than the single disk resonator, they are still above 10,000, which is good enough to enforce in-phase response of each individual resonator, as indicated by Table IV.

As seen in Figure 4.18, in addition to R_x reduction, mechanical coupling of resonators also shifts the center frequency of the peak from that of a stand-alone resonator. For the arrays in Figure 4.18, the resonance frequencies shifts from around 213.5 MHz down to 212.4 MHz. This comes about because the 21.2 μm length coupling beams were originally designed for poly-diamond material, which has ~8% design error to the simulated $\lambda/2$ of 19.6 μm for polysilicon material. For coupling beam slightly longer than $\lambda/2$, the resonance frequency of an array composite will shift downward compared with single resonators because the coupling beams effectively add more mass to the system than stiffness, which decreases the effective array stiffness-to-mass ratio and in turn reduces the overall resonance frequency. In this case, the frequency shift between single disk resonator and disk arrays is only ~0.5%, which is small enough to be fixed by post-fabrication laser trimming [45].

Figure 4.18 also clearly shows that the off-resonance background level limited by electrode-to-resonator overlap capacitance increases as the number of resonators in an array increases. As shown in Figure 4.1, a direct electrical feed-through pass exists via the electrode-to-resonator overlap capacitance, which could potentially increase the off-resonance response if the dc-bias voltage line has finite trace resistance (as shown in R_{L3} in Figure 4.16) and cannot shield all feed-through current from input. Ideally, the feed-through current dominated background response will increase the same amount as the resonance peak for an array composite. However, as V_p line trace resistance doesn't scale down as electrode-to-resonator overlap capacitance increase, the feedthrough current increases more compared with the resonance peak does, making the relative peak height smaller compared with a single disk resonator. By applying trace resistance values to the
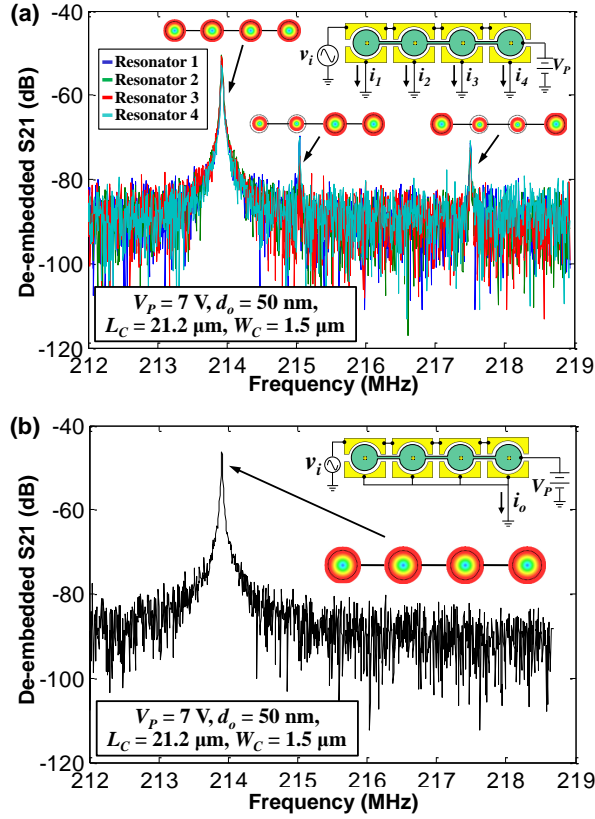
Figure 4.19: (a) Measured de-embedded frequency response spectra of each individual resonator in a mechanically coupled 4-resonator disk array composite. (b) Measured de-embedded frequency response spectrum of a mechanically coupled 4-resonator disk array composite with appropriate electrode phasing design. Here, various vibration modes are observed in the individual resonators' response due to coupling beam design errors and resonance frequency mismatches from fabrication process. A direct combination of output electrodes cancels out undesired modes (mode 2, 3, and 4 in Figure 4.2) and only select the in-phase mode shape.

equivalent circuit model, Table VII also shows the simulated relative peak height for array composites with different number of resonators, which has the same trend as the measured results. Both results indicate that, with finite trace resistance, the relative peak height will decrease as the number of resonators in an array composite increases. By employing new fabrication process that uses thicker polysilicon interconnect or more conductive material, the trace resistance will be negligible compared with the impedance of overlap capacitance of an array, leading to same relative peak height for both single resonators and array-composites [25].

4.6.3. Benefits from Electrode Phasing and High-Q System

To show the impact of $\lambda/2$ coupling beam design error on array performance and demonstrate the efficacy of electrode phasing design to knock out spurious modes, Figure
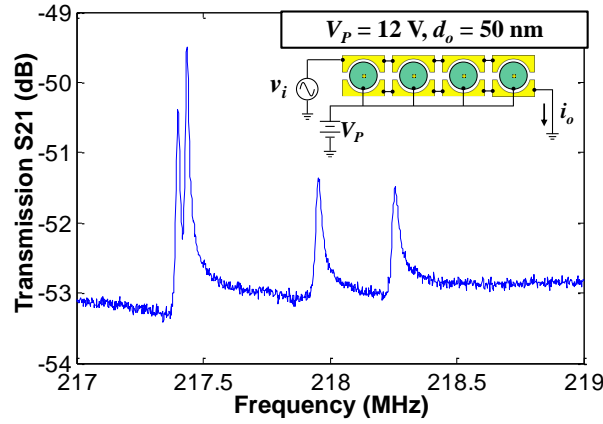
Figure 4.20: Measured Frequency spectrum of a 4-resonator disk array with no coupling beam connecting individual resonator. The resonance frequencies of each constituent resonator varies, which leads to a multi-peak response due to variations from fabrication process.

4.19 presents the de-embedded S21 response of a 4-resonator disk array and the response of each individual resonators in the same type of array, by using the measurement setup in the figure insets. In order to better observe the spurious modes that usually have smaller peaks compared with the main response, Figure 4.19 plots the de-embedded S21 responses that mathematically take out the feedthrough current from electrode-to-resonator overlap capacitance. As the designed coupling beam length of 21.2 μm misses the simulated 19.6 μm half-wavelength value by 8%, it only separates the unwanted spurious modes by ~1 MHz from the desired in-phase response, as shown in Figure 4.19 (a), instead of shifting all unwanted spurious modes infinite away. However, a mechanically coupled array composite can tolerate such coupling beam design error by using appropriate electrode phasing topology. As clearly shown in Figure 4.19 (b), a direct connection of all output electrodes enforces the in-phase response while cancels out the current from all other spurious modes, e.g., out-of-phase vibrations in undesired modes in Figure 4.19(a) will generate current in opposite direction and cancels out at the output. As readers may observe, there are only 3 modes in Figure 4.19(a), with one mode missing according to Figure 4.2. The 4th mode disappears because it has a better matched vibration amplitude from individual resonators, which contributes to not only cancel out output current, but also negate the effective excitation force generated from the input side, causing very small response that will be immersed in noise and cannot be observed.

Figure 4.20and Figure 4.21 present the measured frequency mismatch due to fabrication process in a 4-resonator disk array and the in-phase response enforcement by a high-Q system. The maximum frequency variation between resonators in the un-coupled 4-resonator disk array is around ~4000 ppm, which could be attributable to variation of film thickness, etching uniformity, and lithography during fabrication process. As shown in the response of each constituent resonators in Figure 4.21, such array can still enforce in-phase response of each individual resonators with total phase shift no larger than 0.5° because of high Q's of coupled resonators, which helps to achieve maximum output when combining current from each individual resonator.
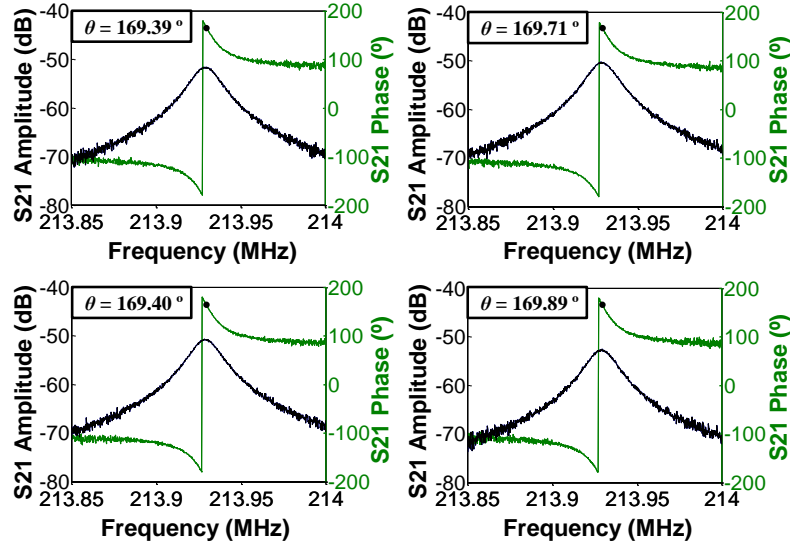
Figure 4.21: Measured de-embedded phase and amplitude response of each resonator in a mechanically coupled 4-resonator disk array using the measurement setup in the inset of Figure 4.16.
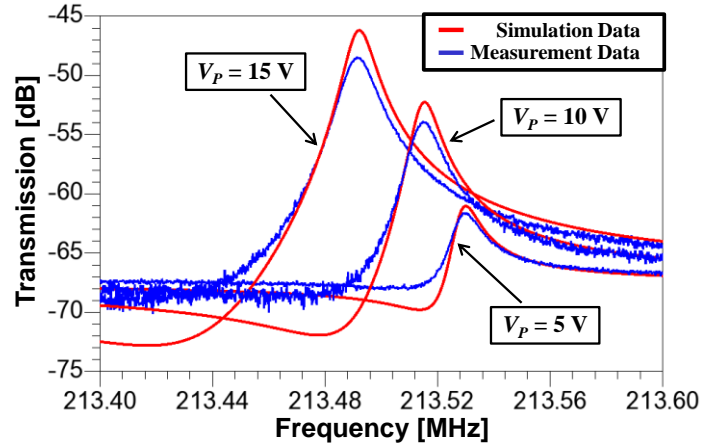
Figure 4.22: Frequency spectrum of a single radial contour mode disk resonator under different dc-bias voltage conditions. (V_P = 5 V, 10 V, and 15 V)

4.6.4. Frequency Stability Enhancement

Figure 4.22 plots the measured S21 parameter of a single radial contour mode disk resonator under different dc-bias voltage conditions (V_P = 5 V, 10 V and 15 V). It observes a 180 ppm frequency change as V_P varies from 15 V down to 5 V, which clearly shows the electrical stiffness induced frequency pulling effect. It also indicates that the frequency stability of a single disk resonator will be susceptible to all factors that changes electrical stiffness, such as environment acceleration or dc-bias voltage noise.
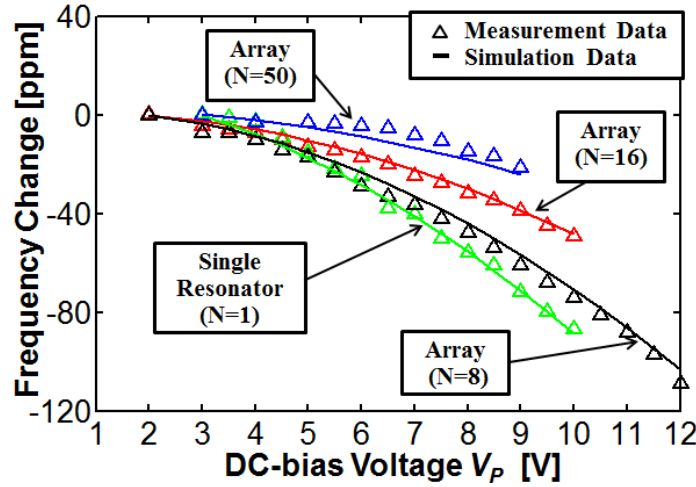
Figure 4.23: Measured curves of resonance frequency versus dc-bias voltage V_P plotted against simulation using negative capacitance equivalent circuit models for disk arrays with $N=1$, $N=8$, $N=16$, and $N=50$.

To demonstrate the frequency stability enhancement against dc-bias voltages from micromechanical disk array composite, Figure 4.23 plots the fractional frequency change along the y-axis against various dc-bias voltages, for radial contour mode disk arrays with various number of resonators, e.g., $N = 1, 8, 16,$ and 50. The measured curves clearly show a shrinking frequency dependence on dc-bias voltage as the number of resonators used in an array increases. In particular, the 50-resonator 213-MHz disk array experiences a 20 ppm frequency change when V_P varies over a 7 V span, from 2 V to 9 V, 3.5× smaller than the 70 ppm of a stand-alone device.

To confirm the validity of the negative capacitance equivalent circuit of Figure 4.6(b), simulated plots using this circuit are also included in Figure 4.23, showing very good agreement between theory and measurement. These simulations assume the load impedance Z_{Li} derives from a combination of series trace resistance R_{L1} and R_{L2} from input/output electrode leads, as well as similar lead resistance R_{L3} from the V_P port, all shown in Figure 4.16. Since probe coax and bond pad capacitance are nulled by calibration, Z_{Li} in these measurements is mainly resistive. It should be noted that the total equivalent load resistance $R_{Li,tot}$ of a disk array in this work is generally larger than that of a single resonator and actually increases with the number of disks in the array. This comes about because, at least in the current layout, the distance between the V_P pad and the furthest resonator increases as the number of resonators increases, as seen from Figure 4.14, resulting in a corresponding increase in series resistance R_{L3}. Table VII summarizes overlap capacitance and equivalent load resistance values for disk arrays with $N=1, 8, 16,$ and 50, clearly showing larger values as the number of resonators increases, at least for straight line (1D) arrays with $N=8$ and $N=16$ as indicated by the SEM in Figure 4.14. The series resistance of the 50-resonator array depicted in Table VII is actually smaller than those of the 8- and 16-resonator ones, since its layout uses a rectangular or matrix topology, rather than a straight line, so the average distance of its resonators from its V_P pad ends up being smaller.

According to (4.8), increases in load resistance like those in Table VII should also contribute to an overall nulling of the electrical stiffness, and thereby enhance frequency stability against dc-bias voltage fluctuations. Indeed, as the number of array resonators increases, electrical stiffness erodes due to increases in both electrode-to-resonator overlap capacitance and load resistance—a double whammy effect perfectly predicted by the negative capacitance equivalent circuit.

Chapter 5 3rd-order Flexural Mode Disk Array Filters

The rapid growth of micromachining technologies that yield high-Q on-chip mechanical resonators [5] now presents an opportunity to miniaturize and integrate highly selective filters together with transistor circuits, which may contribute someday towards implementation of single-chip super-heterodyne transceivers. With Q's higher than 10,000 under vacuum, polycrystalline silicon micromechanical resonators can potentially serve well as miniaturized substitutes for crystals or SAWs in narrowband filtering applications [26]. To date, coupled two-resonator prototypes of such filters have been demonstrated at very high frequency (VHF) (e.g., 223 MHz in [46]). However, applications in communication often desires sharper roll off response which requires higher order filters [37]. Due to smaller electromechanical transduction strength and increased mechanical coupler stiffness at higher frequency, higher-order capacitive-gap micromechanical coupled filters utilizing three or more resonators have not yet been achieved at VHF frequency range.

This chapter realizes a 3rd order VHF narrowband 75MHz micromechanical filters by employing flexural mode disk array composites as 'resonator' element. By using 7-resonator 50nm capacitive-gap flexural mode disk arrays, the 75MHz 3rd order VHF filter achieves a passband of 210 kHz (0.28%) and an improved 20dB shape factor of 1.46 with 40dB stopband rejection. Similar to the previously used filter coupling technique [47] [48], the 3rd order filter in this dissertation utilizes the coupling topology as shown in Figure 5.1, with the only difference that each resonator in the figure actually represents an flexural mode disk array composite. For the majority of mechanical band pass filter designs, the order is synonymous with the number of coupled resonators. As shown in Figure 5.1, a coupled 3-resonator system will exhibit three closely spaced resonance modes that all together define the filter's passband. Here, each resonance peak corresponds to a distinct physical mode shape. The center frequency of the filter is determined primarily by the frequency of the constituent resonators, while the bandwidth is determined largely by the stiffness ratio of the couplers to the resonators. Properly chosen termination resistors will finally flatten the jagged passband and achieve a filter response.

This chapter will first discuss the design of a flexural mode disk resonator and its equivalent electrical circuit model derivation using electromechanical analogies. Then it follows in Section 5.2 by introducing the method of building mechanically coupled resonator array composites with quasi-zero length couplers, which not only reduces a filter's termination resistance and bandwidth, but also does this with minimal increase in area. The analysis and design in Section 5.3 develop the completed equivalent electrical circuit model of a 3rd order coupled array filter and identifies potential paths to optimize
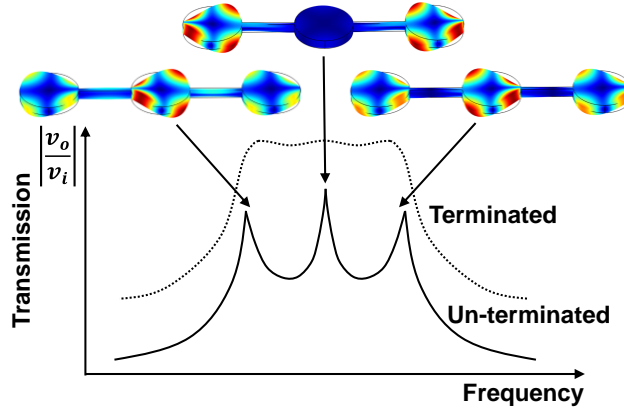
Figure 5.1: Mode shapes of a three-resonator flexural micromechanical coupled filter and its terminated and un-terminated frequency response.

filter performance. After going through the fabrication process of capacitive-gap polysilicon flexural mode disk resonators in Section 5.4, Section 0 then confirms high-Q and low motional resistance of flexural mode disk resonator array composites, demonstrates the effectiveness of quasi-zero length coupling technique, and finally verifies the filter design method by comparing the measurement results with simulation data.

5.1. Flexural Mode Disk Resonators

The mechanically coupled filter in this chapter employs capacitive-gap transduced flexural-mode disk resonators, as shown in Figure 5.2(a), which provides better electromechanical transduction efficiency at the frequency range of interest and allows for flexible phasing design of input and output signals — something very important to reduce output feedthrough current and improve filter's stopband rejection. The flexural-mode disk resonator comprises a 2.5 µm-thick (t = 2.5 µm) polysilicon disk suspended 50 nm (specified by fabrication process) above its capacitive transducer electrodes. In order to minimize anchor induced losses due to misalignments between disk structure and anchor, the filter structure in this chapter employs side-supported flexural-mode disk resonators rather than the center stem supported ones [8].

The flexural-mode disk resonator operates similar to previous capacitive-gap transduced micromechanical resonators [8] [11]. The combination of an ac voltage v_i applied to the input electrodes and a dc-bias voltage V_P applied to the conductive polysilicon resonant structure together induce an electrostatic actuation force which drives the disk into a flexural-mode resonance, when the frequency of v_i matches the resonance frequency. Once vibrating, the V_P-biased time varying capacitance between the disk and its output electrodes generates an output current $i_o = V_P(\partial C/\partial z)(\partial z/\partial t)$, where $\partial C/\partial z$ is the electrode-to-resonator overlap capacitance difference per z-direction gap spacing change. The electrodes in such devices are independently accessible (for phase flexibility) and identical in size, which help to generate symmetric electrostatic force distribution and cancel
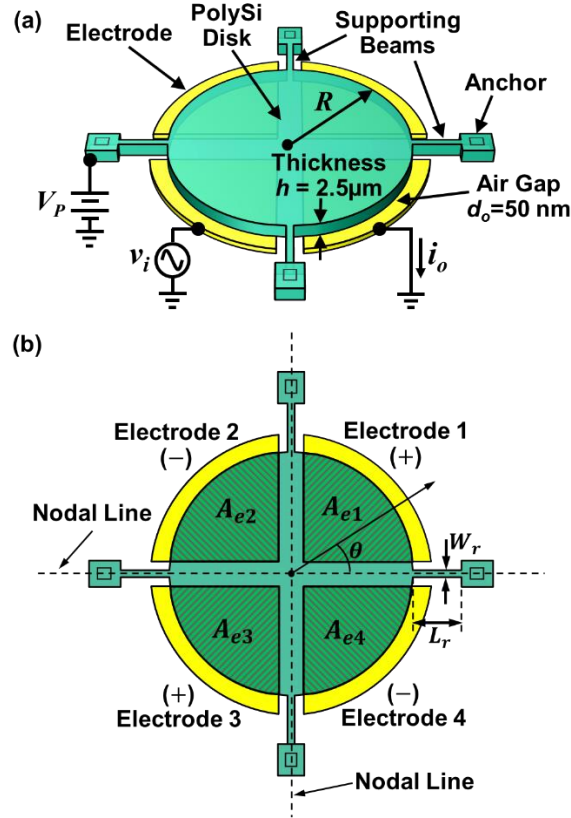
Figure 5.2: (a) Perspective-view schematic of a side-supported 2nd order flexural-mode disk resonator in a classic two-port excitation and sensing configuration. (b) Top-view schematic of the same device.

feedthrough current. By using side support for the disk structure, dc-bias can access the resonator body via side supporting beams, leaving more area for I/O electrodes to enhance electromechanical transduction efficiency.

As shown in the FEM modal response of flexural-mode disk resonators in Figure 5.3(a), each supporting beam aligns with one of the nodal diameters, where the vibration is only torsional (no vertical motion), making the beam attachment points an effective quasi-nodal points. Minimal vibration energy dissipates via supporting beams to the substrate due to near-zero displacement, resulting in higher Q for such device, hence, better stand-alone R_x than a clamped-clamped beam type of resonator. The number of nodal diameters in a mode shape actually indicates the order of the flexural-mode vibration. More nodal diameters appear in higher order flexural-mode shape, i.e., Figure 5.3(b) presents an FEM simulated 3rd order flexural-mode shape with three nodal diameters.

5.1.1. Mode Shape and Resonance Frequency

The flexural mode shape of a free-edge disk structure in a polar coordinates (where the origin coincide with the center of the disk) takes the following expression [49]:
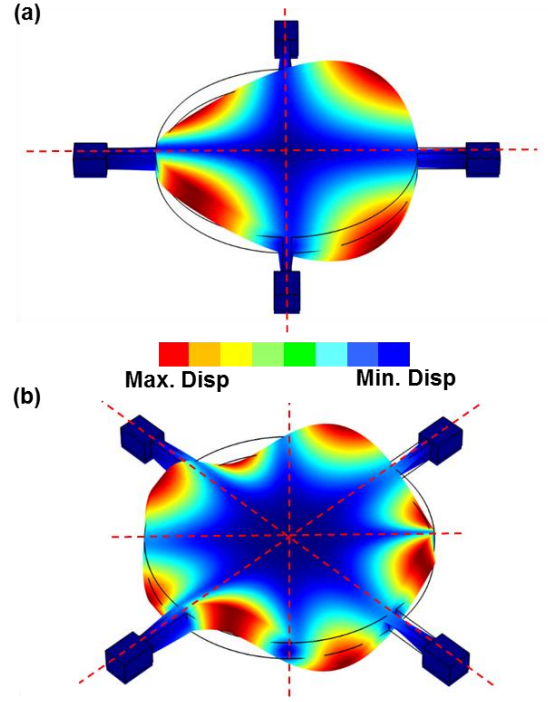
Figure 5.3: (a) FEM simulated 2nd order flexural mode shape of a 20MHz side supported disk resonator with 16 μm radius and 2.5 μm thickness. (b) FEM simulated 4th order flexural mode shape of the same disk resonator at 77MHz. Here, the dashed lines indicate the nodal diameter positions of each corresponding mode shape.

$$Z_{mode}(r, \theta) = \left(J_n \left(\frac{\lambda_{n,s} r}{R} \right) + \frac{C_n}{A_n} I_n \left(\frac{\lambda_{n,s} r}{R} \right) \right) \sin n\theta \qquad (5.1)$$

where (r, θ) is the polar coordinates of a particular point of interest on the disk, R is the radius of the disk, n and s represents the number of nodal diameters and nodal circles, respectively, in a mode shape of interest, J_n and I_n are the nth order Bessel functions of the first kinds and modified Bessel functions of the first kinds, respectively. $\lambda_{n,s}$ and C_n/A_n are generally a function of the boundary conditions of the disk (free edge in this case), Poisson's ratio and the order of the mode shape. The mode shape order can be identified by the number of nodal diameters n and the number of nodal circles s. For the flexural mode shape with zero nodal circles and two nodal diameters ($n = 2$, $s = 0$) that will be discussed in details in this chapter, the numeric value of $\lambda_{2,0}$ and C_2/A_2 are 2.29 and 0.461, respectively, for polysilicon structure material [49] [50].

The nominal resonance frequency f_{nom} for a disk vibrating in flexural mode takes the form [50]:

$$f_{nom} = \frac{\lambda_{n,s}^2}{2\pi} \sqrt{\frac{E}{12\rho(1 - \nu^2)} \frac{h}{R^2}} \qquad (5.2)$$

where h is the structure thickness, E, ρ, and v are the Young's modulus, density, and Poisson ratio, respectively, of its structural material. Note that (5.2) represents the mechanical natural frequency of the disk with zero dc-bias voltage applied (i.e., no electromechanical coupling). The actual resonance frequency f_o during operation will be slightly different from the natural frequency f_{nom} due to the effect of electrical stiffness, which takes the following form [51]:

$$f_o = f_{nom}\sqrt{1 - \frac{k_e}{k_m}} \tag{5.3}$$

where k_e/k_m is a parameter representing the effective electrical-to-mechanical stiffness ratio integrated over the area of electrodes, given by

$$\frac{k_e}{k_m} = N_e \iint_{A_e} \frac{\epsilon V_P^2}{d(r,\theta)^3 k_m(r,\theta)} dr d\theta \tag{5.4}$$

where ϵ is the permittivity in the gap, V_P is the dc-bias voltage, N_e is the total number of electrodes, A_e is the electrode-to-resonator overlap area for each electrode as shown in Figure 5.2(b), and $d(r, \theta)$ is the electrode-to-resonator gap spacing which varies as a function of location (r, θ) on the disk due to V_P-induced forces that statically deflect the disk [52] [53]. $k_m(r,\theta)$ in (5.4) represents the mechanical stiffness in the vertical direction with zero dc-bias voltage (i.e., $V_P = 0$) at location (r, θ) [52]:

$$k_m(r,\theta) = (2\pi f_{nom})^2 m_m(r,\theta) \tag{5.5}$$

where $m_m(r,\theta)$ is the equivalent mass at a given point (r,θ) that can be obtained from the total kinetic energy of the disk divided by one-half of the squared velocity at the point of interest, as shown below:

$$m_m(r,\theta) = \frac{KE_{tot}}{\frac{1}{2}v(r,\theta)^2} = \frac{\frac{1}{2}\iint_{A_r} \rho h [v(r',\theta')]^2 dr' d\theta'}{\frac{1}{2}v(r,\theta)^2} \tag{5.6}$$

where A_r is the disk surface area, $v(r,\theta)$ is the velocity of the z-direction vibration at location (r,θ) given in phasor form by:

$$V(r,\theta) = \dot{Z}(r,\theta) = j\omega_o K Z_{mode}(r,\theta) \tag{5.7}$$

where K is a scaling constant dependent on electrostatic force applied on the disk. Plugging (5.1) and (5.7) into (5.6), the z-direction equivalent mass for a flexural mode disk becomes:

$$m_m(r,\theta) = \frac{\rho h \iint_{A_r} [Z_{mode}(r',\theta')]^2 r' dr' d\theta'}{[Z_{mode}(r,\theta)]^2} \tag{5.8}$$
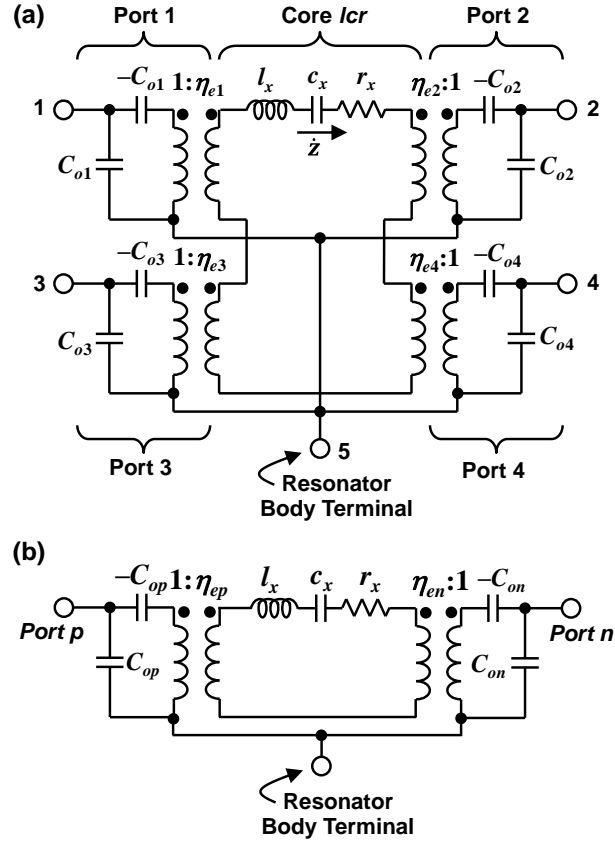
Figure 5.4: (a) Negative capacitance small-signal equivalent circuit for a four-port capacitive-gap transduced flexural-mode disk resonator, such as that of Figure 5.2(a), when operating in the 2nd order flexural mode shown in Figure 5.3(a); (b) Modified equivalent circuit for the same flexural-mode disk resonator with electrodes of the same phase lumped together.

5.1.2. Equivalent Circuit

To conveniently model and simulate the behavior of the flexural-mode disk resonator, Figure 5.4(a) provides an improved electrical small signal equivalent circuit which employs a negative capacitance to clearly predict the k_e dependent resonance frequency. Expressions of the element values in the electrical equivalent circuit take the following form [25]:

$$C_{oi} = \frac{\epsilon A_{ei}}{d_o}, l_x = m_{re}, \ r_x = c_{re}, \ c_x = \frac{1}{k_{re}} \tag{5.9}$$

where C_{oi} is the electrode-to-resonator overlap capacitance, A_{ei} is the electrode-to-resonator overlap area, ϵ is the dielectric constant of the capacitive gap material (vacuum in this case), and m_{re}, k_{re}, c_{re}, are the equivalent mass, mechanical stiffness, damping, respectively, at the highest velocity point on the edge of the disk, which can be obtained by:

$$m_{re} = m_m(R, \pi/4), k_{re} = \omega_{nom}^2 m_m(R, \pi/4), c_{re} = \frac{\omega_{nom} m_m(R, \pi/4)}{Q} \tag{5.10}$$

where ω_{nom} is the angular natural frequency of the disk structure with no dc-bias voltage V_P applied, Q is the quality factor, and $m_m(R, \pi/4)$ is the equivalent mass of the resonator at the highest velocity point as shown in Figure 5.3(a). In addition, when determining the dynamic mass m_{re} of a disk operating in its nth order flexural mode, the integral formulation of (5.8) will yield the same factor χ modifying the physical mass of disk for that value of n, regardless of disk radius. In other words, for an nth order flexural mode disk of any radius, the dynamic mass expression in (5.8) reduces to:

$$m_{re} = \chi M_{tot} = \chi \rho \pi R^2 h \tag{5.11}$$

where $\chi = 0.170$ for the 2nd order flexural-mode disk that this work focuses on. In the physically consistent model of Figure 5.4(a), the transformer turns ratio that represent electromechanical coupling take the expression

$$\eta_{e,i} = V_P \frac{\partial C_{oi}}{\partial z} = V_P \kappa_i \frac{C_{oi}}{d_o} \tag{5.12}$$

which is identical for all ports because of symmetry. The change in electrode-to-resonator overlap capacitance per unit displacement $\partial C_{oi}/\partial z$ is given by:

$$\frac{\partial C_{o,i}}{\partial z} = \left[\iint_{A_{e,i}} \iint_{A'_{e,i}} \frac{Z_{mode}(r,\theta)}{Z_{mode}(r',\theta')} \frac{\epsilon^2 k_{re} r' dr' d\theta'}{[d(r',\theta')d(r,\theta)]^2 [k_r(r',\theta')]} r dr d\theta \right]^{1/2} \tag{5.13}$$

In practice, the complexity of the expression for dc-bias-induced static plate bending of the square resonator $d(r, \theta)$ often precludes convergence of (5.13) when evaluated via computer. Fortunately, the use of the complete form of $d(r, \theta)$ is often not necessary, as substitution of $d(r, \theta)$ and $d(r', \theta')$ with the static d_o yields sufficiently accurate results, yielding the following expression:

$$\frac{\partial C_{o,i}}{\partial z} = \left[\iint_{A_{e,i}} \iint_{A'_{e,i}} \frac{Z_{mode}(r,\theta)}{Z_{mode}(r',\theta')} \frac{\epsilon^2 k_{re} r' dr' d\theta'}{d_o^4 [k_r(r',\theta')]} r dr d\theta \right]^{1/2} \tag{5.14}$$

Combining (5.12), (5.13), and (5.14) yields the expression of the dimensionless ratio κ_i — a factor that modifies the (easy to remember) electromechanical coupling of an ideal parallel-plate capacitive-gap transducer to account for a non-constant resonance displacement (or velocity) profile over the electrode area.

$$\kappa_i = \frac{\left[\iint_{A_e} \iint_{A'_e} \frac{Z_{mode}(r,\theta)}{Z_{mode}(r',\theta')} \frac{k_{re} r' dr' d\theta'}{[k_r(r',\theta')]} r dr d\theta \right]^{\frac{1}{2}}}{A_{e,i}} \tag{5.15}$$

Reflecting the *lcr* through the transformer at a particular port (with all other ports grounded) can generate the effective electrical impedance as the following:

$$L_x = \frac{m_{re}}{\eta_{e,i}^2}, \quad C_x = \frac{\eta_{e,i}^2}{k_{re}}, \quad R_x = \frac{c_{re}}{\eta_{e,i}^2} \tag{5.16}$$

Of the elements in (5.16), the series motional resistance R_x is the most important one in reducing a filter's termination resistance R_Q, which helps to match a filter directly to antennas that usually has impedance range between 50 Ω to 377 Ω in wireless communication applications.

5.2. Flexural Mode Disk Array Composites

As discussed in Chapter 4, a micromechanical disk array composite can lower the motional resistance R_x by summing together the in-phase output current from each mechanically coupled resonators [8]. In addition, the coupled micromechanical disk array increases the device's equivalent stiffness, as will be discussed later in this session, which is essential to lower the coupling beam to resonator stiffness ratio and achieve a narrowband filter.

5.2.1. Schematic and Equivalent Circuit of Flexural Mode Disk Arrays

Figure 5.5 presents a one dimensional (1D) two-port micromechanical flexural-mode disk array composite constructed by mechanically linking individual disk resonators via very short rotational coupling beams and electrically combining resonator's input/output electrodes to generate I/O ports. Here, coupling of resonators yields a multi-mode system, where at each mode, all resonators vibrate at the exact same frequency [16], allowing their outputs to be combined to boost input and output currents, thereby decreasing the motional resistance and increasing power handling. As the beam coupling in an array is generally stronger compared with weak coupling in applications such as narrowband filers [37], an ABCD matrix model will be necessary to capture an array's mechanical performance accurately, rather than a simplified T-network model [16]. As shown in Figure 5.6, a rotational coupler can be modeled as an acoustic transmission line—the mechanical analog to the familiar electrical transmission line that takes the following expression by using an ABCD matrix:

$$\begin{bmatrix} \tau_1 \\ \dot{\varphi}_1 \end{bmatrix} = \begin{bmatrix} A & B \\ C & D \end{bmatrix} \begin{bmatrix} \tau_2 \\ \dot{\varphi}_2 \end{bmatrix} = \begin{bmatrix} cos(\alpha l_c) & jZ_m sin(\alpha l_c) \\ \dfrac{jsin(\alpha l_c)}{Z_m} & cos(\alpha l_c) \end{bmatrix} \begin{bmatrix} \tau_2 \\ \dot{\varphi}_2 \end{bmatrix} \tag{5.17}$$

where τ_i and $\dot{\varphi}_i$ are the torque and angular velocity at corresponding ports, l_c is the length of the rotational coupling beam. Z_m and α in (5.17) are acoustic characteristic impedance and acoustic wave propagation constant, respectively, which take the following forms [8]:
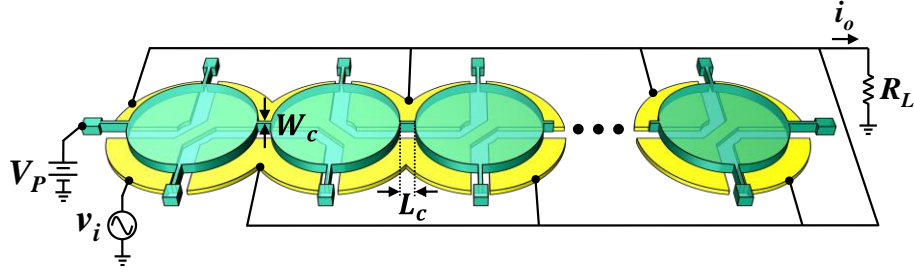
Figure 5.5: Schematic of a one-dimensional flexural-mode disk array composite with disks linked by mechanical couplers to enforce same resonance frequency for each individual resonator.

Rotational Mechanical Coupler

$$\begin{bmatrix} \tau_1 \\ \dot{\varphi}_1 \end{bmatrix} = \begin{bmatrix} cos(\alpha l) & jZ_m sin(\alpha l) \\ \dfrac{jsin(\alpha l)}{Z_m} & cos(\alpha l) \end{bmatrix} \begin{bmatrix} \tau_2 \\ \dot{\varphi}_2 \end{bmatrix}$$

Electrical Transmission Line

$$\begin{bmatrix} v_1 \\ i_1 \end{bmatrix} = \begin{bmatrix} cos(\beta l) & jZ_o sin(\beta l) \\ \dfrac{jsin(\beta l)}{Z_o} & cos(\beta l) \end{bmatrix} \begin{bmatrix} v_2 \\ i_2 \end{bmatrix}$$
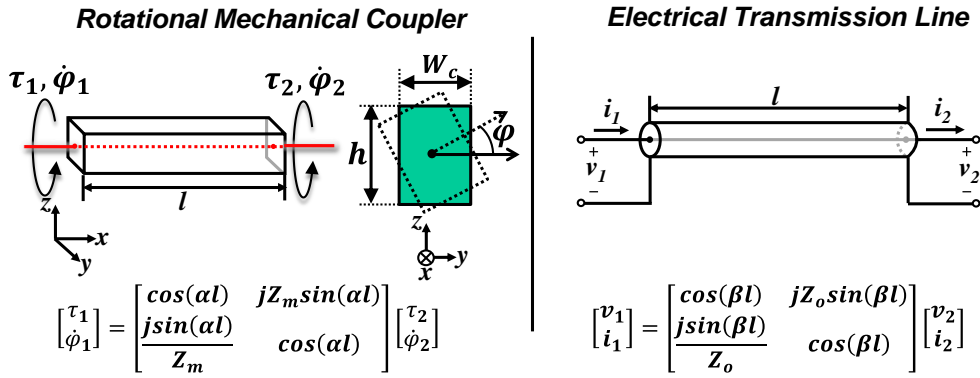
Figure 5.6: Two-port modeling of a mechanical rotational coupling beam in analogy to an electrical transmission line.

$$\alpha = \frac{\omega}{v_e} = \frac{\omega}{\sqrt{\dfrac{G}{\rho} \cdot \dfrac{\gamma}{J_s}}} = \frac{2\pi}{\lambda}, Z_m = \gamma\sqrt{G\rho} \tag{5.18}$$

where ω is the radian frequency of the acoustic wave, v_e is the acoustic velocity, λ is the wavelength of the acoustic wave propagating in the coupling beam, ρ is the material density, G is the shear modulus of the beam material, J_s is the polar area moment of inertia of the beam cross-section about its centroid, and γ is the torsional constant, which is slightly different from the polar area moment of inertia due to cross-section warping associated with non-circular cross-sections [54]. The rotational acoustic wave velocity in the coupling beam is determined by γ and J_s together, which are given by:

$$\gamma = \beta ab^3 = \beta W^3 h$$
$$J_s = \frac{ab(a^2 + b^2)}{12} = \frac{Wh(W^2 + h^2)}{12} \tag{5.19}$$

where a and b are the long side length and short side length of the rectangle cross-section of the coupling beam, respectively, W is the coupling beam width, h is the coupling beam thickness, β is a constant related to the long side length to short side length ratio of a
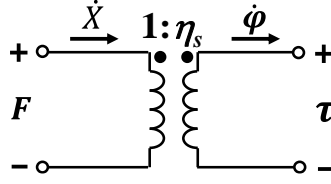
Figure 5.7: Schematic of a displacement transformer that converts linear displacement variables (F, $\dot{X}$) to torsional variables (τ, $\dot{\varphi}$), or vice versa.

rectangular cross-section, which equals approximately 0.209 for $W_s = 1.5$ μm, and $h = 2.5$ μm in our case [55].

As shown in Figure 5.5, the rotational coupling beams connect to the resonators' edge along their nodal diameters where the vibration is purely torsional, instead of connecting to the maximum linear displacement point where the equivalent *lcr* tank is modeled. Therefore it is necessary to employ a displacement transformer that converts torsional variables to linear displacement variables or vice versa to bridge the resonators' *lcr* equivalent circuit model and the rotational beams' ABCD matrix model. As shown in Figure 5.7, the ratio of linear velocity at the maximum displacement point ($R, \pi/2n$) (where the *lcr* tank is modeled) to angular velocity at the coupling location ($R, 0$) determines the displacement transformer turn ratio η_s, which takes the following expression:

$$\eta_s = \frac{\dot{X}}{\dot{\varphi}} = \frac{\omega Z_{mode}(R, \frac{\pi}{2n})}{\omega \varphi(R, 0)} = \frac{Z_{mode}(R, \frac{\pi}{2n})}{\varphi(R, 0)} \tag{5.20}$$

where ω is the angular resonance frequency of the disk, φ describes the rotation angle around the radial direction axis of the disk at its perimeter, which takes the expression as:

$$\varphi(R, 0) \approx \frac{1}{R} \frac{dZ_{mode}}{d\theta}\bigg|_{(R,0)} = \frac{n}{R} Z_{mode}\left(R, \frac{\pi}{2n}\right) \tag{5.21}$$

Plugging (5.21) into (5.20) yields the displacement transformer turn ratio η_s as:

$$\eta_s = \frac{R}{n} \tag{5.22}$$

By using the ABCD matrix model for a mechanical rotational coupler and the negative capacitance equivalent circuit of a flexural-mode disk resonator as described in Section 5.1, Figure 5.8 develops an electrical equivalent circuit model of an *N*-resonator flexural-mode array composite that can accurately capture its frequency response. Because an in-phase vibration of two adjacent disk resonators will generate torques with opposite directions on the two sides of the rotational coupler, the two-port ABCD matrix model in Figure 5.8 connects adjacent resonators with displacement transformers of opposite polarities. The mechanical connection of resonators actually realizes a multi-pole filter structure that has *N* vibration modes, where *N* is the number of coupled resonators.
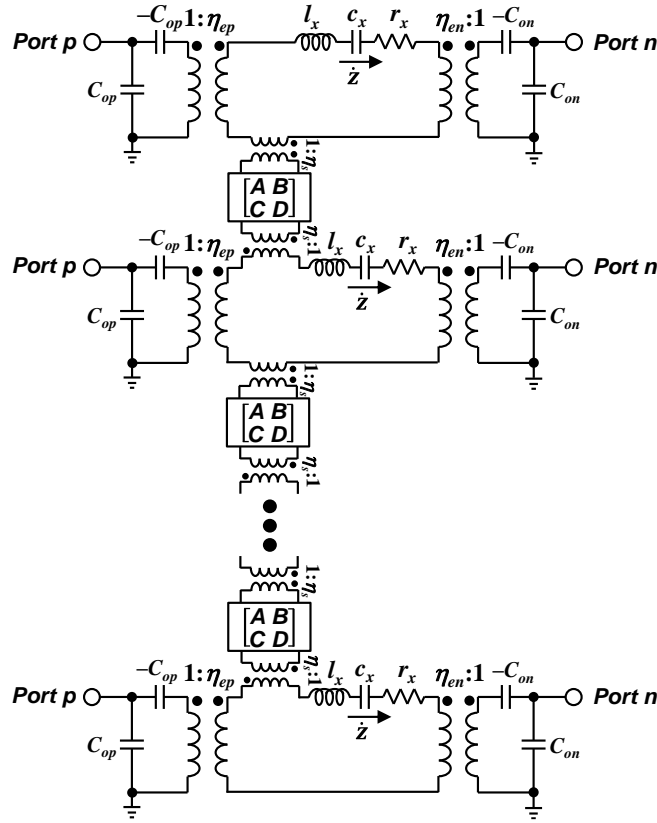
Figure 5.8: Small-signal equivalent circuit of a flexural-mode disk array composite employing two-port ABCD matrix model to capture the behavior of mechanical rotational couplers.

5.2.2. Quasi-Zero Wavelength Rotational Coupling Beams

As first demonstrated in [12], the use of half-wavelength mechanical couplers ensures that all resonators vibrate in phase and ideally spreads undesired modes infinitely away, leaving only one in-phase mode selected. For rotational coupling method, half-wavelength of the acoustic wave in a coupler takes the following expression

$$l_{c,\lambda/2} = \frac{\sqrt{\frac{G}{\rho} \cdot \frac{\gamma}{J_s}}}{2f} = \pi \frac{\sqrt{\frac{G}{\rho} \cdot \frac{\gamma}{J_s}}}{\omega} \tag{5.23}$$

and gives value of 25 μm for polysilicon material at 75MHz. The length of a $\lambda/2$ coupler at this frequency range is approximately $3\times$ the radius of the disk (R=8.4 μm for 2nd order flexural mode), which means a $\lambda/2$ coupled array will occupy much more area compared with the total area of only disks. This is a huge drawback on the fabrication cost of such devices, especially for an array with a large number of coupled single resonators. In addition, a very long suspended coupling beam is also vulnerable to pull-in effect when the
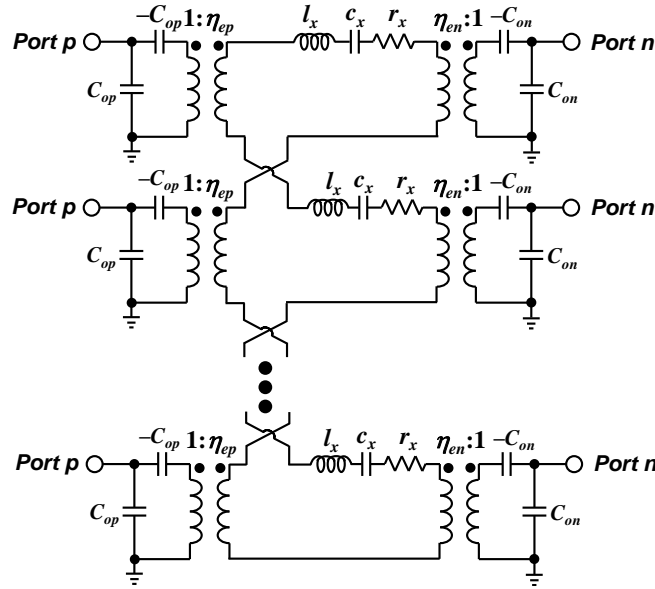
Figure 5.9: Modified equivalent circuit of a flexural mode disk array-composite with zero-wavelength coupling beams.

substrate is biased at a different voltage than the dc-bias V_P applied on the disk body. To overcome these issues and fully utilize the phase flexibility of such flexural mode devices, this dissertation employs a quasi-zero wavelength coupling method that directly attaches adjacent flexural-mode disk resonators, creating an effective zero-wavelength coupling. Plugging $l_c = 0$ into (5.17) yields the torque and angular velocity relationships at the two ends of the rotational coupler as follows:

$$\tau_1 = \tau_2 \, , \dot{\varphi}_1 = \dot{\varphi}_2 \tag{5.24}$$

which shows the torque and angular velocity on the two sides of a rotational coupler will have the same magnitude with the same phase. Such condition indicates that adjacent disk resonators connected by the zero-wavelength coupling beam will vibrate out of phase because of the crisscrossed pins of the ABCD matrix as shown in Figure 5.8, thereby enforcing only the desired out-of-phase mode with all other unwanted modes eliminated. For the case of zero-wavelength coupling, a simple series connection can replace the ABCD matrix and generate a modified N-resonator disk array equivalent circuit as shown in Figure 5.9. To combine the output current, electrodes with opposite signs are connected for adjacent disks because of the out-of-phase motion of the vibration mode selected by zero-wavelength coupling.

5.2.3. Simplified Equivalent Circuit of Array Composites

To further simplify the equivalent circuit model of zero-wavelength coupled disk array composite, series or shunt combinations of a single disk resonator's equivalent circuit
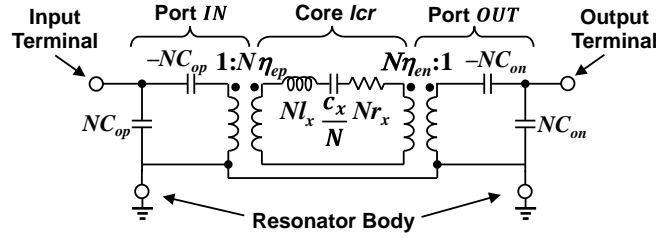
Figure 5.10: Simplified equivalent circuit of a flexural-mode disk array composite with zero-wavelength coupling beams based on element values in the single resonator equivalent circuit in Figure 5.4(b).

element values lead to a lumped equivalent circuit as shown in Figure 5.10. For a disk array with N mechanically coupled disk resonators, the stiffness k_m, mass m_m, damping b_m, electromechanical coupling factor η_{ei}, and electrode-to-resonator overlap capacitance C_{oi} are all N times larger than that of a single disk resonator. Thus, simple multiplication or division by N is all that is needed to derive zero-wavelength coupled array equivalent circuit element values from those of a single disk resonator, as shown in Figure 5.10.

As will be discussed in next section, readers can see the real designed array composites in Table X actually have very short quasi-zero wavelength coupling beams (e.g. $W_c = 1.4$ um, $l_c = 1$ μm) instead of absolute zero wavelength, due to lithography and etching limits. However, as discussed in Chapter 4, such design error will generate negligible impact on an array performance if the array employs appropriate electrode phasing designs and individual resonators with very high Q.

5.3. Flexural Mode Disk Array Filter Design

Figure 5.11 shows the schematic of a 3rd order coupled array filter, comprised of three flexural disk array composites connected by torsional coupling beams. The schematic of the flexural mode disk filter is much like the filter of Figure 5.1, except that instead of single disk resonators, it uses mechanically coupled arrays of vibrating flexural-mode disk resonators, which basically behaves similar to a resonator but with lower motional resistance and higher stiffness, as discussed in Section 5.2, leading to lower termination resistance and smaller bandwidth. Each array composite in Figure 5.11 comprises of N (N = 7) flexural-mode disk resonators that are mechanically coupled via very short beams with high stiffness to force all resonators to vibrate at the same frequency with the out-of-phase mode. The excitation electrodes of the first array (on the left) form the input electrode of the filter and the electrodes of the third array form the output electrode, with all other electrodes either used as tuning electrodes or negative I/O electrodes if the filter is configured for a differential measurement setup. The signal v_i applied at the input with source resistance R_Q serves as one of the termination resistances to flat the filter passband. When the frequency of v_i falls within the filter passband, the mechanical structure vibrates with an overall mode shape that combines those of Figure 5.1, which creates a motional output current passed through the output termination resistor and generates the output voltage. By employing filter couplers in between array composites with specific lengths
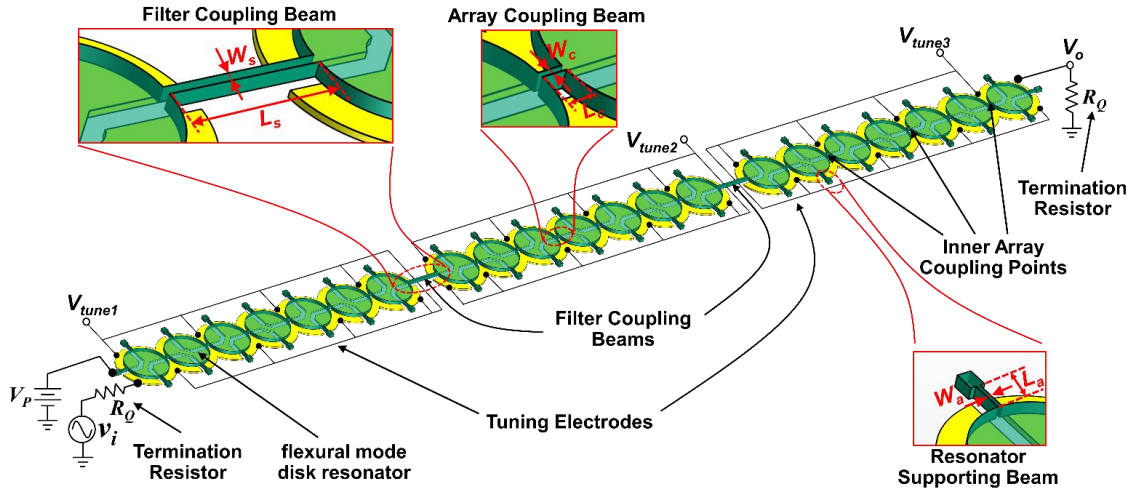
Figure 5.11: Parallel projection view of a 3rd order coupled array filter utilizing three mechanically coupled arrays with 7 resonators in each array composite (i.e., N =7).

(e.g., odd number times of $\lambda/4$), such mechanical coupled filter can achieve narrow bandwidth with tolerance on errors from design and fabrication process.

5.3.1. C_x/C_o — Contributor to Filter Passband Distortion

Any resonator targeting the needs of an RF channel-selecting filter must possess sufficient input/output (I/O) electromechanical transduction efficiency to overpower feedthrough currents that would otherwise compromise the filter response. Here, the ratio of C_x/C_o [56] provides a convenient measure of an electromechanical transducer strength, where C_x can be obtained from (5.16) and C_o represents the total overlap electrode-to-resonator capacitance for a flexural-mode disk resonator. The value of C_x/C_o needs to exceed the percent bandwidth of a filter to avoid excessive passband distortion. The degree by which it must exceed the percent bandwidth depends upon the filter type and order, i.e., the number of resonators used. For example, a rule of thumb to avoid passband distortion for a 3rd order Chebyshev filter upon proper termination stipulates that (C_x/C_o)'s of the I/O resonators should be 2.5$\times$ larger than the filter percent bandwidth [57].

For capacitive gap resonators, the value of C_x/C_o's is related to the mechanical mode shape. The mechanically coupled filter in this dissertation employs flexural-mode disk type of resonators which can provide sufficient input/output (I/O) electromechanical coupling at the frequency range of interest to realize a filter passband response with little distortion. As shown in Figure 5.13, at resonance frequency range below 200 MHz (frequency range of interest in this work is around 75 MHz), clamped-clamped beam (CC-beam) and flexural-mode disk types of resonators have better coupling coefficient compared with contour mode and wine glass mode disk resonators, at the condition of 40 nm gap spacing and 15 V dc-bias voltage. The mechanically coupled filter in this dissertation chooses flexural mode disk type resonators rather than CC-beam resonators mainly because CC-beam resonators usually have lower Q (less than 8,000), which leads to more insertion loss.
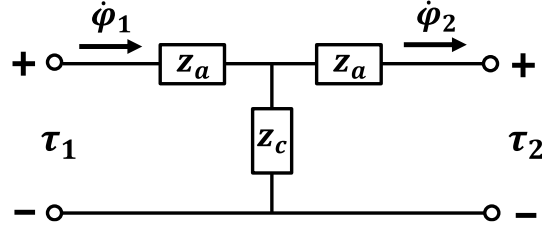
Figure 5.12: A general transmission line T-network model for a mechanical coupling beam in rotational mode.
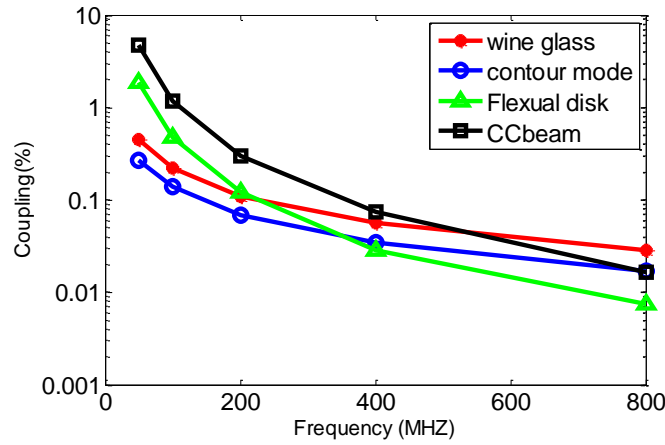
Figure 5.13: Electromechanical transduction efficiency (C_x/C_o) for different types of capacitive-gap resonators at frequency range between 50 MHz and 800 MHz, with conditions of 40nm gap and 15V dc-bias voltage.

To clearly identify factors that affect a resonator's electromechanical transduction efficiency, the following expression estimates the electromechanical coupling coefficient of a flexural mode disk resonator and shows the available knobs to improve it:

$$\frac{C_x}{C_o} \approx \frac{V_P^2}{d_o^3} \cdot \frac{\kappa_i^2 \epsilon}{\omega_{nom}^2 \chi \rho h} \tag{5.25}$$

where ϵ is the permittivity of gap spacer, which is vacuum in this case; ω_{nom} is the flexural mode natural frequency of the disk; χ relates the ratio of static mass of the disk to its dynamic mass [25]; and κ_i is a dimensionless factor that modifies the electromechanical transduction strength of an ideal parallel-plate capacitive-gap transducer to account for a non-constant resonance displacement profile over the electrode area. Here, with same resonance frequency, the dc-bias voltage V_P and spacing d_o across the I/O electrode-to-resonator gaps are clearly the strongest knobs, with the former having a quadratic effect, and the latter a whopping third power influence. Given these dependencies, shrinking the gaps from the 90 nm of [47] to the present 50 nm delivers a 5.8× improvement in (C_x/C_o). Assuming a dc-bias voltage of 15 V, the (C_x/C_o) goes from the 0.15% to 0.88% , which is sufficient for the designed three-resonator 0.3% bandwidth filter.

5.3.2. Quarter Wavelength Coupling Beam Design

To facilitate the design of a mechanically coupled narrowband filter, Figure 5.12 shows a general T-network transmission line model of a rotational coupler, corresponding to Equation (5.17). The z parameters of the series and shunt arms are a function of the ABCD matrix elements in (5.17) and take the following expression:

$$z_a = \frac{B}{D+1} = jZ_m \tan\left(\frac{\alpha l_s}{2}\right)$$

$$z_c = \frac{1}{C} = \frac{Z_m}{j\sin(\alpha l_s)}$$

(5.26)

where l_S is the length of the filter coupling beam. Since α and l_s are constant for a narrowband system at frequency ω_o, rewriting z_c in terms of a coupling capacitance c_s yields the following expressions:

$$z_c = \frac{1}{j\omega_o c_s}, c_s = \frac{\sin(\alpha l_s)}{\omega_o Z_m}, k_s = \frac{1}{c_s} = \frac{\omega_o Z_m}{\sin(\alpha l_s)}$$

(5.27)

For a narrowband filter, l_S in (5.27) is designed to be an effective quarter wavelength (odd number of times of $\lambda/4$), mainly for the following three reasons: to minimize bandwidth, to pose zero mass loading on resonance frequency, and to allow maximum tolerance on coupling beam length variations from design and fabrication. As z_c will connect two adjacent resonators' equivalent *lcr* model, its value reveals the strength of the mechanical coupling. z_c in (5.27) actually represents the impedance of an equivalent coupling capacitor c_s, which can be further rewritten as k_s, the equivalent mechanical stiffness of a coupling beam, since capacitance in electrical domain is equivalent to stiffness in mechanical domain. The coupling beam to array composite equivalent stiffness ratio will determine a coupled filter's percent bandwidth. To minimize bandwidth, the absolute value of $\sin(\alpha l_s)$ in (5.27) should reach its maximum value, leads to l_s an equivalent quarter wavelength, as shown in the following expression:

$$l_s = \frac{\frac{\pi}{2}(2m+1)}{\alpha} = \frac{\lambda}{4}(2m+1), (m = 0,1,2,\dots)$$

(5.28)

Combining (5.18) and (5.27), the minimum coupling beam stiffness k_s takes the following expression:

$$k_{s,\frac{\lambda}{4}(2m+1)} = 2\pi \cdot \sqrt{\frac{\gamma}{J_s}} \cdot \frac{\gamma G}{\lambda}$$

(5.29)

For an equivalent quarter wavelength coupling condition, z_a and z_c will have the same absolute value but opposite sign. For example, z_a and z_c in (5.26) will turn into the follow expressions for the filter in this chapter that employs $\lambda\backslash 4$ couplers:
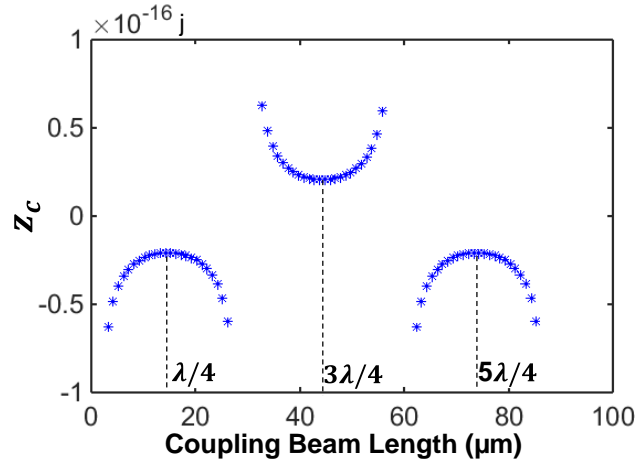
Figure 5.14: Mechanical coupling impedance z_c versus coupling beam length for a flexural-mode disk filter composed of disk resonators vibrating around 70 MHz with radius of 8.4 µm.
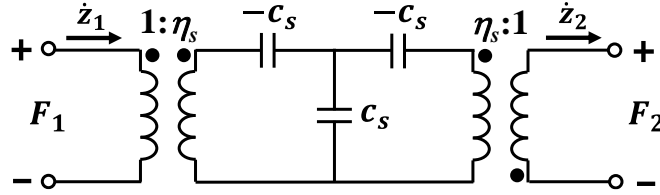
Figure 5.15: Equivalent circuit of a quarter-wavelength rotational coupler. Here, a capacitor c_s can be used to represent the coupling impedance z_c at resonance frequency f_o. The transformer η_s converts linear displacement parameters to torsional parameters, or vice versa.

$$z_a = -jZ_m, z_c = jZ_m \tag{5.30}$$

With same amplitude but negative sign, z_a and z_c will cancel out and generate zero loading effect to its adjacent resonators, This will greatly ease the design of a mechanical coupled filter, since each constituent resonator doesn't need to compensate its frequency shift caused by loading from couplers, meaning each constituent resonator can be identical and designed at the same frequency. In addition, a quarter wavelength design also offers best tolerance against coupling beam variations. As shown in Figure 5.14, the slope of impedance z_c versus coupling beam length approaches zero at quarter wavelength points, meaning a slight change in coupling beam length will not significantly change a filter's bandwidth.

Figure 5.15 shows the equivalent circuit model of a $\lambda/4$ rotational coupling beam, comprised of two displacement transformers and a T-network model that employs capacitor c_s to represent z_a and z_c. The two ports of this equivalent circuit will directly connects to the core *lcr* tank model of an array composite, which will be shown in the next session.
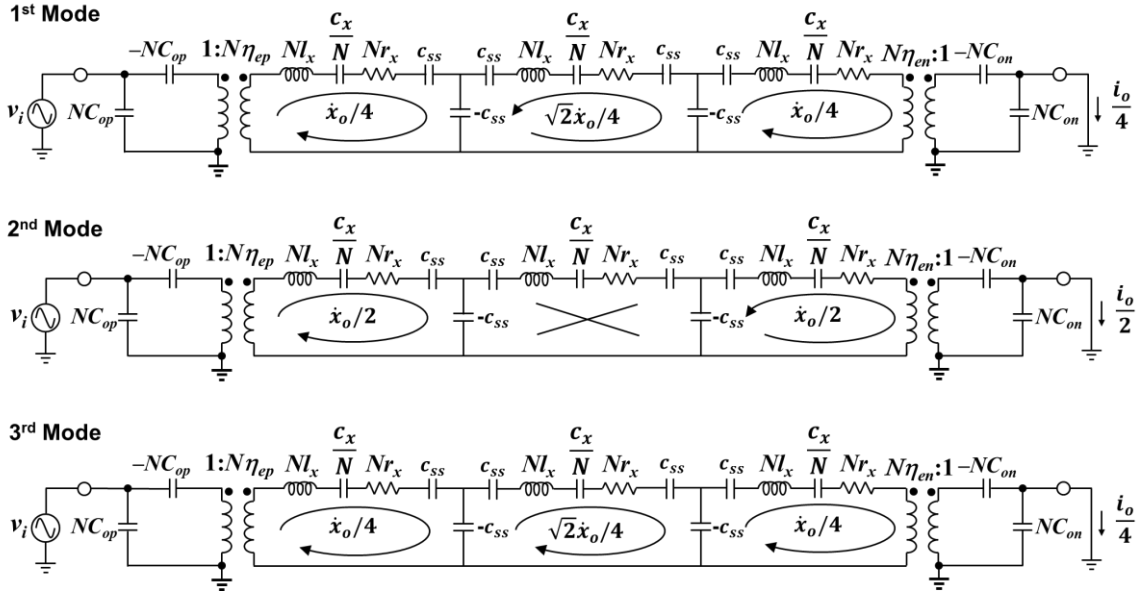
Figure 5.16: Equivalent electrical circuits of a 3rd un-terminated coupled array filter ($N = 7$), which show the motion of constituent array composites for each resonance mode.

5.3.3. Filter Equivalent Circuit

Figure 5.16 presents the equivalent circuit of a 3rd order coupled array filter, where the *lcr* tanks model the array composites, the capacitor T-networks represent the $\lambda/4$ coupling beams, and the transformers η_e model the electromechanical transduction. Here, the capacitor T-network absorbs the displacement transformer into it and leads to a new parameter c_{ss} with the following expression:

$$c_{ss} = \eta_s^2 c_s, \, k_{sij} = 1/c_{ss} \tag{5.31}$$

where η_s represents the displacement transformer turn ratio and k_{sij} is the equivalent linear stiffness of the rotational coupling beam between the ith and jth resonator.

Being a high quality factor system with Q larger than 10,000, all array composites will reach their maximum displacement simultaneously, either in-phase or out-of-phase with each other. Figure 5.16 presents a simplified unterminated filter equivalent circuit with tuning electrodes neglected (the case when tuning electrodes have the same voltage). The current in each individual mesh represents the motion of arrays in each mode. With all meshes resonating at the same frequency for each mode, the motional current and resonance frequencies for each mode can be determined by using Kirchhoff law. The percent bandwidth of the coupled filter is proportional to the ratio of the array's equivalent capacitor to the coupling capacitor, which can be written as the following expression.
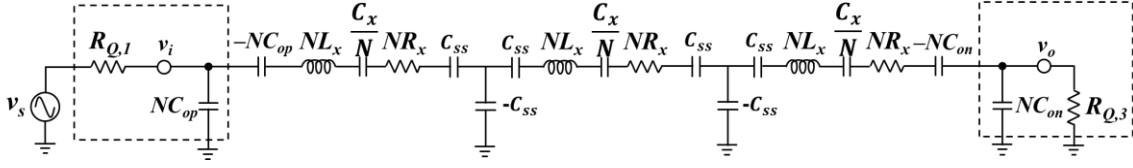
Figure 5.17: Simplified equivalent electrical circuit of a terminated 3rd coupled array filter ($N = 7$). Here, the termination resistor $R_{Q,i}$ at the input and output ports form a low pass filter that could potentially distort passband response if the cut-off frequency is very close to the center frequency.

$$\frac{BW}{f_o} = \frac{1}{k_{ij}} \cdot \frac{c_x}{Nc_{ss}} = \frac{1}{k_{ij}} \cdot \frac{k_{sij}}{Nk_{re}} \tag{5.32}$$

where k_{ij} is the normalized coupling coefficient between resonator tanks for a given filter type (i.e., Butterworth, Chebyshev, etc.) [4], k_{sij} stands for the coupling beam stiffness between the ith and jth arrays, N is the number of resonators in an array, and k_{re} is the equivalent stiffness of a single flexural-mode disk resonator. For the same coupling beam, Equation (5.32) shows that an N-resonator array will reduce the percentage bandwidth by N times than that achieved by a stand-alone resonator. This will ease the fabrication of narrowband coupled filters since designers just need to increase the number of resonators in an array to achieve a narrow bandwidth, instead of significantly shrinking the beam width and challenging the lithography limit.

With $\dot{x}_o$ representing the velocity amplitude of an N-resonator array when the same input voltage v_i and dc-bias voltage V_P as the filter applies, Figure 5.16 shows that the output current from the 3rd array for the 2nd mode will be $\sqrt{2} \times$ larger than the other two modes. The following equations also show that the equivalent resistance r_{eq} for the center resonance mode is $2 \times$ smaller than the other two modes. Both of these indicate that the central resonance peak in the unterminated filter frequency response (S21) will be 6 dB higher than the two side peaks, as will also be shown in Figure 5.25 in Section 0.

$$r_{eq,1} = \frac{P_{tot}}{\left(\frac{\dot{x}_o}{4}\right)^2} = \frac{\left(\frac{\dot{x}_o}{4}\right)^2 + \left(-\frac{\sqrt{2}}{4}\dot{x}_o\right)^2 + \left(\frac{\dot{x}_o}{4}\right)^2}{\left(\frac{\dot{x}_o}{4}\right)^2} r_x = 4r_x$$

$$r_{eq,2} = \frac{P_{tot}}{\left(\frac{\dot{x}_o}{2}\right)^2} = \frac{\left(\frac{\dot{x}_o}{2}\right)^2 + \left(\frac{\dot{x}_o}{2}\right)^2}{\left(\frac{\dot{x}_o}{2}\right)^2} r_x = 2r_x \tag{5.33}$$

$$r_{eq,3} = \frac{P_{tot}}{\left(\frac{\dot{x}_o}{4}\right)^2} = \frac{\left(\frac{\dot{x}_o}{4}\right)^2 + \left(\frac{\sqrt{2}}{4}\dot{x}_o\right)^2 + \left(\frac{\dot{x}_o}{4}\right)^2}{\left(\frac{\dot{x}_o}{4}\right)^2} r_x = 4r_x$$

In real application, to flatten the filter passband and achieve the designed amount of passband ripple, termination resistors at the input and output electrodes will control (i.e., load) the Q's of the end resonators. By reflecting the *lcr* tank and T-network through the outside of the transformer, Figure 5.17 presents a simplified lumped equivalent circuit model of a coupled filter terminated with resistance $R_{Q,i}$ at the two ends. The following expression determines the value of the impedance required to terminate a coupled array filter when the approximation of $Q_r \gg q_i Q_f$ is valid:

$$R_{Q,i} = \left(\frac{Q_r}{q_i Q_f} - 1\right)\frac{R_x}{N} \approx \frac{Q_r}{q_i Q_f} \cdot \frac{R_x}{N}$$

(5.34)

Q_r and Q_f in (5.34) are the array and filter quality factors, respectively, q_i is a normalized Q parameter obtained from a filter cookbook [4]. From (5.34), the use of N-resonator array instead of a single resonator provides an N times reduction in filter termination impedance, as long as Q's of the array composite is sufficiently higher than $q_i Q_f$. As $R_{Q,i}$ is much larger than R_x/N for a narrow band filter, the peak difference is negligible after termination, combining also with the fact that responses from all peaks will couple when effective Q is low. The value of Q_r and Q_f also determines the insertion loss of the filter, which is governed by the following equation.

$$IL = 20 \log\left(\frac{2R_{Q,i} + \frac{2R_x}{N}}{2R_{Q,i}}\right) = 20 \log\left(1 + q_i \frac{Q_f}{Q_r}\right)$$

(5.35)

For a narrowband filter (high Q_f), higher resonator Q_r will lead to smaller insertion loss, as shown in (5.35). For example, for a 200 kHz bandwidth 3rd order Chebyshev filter at 75 MHz, Q's of 10,000 for array composite will lead to a 3rd order filter insertion loss of less than 0.4 dB. The simplified equivalent circuit in Figure 5.17 also indicates that a low pass filter formed by $R_{Q,i}$ and NC_{op} (or NC_{oi}) will process the transmitted signal first, before the signal goes into the actual filter. In order to avoid distortion on transmitted signals, the low pass filter cut off frequency needs to be several times higher than the filter's center frequency, which leads to the following expression:

$$\frac{1}{R_{Q,i}NC_{op}} > K\omega_o$$

(5.36)

Where the ratio K is dependent on the filter type, filter order, and the passband ripple allowed by the user. Combining (5.34) with the equation $Q_r = 1/(\omega_o C_x R_x)$ leads to another form of (5.36) as the following:

$$C_x/C_{op} > K\frac{P_{BW}}{q_i}$$

(5.37)

which is similar as discussed in Section 5.3.1.

TABLE VIII: EQUIVALENT CIRCUIT ELEMENT VALUES OF A 75MHZ 3RD ORDER COUPLED ARRAY FILTER WITH 7 RESONATORS IN EACH ARRAY COMPOSITE

Parameter	Value	Units
N	7	N/A
c_x	2.02×10^{-5}	F
l_x	2.23×10^{-13}	H
r_x	1.64×10^{-8}	Ω
c_{ss}	1.5×10^{-3}	F
C_{on}	14.9	fF
$\eta_{ep} = \eta_{en}$	1.42×10^{-6}	C/m
c_s	8.68×10^{7}	F
η_s	4.2×10^{-6}	m

TABLE IX: IMPEDANCE-EXPLICIT EQUIVALENT CIRCUIT ELEMENT VALUES OF A 3RD ORDER COUPLED ARRAY FILTER WITH 7 RESONATORS IN EACH ARRAY COMPOSITE

Parameter	Value	Units
N	7	N/A
C_x	4.06×10^{-17}	F
L_x	0.11	H
R_x	8.18	kΩ
C_{ss}	1.50×10^{-13}	F
$C_{op} = C_{on}$	14.9	fF
$R_{Q,1} = R_{Q,3}$	10.5	kΩ
$1/(2\pi R_{Q,1} C_{on})$	145.4	MHz

5.3.4. Design Example

This section designs a 75-MHz ($R = 8.4$ µm) 3rd order flexural mode disk array filter which employs three mechanically coupled array composites, with each array contains 7 flexural-mode disk resonators. Table VIII and Table IX summarize the equivalent circuit variables for the constitute array composites and the filter. Compared with a 3rd order filter using coupled single disk resonators, this array filter will have $7\times$ smaller fractional bandwidth, which relaxes the requirement of very thin mechanical couplers and reduces the fabrication challenge. In addition, with smaller termination resistance, this work pushes one more step toward using such filter in a communication system with much lower impedance, e.g., between 50 Ω and 377 Ω.

5.4. Fabrication Process

The fabrication process for this all-polysilicon flexural mode disk array filter is similar to that of [8], with small deviations mainly in that it uses thinner sacrificial oxide layer (50 nm) to enhance the devices' electromechanical transduction efficiency and employs BOSCH based etching process to achieve good sidewall profiles for a 2.5 µm thick structure layer. The process begins with film depositions, lithographic patterning, and
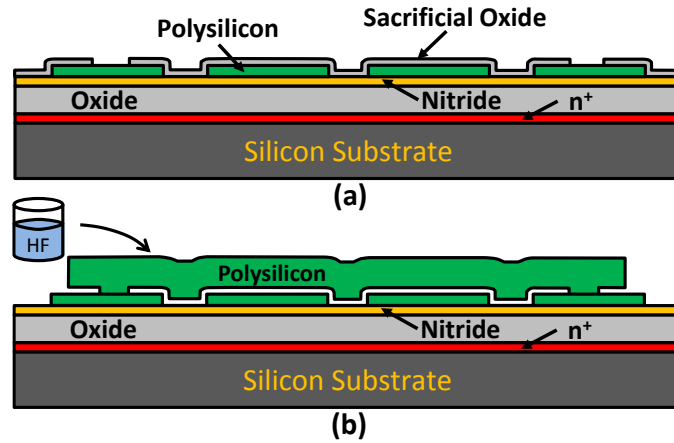
Figure 5.18: Cross-sections showing the last few steps in the fabrication process for an all-polysilicon flexural mode disk resonators with 50nm gap spacing.

etching steps identical to those of [8] to achieve the substrate isolation layer, polysilicon interconnects, and the oxide sacrificial layer. At this point, patterned phosphorus-doped polysilicon electrodes and interconnect are covered by a 50 nm thick sacrificial LPCVD silicon dioxide, as shown in Figure 5.18(a), except at portions dry-etched to serve as anchors for resonators. A 2.5 µm thick in-situ doped polysilicon film is then deposited via LPCVD at 585ºC to serve as the resonators' structural layer, followed by a BOSCH based dry-etch process to define the disks and coupling beams. Since flexural-mode disk resonators have electrode-to-resonator gap at the bottom, the scalloped sidewall profile generated by BOSCH process will not significant impact the filter's performance. Instead, such process will offer straight sidewalls for flexural mode resonators, which will generate less errors in frequency prediction. After the polysilicon structural layer etching, a 30 mins 950 ºC stress and dopant distribution anneal is needed to ensure good quality factor. In the final step of the process, the wafer is dipped into a solution of 49 wt. % hydrofluoric acid to etch away the sacrificial oxide layer, reaching a cross-section as shown in Figure 5.18(b).

Figure 5.19 and Figure 5.20 present a stand-along 20-MHz flexural-mode disk resonator and a 16-resonator 70-MHz disk array composite, respectively. Clearly indicated by Figure 5.20, couplers in between resonators are much shorter compared with the supporting beams, which makes them very stiff to enforce out-of-phase motion of adjacent resonators in an array. Figure 5.21 presents the SEM of a 70MHz 3rd order array filter which couples three array composites with each array contains seven resonators in it. As shown in Figure 5.21, the much longer $\lambda/4$ coupling beam helps the filter achieve minimum bandwidth and highest tolerance against design errors and fabrication process variations. These SEMs also show clear topography in the disk, which might slightly impact the resonance frequency and quality factor. To solve this, future work will employ CMP process to planarize layers after deposition. As shown in the test results in next Section, the quality factor of flexural-mode disk resonators is higher than 10,000 even with topography existing on the surface of the disk.
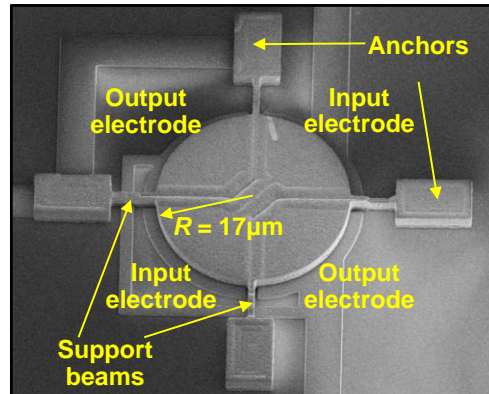
Figure 5.19: SEM of a 20-MHZ (R=17 μm) stand-alone flexural-mode disk resonator with 50 nm capacitive gap spacing.
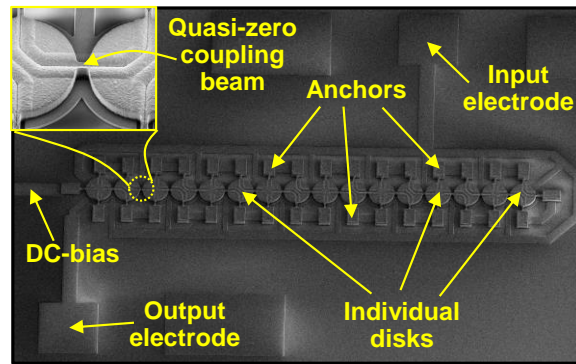
Figure 5.20: SEM of a 70-MHZ 50 nm capacitive-gap flexural-mode disk array composite which employs 16 mechanically coupled resonators.
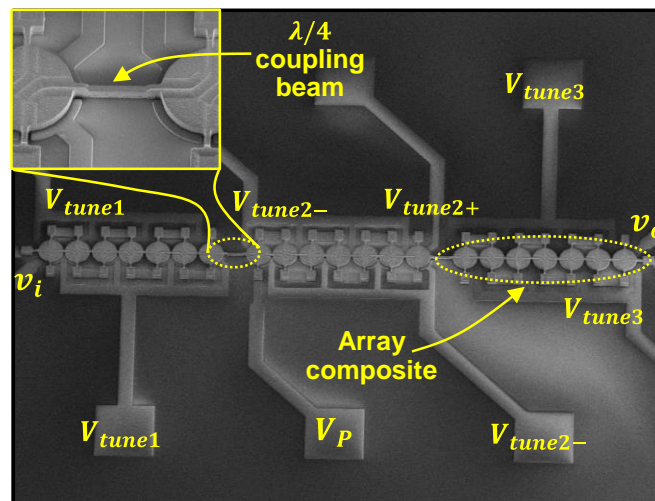
Figure 5.21: SEM of a 70-MHZ 3rd order array filter that couples three array composites with each array employing 7 resonators.
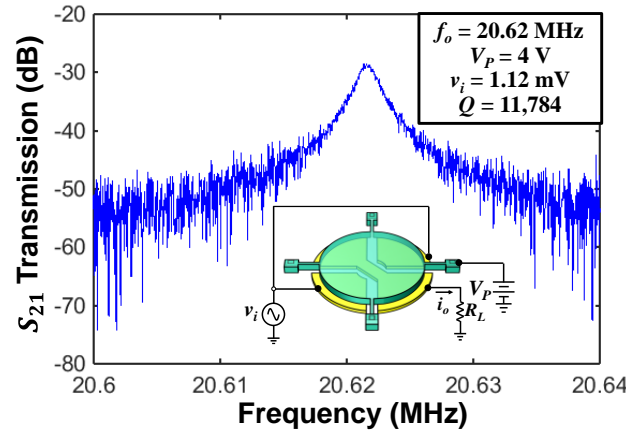
Figure 5.22: Frequency response of a 20MHz 2nd flexural-mode disk resonator (R=16 μm).

5.5. Measurement Results

To demonstrate the efficacy of mechanical coupling techniques in building arrays and filters, measured frequency response of S parameters are in order, for stand-alone flexural-mode disk resonators, mechanically coupled array-composites, and a 3rd order coupled array filter. Although high frequency micromechanical resonators are less susceptible to gas damping, vacuum is still needed to measure Q's above 10,000. Therefore this work measured the fabricated devices under a 2μtorr vacuum environment in a Lakeshore FWPX vacuum probe station. The fabricated devices in this chapter was measured via the two-port measurement mode of an Agilent E5071C network analyzer with measurement plane moved to the probe tips using standard SOLT calibration on a CS-5 substrate.

5.5.1. Stand-Alone Flexural Mode Disk Resonators

Figure 5.22 presents the frequency spectrum of a stand-alone flexural-mode disk resonator with 16 μm radius and 50-nm capacitive gap measured under a 2μtorr vacuum environment with a dc-bias voltage of 4 V. This device exhibits a $Q > 10,000$ at ~20 MHz, which is good enough to suppress phase shift in between constituent resonators in an array composite according to Section 4.2, when design errors and frequency mismatches exist.

A flexural-mode disk resonator can also achieve higher resonance frequency by employing higher order flexural mode with more nodal diameters. Figure 5.23 presents a measured frequency spectrum of a 223-MHz center stem supported flexural-mode disk resonating at the 4th order mode. As indicated in the FEM simulated mode shapes in Figure 5.3, the 4th order mode shape has a larger central area with little displacement, leading to less energy loss via anchors. That's why the 4th order flexural-mode disk can still achieve high Q above 10,000 even its intrinsic quality factor predicted to be lower than that of a lower frequency one (*fQ* product constant at these frequency ranges) [29].
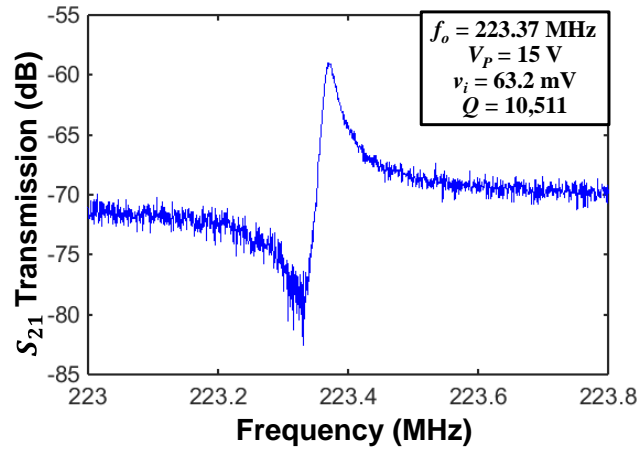
Figure 5.23: Frequency response of an 8.8 µm radius disk resonator vibrating at the 4th flexural mode around 223 MHz.
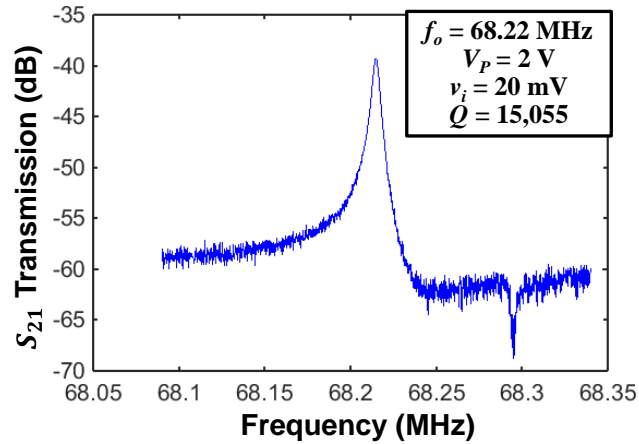
Figure 5.24: Measured frequency response of a 68 MHz (R = 8.8 µm) radius disk array composites with 16 resonators coupled by quasi-zero rotational couplers.

5.5.2. Mechanically-Coupled Flexural Mode Disk Arrays

Figure 5.24 presents the frequency characteristics of a 68-MHz 16-resonator coupled flexural-mode disk array composite measured using two-port configurations under vacuum. With only 2V dc-bias voltage, its motional resistance outperforms what had been achieved with a much higher 25V by similar type stand-alone disk resonators [8], which is mainly enabled by the motional current boost from arraying and the stronger electromechanical transduction from a narrower 50-nm gap spacing. With more than 12× reduction in dc-bias voltage, such array devices can be integrated with IC more easily without the need to generate high dc-bias voltage, e.g. by using MEMS charge pump [58]. Figure 5.24 also clearly shows a single resonance peak with no other significant spurious modes, which
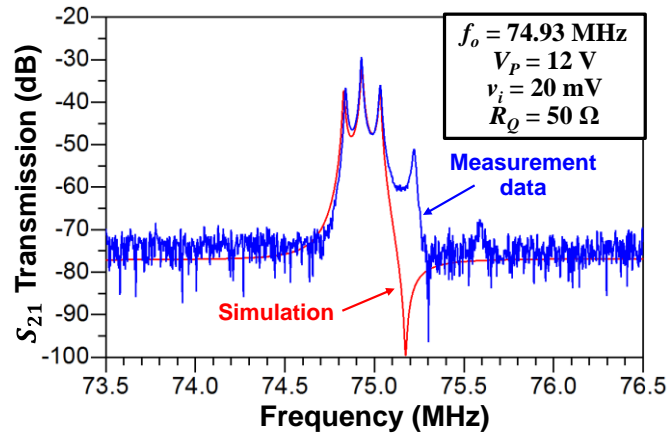
Figure 5.25: Comparison of measured response and simulation data spectrum for the frequency response of a 3rd order array filter with each array composite employing 7 mechanically coupled flexural mode disk resonators.

indicates all other 15 spurious modes are successfully suppressed and thereby demonstrates the effectiveness of the quasi-zero coupler and electrode phasing design. With a very high Q of 15,505, the 16-resonator array composite shows no sign of Q deduction from mechanical coupling, which makes the arraying technique with quasi-zero length couplers a perfect candidate for low insertion loss narrow band filters.

5.5.3. Coupled Array Filters

To verify the design theory and analyze filter performance dependencies, Figure 5.25 compares the measurement results of a 75MHz un-terminated 3rd order array filter with the simulated data using the equivalent circuit in Figure 5.16. In order to match the measured and simulated spectra, several adjustments were made to the original design data in the "Designed" columns of Table X, e.g. the resonance frequency adjustment, the feedthrough capacitance from substrate, and the coupling beam width difference. Since the disk's resonance frequency at flexural modes depends on the polysilicon structure film thickness, which is hard to be precisely controlled during fabrication, the actually measured filter's center frequency shifts from 71.2 MHz to 74.9 MHz. In addition, due to under exposed lithography in the coupler area and etching profile variation, the fabricated coupler width is slightly thinner than the designed value. To match the stopband rejection from the measurement results, the equivalent circuit simulation employs a 3fF feedthrough capacitance connecting between the input and output port to represent the capacitive feedthrough path (electrode-substrate-electrode) for a coupled filter. After these appropriate adjustments, the measured and simulated passbands and shape factors are very similar as shown in Figure 5.25, with the only discrepancies coming from the unexpected spurious resonance peak at the stopband. The spurious mode may be attributable to the coupling topology of the array filter in this work. As shown in the filter schematic in Figure 5.5, the resonators' vibration excited by the input voltage will go through a long path to reach resonators in the output array. As each coupler and resonator may introduce non-

TABLE X: THE DESIGN PARAMETERS, SIMULATION DATA, AND MEASUREMENT RESULTS OF A 3RD ORDER COUPLED ARRAY FILTER

Parameter	Designed/ Simulated	Measured	Units
Center Frequency, f_o	71.2/74.93	74.9	MHz
Bandwidth, BW	218/227	210	kHz
Fractional Bandwidth, (BW/f_o)	0.31/0.30	0.28	%
Insertion Loss, $I.L.$	0.9/1.6	5.5	dB
Passband Ripple, $P.R.$	0.5/1	4.5	dB
20dB Shape Factor, $S.F.$	1.59/1.59	1.46	N/A
Stopband Rejection, $S.R.$	——	40	dB
Termination Resistors, R_Q	11.2/10.5	5.2	kΩ
Quality Factor, Q	15,000/6,500	6500	N/A
DC-Bias Voltage. V_P	15/12	12	V
Filter Coupler Length, L_s	14.9/14.9	14.9	μm
Filter Coupler Width, W_s	1.7/1.4	1.4	μm
Array Coupler Length, L_c	1/1	1	μm
Array Coupler Width, W_c	1.4/1.2	1.2	μm
Res. Beam Length, L_a	3.8/3.8	3.8	μm
Res. Beam Width, W_a	1.4/1.2	1.2	μm
Number of Res. In Array, N	7/7	7	N/A

idealities, such topology will have a high chance of introducing spurious modes or mode shape distortions. In the future, to suppress such spurious response, filters employing different coupling topologies such as rectangular shape or square shape rather than single-line shape, may help to reduce the length of coupling path [46], thereby potentially leading to a cleaner filter response.

Figure 5.25 also shows that the resonance peaks' average Q of 6,500 is not as high as seen in previously measured disk array composites in Figure 5.24, for which Q's higher than 10,000. The following two reasons mainly cause the Q reduction: First, very closely spaced resonance peaks may load the device's quality factor. Second, the combination of simultaneous motion from each coupled resonator affects the overall anchor loss, leading to a higher ratio of energy loss via substrate to vibration energy in the resonator. Nevertheless, an average Q of 6,500 will still achieve a low insertion loss less than 2dB for a 0.3% bandwidth filter at 75MHz. As indicated in Figure 5.25, both simulation and measurement show that the central resonance peak is about 6 dB higher than the two side peaks, which is consistent with the analysis in Section 5.3. After termination, this peak difference will be negligible because of Q loading effect from termination resistances.

During this filter measurement, the E5071C network analyzer provides the virtual termination resistors by using the fixture simulator function. As shown in the terminated filter response in Figure 5.26, two 5.2 kΩ resistors at the I/O ports of the filter together raise the resonance peak level and flatten the passband. As the device is tested using probe station, finite contact resistance and polysilicon trace parasitic resistance may also contribute to part of the equivalent termination resistors, which will make the needed termination resistance smaller than the simulated 10.53 kΩ. The bandwidth of this filter is 210 kHz, which is very close to the designed value of 218 kHz. In addition, by using a higher 3rd order filter, the response reaches a much better roll-off with 20dB shape factor
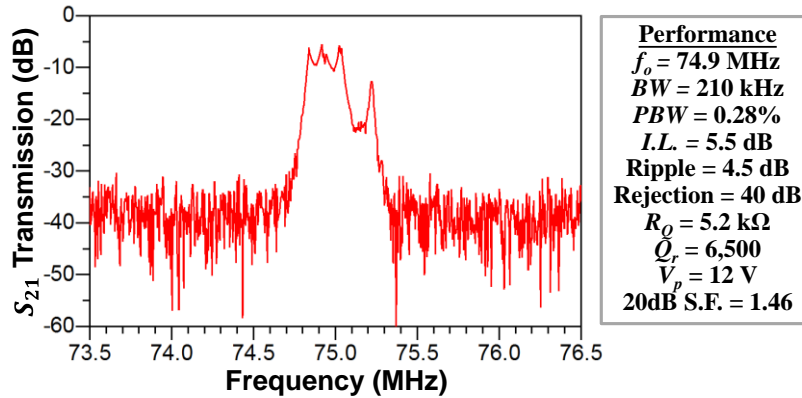
Figure 5.26: Measured frequency response of a terminated 3rd order coupled array filter with 7 resonators in each array composite.

of 1.46, significantly smaller than the values of 2.31 and 2.69 achieved by the 2nd order filter in [52] and [46], respectively, leading to better signal selection for narrowband applications.

Although the frequency spectrum of the 3rd order coupled array filter shows matched response with simulation and impressive sharper roll-off, a more pragmatic inspection of Table X reveals some remaining practical issues. Perhaps the most offensive of these are the large values of termination resistance R_Q (>5 kΩ), which may not only amplifies problems with parasitic capacitance as dictated by (5.36), but also generates more input referred voltage noise. Among the most promising strategies to reduce R_Q are: 1) decreasing the electrode-to-resonator gaps, which leads to lower R_x, 2) using more conductive materials (e.g. metal) for traces and fully integrating the filter with sense electronics.

In addition to the above R_Q issue, the 5.5dB insertion loss of the filter is also larger than the simulated 1.6 dB, which could be attribute to the finite contact resistance and trace resistance that behave as a voltage divider and attenuate the signal. Replacing the trace with metal and using wire bonding measurement set up will have a high chance to solve this problem in the future. The measured filter response also shows a higher passband ripple of 4.5 dB than the designed 1 dB. This can be attributable to the following reasons: 1) the 12 V maximum dc-bias voltage applicable to the device without pull-in is lower than the designed 15 V, which will reduce C_x/C_o value down to 0.64× according to (5.25); 2) parasitic capacitance in the order of 35 fF (according to layout and fabrication process) exists between the electrode and the conductive silicon wafer substrate, which increases the effective total C_o to 139 fF, based on the equivalent circuit elements value in Table VIII. Since this parasitic capacitance will contribute zero electromechanical transduction, it will contribute to another 25% reduction in electromechanical transduction strength. Considering these two factors, the C_x/C_o will reduce to 0.2%, which is smaller than the measured 0.28% percent bandwidth and thereby leading to more passband distortion according to Section 5.3.1.

As indicated in the SEM in Figure 5.21, the fabricated filter actually have differential

input and output ports, which not only improves the electromechanical transduction efficiency C_x/C_o, but also can reduce the feedthrough current. However, due to the fact that the polysilicon bond pads are easily peeled off during wire bonding, this work can only test the coupled array filter using a probe station, which limits the ports number to six and cannot measure the device in a differential mode.

In the future, an improved fabrication process that can reduce interconnect trace resistivity and area, enhance electrode-to-resonator pull-in strength, and improve polysilicon film attachment would render a capacitive-gap MEMS filter with lower insertion loss, smaller termination resistance, and more flattened passband, which may be potentially used in future RF channel select applications. Improvements to each of the above approaches are ongoing and much work still remains in this area.

Chapter 6 Conclusions

RF channel selection enabled by MEMS capacitive-gap resonator array composites with extremely high Qs >30,000 and large numbers of coupled resonators can potentially be a key enabler for software-defined cognitive radios. More importantly, this technology will encourage wireless radio designers to break existing assumptions and open their minds to the possibility of having extremely high Q passive components in abundance, allowing them to use as many high-Q passives as they can, such as building front-end VLSI mechanical circuits. Once this happens, an explosion of new communication architectures and even new wireless standards may ensue, which may in turn greatly enhance the capability of our wireless networks.

6.1. Achievements

This dissertation explored the degree to which MEMS capacitive-gap resonators can be applied in the aforementioned RF channel select applications. The thesis focused on three distinct methods to achieve high Q, high stiffness, and low motional resistance capacitive-gap resonators that can be used as elements for RF narrowband filters. Specifically, the thesis enhanced the capability of the equivalent circuit model of a radial contour mode disk resonator by making two improvements: using transmission line based T-network to predict anchor loss dominated Q and using negative capacitance to clearly capture the frequency pulling effect from electrical stiffness. Indicated by the improved equivalent circuit, the use of hollow stem support in this dissertation successfully suppressed energy loss via substrate and has enabled quality factors as high as 56,061 at 329 MHz and 93,231 at 178 MHz—values now in the same range as previous disk resonators employing multiple materials with more complex fabrication processes. To reduce a filter's bandwidth and termination resistance, the thesis also demonstrated a high-stiffness 50-resonator mechanically coupled disk array composite, which not only showed 46.5× improvement in motional resistance, but also a 3.5× frequency stability enhancement against dc-bias voltage fluctuations. Finally, the last chapter demonstrated a 75 MHz 3rd-order channel select (210 kHz) filter based on coupled flexural mode disk resonators with Qs >10,000, which achieved an improved 20 dB shape factor of 1.46 compared with previous measured 2nd order capacitive-gap filters in VHF range.

6.1.1. Implications on High Q Resonator Design

The measured Q enhancements of 2.6× for hollow stem radial-contour mode disk resonators at 154 MHz and 2.9× for wine glass mode ones at 112 MHz versus identically dimensioned full stem counterparts confirms the efficacy of the hollow stem approach for maximizing resonator Q. This approach not only circumvents lithography challenges

otherwise needed by other stem-size reducing Q-enhancement approaches, but does so with zero increase in fabrication complexity over conventional methods for achieving stemmed resonators, making it a very simple and effective way to enhance quality factor. By introducing a new small-signal equivalent circuit that employs a transmission line T-network and a substrate resistor to model magnitude of anchor loss, resonator designers can now predict anchor loss dominated Q without the need to perform finite element simulations. Such new equivalent circuit not only aligns the predicted Q's accurately with measurement data for both hollow stem and full stem disk resonators of different stem radii, but also provides important implications and guidelines for high Q micromechanical disk resonator design. According to this equivalent circuit model, designers can improve quality factor by optimizing vibration structure dimensions, engineering anchor geometries, and choosing materials with appropriate properties. The following summarizes some design guidelines extracted from this new equivalent circuit model for high-Q micromechanical disk resonators.

A. Disk Thickness

By increasing the displacement transformer ratio η_{sub} in Figure 2.5, the equivalent resistance looking into the displacement transformer from the *lcr* tank side will decrease, leading to a lower energy loss and higher Q. According to (2.22), one way to boost η_{sub} is to design a thinner disk structure, which will apply smaller vertical stress through the stem onto the substrate and generates less energy dissipation. However, thinning the disk may also increase motional resistance, a situation that could cause problems for oscillator or filter applications [40] [46]. Therefore potential trade-off may exists between quality factor and motional resistance for radial contour mode center supported disk resonators.

B. Stem Geometries

As already analyzed in this dissertation, cross sectional area of a disk stem has a huge impact on resonators' quality factor. However, as stem size goes to extremely small, the strength of stem will be compromised. To overcome this issue, the hollow-stem idea in the thesis actually reduces the stem cross sectional area without jeopardizing the resonator strength.

Another very important geometry that this dissertation doesn't include is the stem length. Similar to an electrical transmission line, what a stem does to substrate resistor r_{sub} is to rotate it clockwise on a Smith Chart. A stem will modify r_{sub} to a minimum value if its length equals quarter wavelength of the acoustic wave in it, leading to minimum energy dissipation via substrate and highest Q. However, in frequency range around 150 MHz, quarter wavelength in polysilicon material is in the order of 13 μm. Such stem length will largely increase fabrication complexity and reduce resonators' strength. For higher frequency such as 1GHz, quarter wavelength for polysilicon material shrinks to 2μm, a much more feasible dimension for center supported disk resonators. Therefore stem length optimization will become more necessary for resonators in GHz frequency range.

C. Material Properties

For contour-mode disk resonators, material with smaller Poisson's ratio will generate less vertical displacement at the center of the disk, as indicated in (2.21), which leads to

smaller forces on the stem and less anchor loss to the substrate. Therefore materials with small Poisson's ratio, such as polydiamond material [18], can be a very good choice for center supported contour mode disk resonators.

6.1.2. Impact on Applications (Negative Capacitance Equivalent Circuit)

The newly developed equivalent circuit model based on negative capacitance provides improved visualization that helps to identify methods to suppress electrical stiffness induced frequency variation.

A. Drive and Sense Type

From a practical circuit perspective, the use of small source and load resistances equates to the use of voltage drive and current sensing. Conversely, the use of large source and load resistances equates to the use of current drive and voltage sensing. From the discussion in Section 4.3 in Chapter 4, voltage drive makes most sense where frequency tuning is needed, such as for a tunable filter passband application, or a voltage-controlled oscillator. On the other hand, current drive is most appropriate when frequency stability is paramount.

One example application where the choice of drive and sense type could make a big difference is that of a reference oscillator that must be stable against a variety of environmental perturbations. These include acceleration, power supply noise, drift, and undue charging (e.g., due to radiation), all of which can induce instability in the oscillator's frequency. The most significant mechanism for frequency instability caused by these particular perturbations ends up being instability in the electrical stiffness. As revealed by the negative capacitance equivalent circuit in Figure 2.3(b), frequency dependence on electrical stiffness can essentially be nulled by using a high impedance input, high impedance output sustaining amplifier. Here, high impedance is defined relative to the impedance presented by the shunt C_{oi} at the resonator I/O terminals, i.e., the resistance presented by the drive/sense circuit loading each I/O port is considered "high" when it is at least 5 times larger than $1/(sC_{oi})$. This suggests that to maximize frequency stability against environmental variations, a Pierce oscillator [59] configuration would be a better choice than the commonly used transresistance sustaining amplifier.

On the other hand, if frequency tuning is important, and slight instabilities due to environmental perturbations can be tolerated, a low impedance input, low impedance output sustaining amplifier is most suitable, such as a transresistance amplifier [60].

B. Device Design Insights

For the case where frequency stability is of most interest, the negative capacitance equivalent circuit offers a very important insight: The highest stability against changes in bias voltage or overlap capacitance comes when the positive C_{oi}'s can cancel the negative ones. It will ensure maximum stability if C_{oi} can be made much greater so that its impedance is smaller than any load resistance on a given terminal.

This simple fact now reveals several methods by which the frequency stability of a capacitive-gap transduced resonator can be maximized:

1) Utilize large arrays of resonators, perhaps mechanically coupled into array composites like that of [8] and [27]. The use of many devices increases the total input or output C_{oi} so that it swamps any terminal load resistance.

2) Use solid dielectric gaps, such as demonstrated in [43] and [44]. Here, simply raising the gap permittivity again raises C_{oi} so that it dominates over any terminal resistance.

3) Employ small gap spacings, which not only improves motional resistance, but also raises C_{oi} to cancel more of the electrical stiffness that is represented by $-C_{oi}$.

Needless to say, design insights like these made possible by the negative capacitance equivalent circuit that can greatly improve specific performance over others, are invaluable. There are sure to be many other examples, from oscillators, to filters, to mixlers [22], where explicit representation of the negative capacitance in a micromechanical resonator's equivalent circuit proves instrumental to maximizing performance.

6.2. Future Research Directions (Solving the Problems)

This dissertation focuses on the following three aspects of high Q MEMS capacitive-gap resonator design for RF channel selection:

1. Electro-mechanical analogies that predicts anchor loss dominated quality factor and captures frequency pulling effect from electrical stiffness.

2. Hollow stem support for higher micromechanical disk resonator quality factor.

3. Mechanically coupled disk array composite employing high Q resonators with proper electrode phasing design, which increases mechanical stiffness, lowers motional resistance, and enhances frequency stability against environmental fluctuations.

The future research can combine all these techniques and even other recent exciting techniques, such as ALD gap filings [7] or silicide induced gaps [61], into one single device, e.g., a capacitive-gap disk filter based on mechanically coupled hollow stem disk array composites with ALD partially filed gaps, operating at 1 GHz and above.

In the course of investigating high Q micromechanical disk resonators for channel select filters, numerous problems have been raised and identified, including strength compromise from electrode overhangs of hollow stem disk resonators, Q loading and feedthrough current increase of disk array composites from parasitic trace resistance. The following are some suggestions to solve the above mentioned problems.

6.2.1. Electrode Strength

As indicated by the measurements in Chapter 3, the hollow stem device could not accept voltages as large as used for the full stem devices, since the former tended to pull into its electrode vertically when dc-bias voltages exceeded 3V. This is attributable to the thinner electrode overhangs which reduce the strength of hollow stem devices in the vertical

direction. It reveals a limitation of the hollow stem approach, where the much thinner electrode overhang compromises the maximum dc-bias voltage sustainable across the electrode-to-resonator gap before pull-in, leading to a compromised motional resistance.

In the future, an improved fabrication process with CMP (chemical mechanical planarization) process that can eliminate electrode over-hangs would solve this electrode strength compromise and allow the same pull-in voltage for hollow stem disk resonators as its full stem counterparts.

6.2.2. Parasitic Trace Resistance

As indicated by the ac small signal equivalent circuit, any trace parasitic resistance at the I/O ports will be in series with motional resistance R_x, which will lower the effective quality factor of a capacitive-gap resonator and impact a filter's insertion loss, especially for a resonator with low motional resistance such that the trace resistance R_p and motional resistance R_x are comparable. This is true even for trace resistance at the V_p port when there is net current pulled in and out from the resonator body. The relative lower measured Q of array composite compared with single stand-alone disk resonator can be attributable to this factor since array composites will have much lower motional resistance, which makes it more sensitivity to trace resistance Q-loading effect. In addition, trace resistance will also increase the feedthrough current of a resonator array composite, as discussed in Chapter 4, which will eventually lead to lower stopband rejection of a capacitive-gap micromechanical disk filter.

The measured 3rd order filter in Chapter 5 achieves a stopband rejection of 40 dB, which is not good enough for a RF channel select filter that usually requires 60 dB stopband rejection. One important factor that limits the stopband rejection is the current feedthrough path via the resonator structure. By looking at the schematic of a filter in Figure 5.5, designer can see an electrical feedthrough path, which is basically the series combination of input & output electrode-to-resonator overlap capacitance. If the dc-bias voltage terminal has finite trace resistance and cannot shield all feedthrough current from the input, it will reach to the output port and increase the stopband rejection level.

To solve this, the first step is to lower trace resistance on the dc-bias voltage port so that it can ground more feedthrough current. This is especially important when array composites are employed in a filter since the V_p line trace resistance doesn't scale down as the impedance of electrode-to-resonator overlap capacitance decreases. On the contrary, the trace resistance may even increase because of longer routing in an array composite. This will make it more difficult for dc-bias voltage to shunt the feedthrough current to ac ground.

Below are several thoughts that can suppress the above mentioned Q loading and stopband rejection compromise caused by parasitic trace resistance:

1. Increase the thickness of the doped polysilicon trace routing layer. However, this may pose fabrication challenges on etching and topography management.
2. Use metal or silicide material as interconnect.

3. Make coupling beam non-conductive, which will cut off the electrical path for feedthrough current, e.g. using masked doping to control locations that are conductive or not.

6.2.3. Parasitic Capacitance

The measured filter response also shows a higher passband ripple of 4.5 dB than the designed 1 dB. This is partially attributable to the parasitic capacitance between the I/O electrode and the conductive silicon wafer substrate, which increases the effective input capacitance and lowers C_x/C_o, leading to compromised electromechanical coupling strength. Reducing interconnect area, using non-conductive high resistivity wafer, or integrating micromechanical filters with on-chip termination resistance would render a capacitive-gap MEMS filter with flat passband in the future, which could be potentially used in an RF channel select application.

Bibliography

[1] M. Dillinger, K. Madani and N. Alonistioti, Software Defined Radio: Architecture, Systems and Functions, Wiley, 2003.

[2] J. Mitola, "The software radio architecture," *IEEE Communications Magazine,* vol. 33, no. 5, pp. 26-38, May 1995.

[3] C. T.-C. Nguyen, "MEMS-based RF channel selection for true software-defined cognitive radio and low-power sensor communications," *IEEE Communications Magazine,* pp. 110-119, Apr. 2013.

[4] A. I. Zverev, Handbook of Filter synthesis, Hoboken, New Jersey: John Wiley & Sons, Inc., 1967.

[5] T. Naing, T. Beyazoglu, L. Wu, M. Akgul, Z. Ren, T. Rocheleau and C. T.-C. Nguyen, "2.97-GHz CVD diamond ring resonator with Q> 40,000," in *IEEE International Frequency Control Symposium*, Baltimore, MD, May 21-24, 2012, pp. 570-575.

[6] C.-M. Y. V. Lin, J. Zou, Y.-Y. Chen and A. P. Pisano, "Micromachined One-Port Aluminum Nitride Lamb Wave Resonators Utilizing the Lowest-Order Symmetric Mode," *Journal of Microelectromechanical Systems,* vol. 23, no. 1, pp. 78-91, Feb. 2014.

[7] M. Akgul, B. Kim, Z. Ren and C. T.-C. Nguyen, "Capacitively transduced micromechanical resonators with simultaneous low motional resistance and Q > 70,000," in *Hilton Head Workshop*, Hilton Head Island, South Carolina, 2010.

[8] M. U. Demirci and C. T. -C. Nguyen, "Mechanically corner-coupled square microresonator array for reduced series motional resistance," *Journal of Microelectromechanical Systems,* vol. 15, no. 6, pp. 1419-1436, Dec. 2006.

[9] K. Wang, A.-C. Wong and C. T.-C. Nguyen, "VHF free-free beam high-Q micromechanical resonators," *Journal of Microelectromechanical Systems,* vol. 9, no. 3, pp. 347-360, 2000.

[10] J. E.-Y. Lee, Y. Zhu and A. A. Seshia, "A bulk acoustic mode single-crystal silicon microresonator with a high-quality factor," *Journal of Micromechanics and Microengineering,* vol. 18, no. 6, 2008.

[11] J. Wang, Z. Ren and C. T.-C. Nguyen, "1.156-GHz self-aligned vibrating micromechanical disk resonator," *IEEE Transactions on Ultrasonics, Ferroelectrics, and Frequency Control,* vol. 51, no. 12, pp. 1607-1628, Dec. 2004.

[12] Y.-W. Lin, S.-S. Li, Z. Ren and C. T.-C. Nguyen, "Low phase noise array-composite micromechanical wine-glass disk oscillator," in *Technical Digest, IEEE, Int. Electron Device Mtg.*, Washington, DC, Dec. 5-7, 2005, pp. 287-290.

[13] W.-C. Li, Y. Lin, B. Kim, Z. Ren and C. T.-C. Nguyen, "Quality factor enhancement in micromechanical resonators at cryogenic temperatures," in *the 15th International Conference on Solid-State Sensors, Actuators, & Microsystems*, Denver, Colorado, Jun. 21-25, 2009, pp. 1445-1448.

[14] R. Jansen et al., "Optimal T-support anchoring for bar-type BAW resonators," in *24th International IEEE Micro Electro Mechanical Systems Conference*, Cancun, Mexico, Jan. 23-27, 2011, pp. 609-612.

[15] J. Wang, J. E. Butler, T. Feygelson and C. T.-C. Nguyen, "1.51-GHz polydiamond micromechanical disk resonator with impedance-mismatched isolating support," in *17th*

International IEEE Micro Electro Mechanical Systems Conference, Maastricht, The Netherlands, Jan. 25-29, 2004, pp. 641-644.

[16] R. A. Johnson, Mechanical Filters in Electronics, New York: Wiley, 1983.

[17] Y. Xie, S.-S. Li, Y.-W. Lin, Z. Ren and C. T.-C. Nguyen, "1.52-GHz Micromechanical extensional wine-glass mode ring resonators," *IEEE Transactions on Ultrasonics, Ferroelectrics, and Frequency Control,* vol. 55, no. 4, pp. 890-907, Apr. 2008.

[18] M. Akgul, R. Schneider, Z. Ren, G. Chandler, V. Yeh and C. T.-C. Nguyen, "Hot filament CVD conductive microcrystalline diamond for high Q, high acoustic velocity micromechanical resonators," in *Joint Conference of the IEEE International Frequency Control and the European Frequency and Time Forum (FCS)*, San Francisco, CA, May 2011, pp 1-6.

[19] Z. Hao and Y. Xu, "Vibration displacement on substrate due to time-harmonic stress sources from a micromechanical resonator," *Journal of Sound and Vibration,* vol. 322, no. 1-2, pp. 196-215, Apr. 2009.

[20] D. S. Bindel and S. Govindjee, "Elastic PMLs for resonator anchor loss simulation," *International Journal for Numerical Methods in Engineering,* vol. 64, no. 6, pp. 789-818, Oct. 2005.

[21] Y.-H. Park and K. C. Park, "High-Fidelity modeling of MEMS resonators - Part I: anchor loss mechanisms through substrate," *Journal of Microelectromechanical Systems,* vol. 13, no. 2, pp. 238-247, Apr. 2004.

[22] A.-C. Wong and C. T.-C. Nguyen, "Micromechanical mixer-filters," *Journal of Microelectromechanical Systems,* vol. 13, no. 1, pp. 100-112, Feb. 2004.

[23] M. Agarwal, K. Park, M. Hopcroft, S. Chandorkar, R. N. Candler, B. Kim, R. Melamud, G. Yama, B. Murmann and T. W. Kenny, "Effects of mechanical vibrations and bias voltage noise on phase noise of MEMS resonator based oscillators," in *19th IEEE International Micro Electro Mechanical System Conference*, Istanbul, Turkey, Jan. 22-26, 2006.

[24] G. Bahl, R. Melamud, B. Kim, S. A. Chandorkar, J. C. Salvia, M. A. Hopcroft, D. Elata, R. G. Hennessy, R. N. Candler, R. T. Howe and T. W. Kenny, "Model and observations of dielectric charge in thermally oxidized silicon resonators," *Journal of Microelectromechanical Systems,* vol. 19, no. 1, pp. 162-174, 2010.

[25] M. Akgul, L. Wu, Z. Ren and C. T.-C. Nguyen, "A negative-capacitance equivalent circuit model for parallel-plate capacitive-gap-transduced micromechanical resonators," *IEEE Transactions on Ultrasonics, Ferroelectrics, and Frequency Control,* vol. 61, no. 5, pp. 849-869, Apr. 2014.

[26] L. Wu, M. Akgul, Z. Ren, Y. Lin, W. Li and C. T.-C. Nguyen, "Hollow stems for higher micromechanical disk resonator quality factor," in *IEEE International Ultrasonics Symposium*, Orlando, FL, Oct. 18-21, 2011, pp. 1964-1967.

[27] L. Wu, M. Akgul, W. Li, Y. Lin, Z. Ren, T. Rocheleau and C. T.-C. Nguyen, "Micromechanical disk array for enhanced frequency stability against bias voltage fluctuations," in *Joint UFFC, EFTF and PFM Symposium*, Prague, Czech, Jul. 21-25, 2013, pp. 547-550.

[28] R. N. Candler, A. Duwel, M. Varghese, S. A. Chandorkar, M. A. Hopcroft, W.-T. Park, B. Kim, G. Yama, A. Partridge, M. Lutz and T. W. Kenny, "Impact of Geometry on Thermoelastic Dissipation in Micromechanical Resonant Beams," *Journal of Microelectromechanical Systems,* vol. 15, no. 4, pp. 927-934, 2006.

[29] R. Tabrizian, M. Rais-Zadeh and F. Ayazi, "Effect of phonon interactions on limiting the fQ product of micromechanical resonators," in *the 15th International Conference on Solid-State Sensors, Actuators, & Microsystems*, Denver, Colorado, Jun 21-25, 2009, pp 2131-2134.

[30] E. Anastassakis, A. Cantarero and M. Cardona, "Piezo-Raman measurements and anharmonic parameters in silicon and diamond," *Physical Review B,* vol. 41, no. 11, pp. 7529-7535, 1990.

[31] M. Onoe, "Contour vibrations of isotropic circular plates," *The Journal of the Acoustical Society of America,* vol. 28, no. 6, pp. 1158-1162, Nov. 1956.

[32] Z. Hao and F. Ayazi, "Support loss in the radial bulk-mode vibrations of center-supported micromehanical disk resonators," *Sensors and Actuators A: Physical,* vol. 134, no. 2, pp. 582-593, Mar. 2007.

[33] G. Miller and H. Pursey, "The field and radiation impedance of mechanical radiators on the free surface of a semi-infinite isotropic solid," *Proceedings of the Royal Society of London. Series A, Mathematical and Physical Sciences,* vol. 223, no. 1155, pp. 521-541, May 20, 1954.

[34] Z. Hao and F. Ayazi, "Support loss in micromechanical disk resonators," in *18th IEEE International Conference on Micro Electro Mechanical Systems*, Miami, Florida, Jan. 30-Feb. 3, 2005, pp. 137-141.

[35] W. C. L. Hu and D. D. Kana, "Four-pole parameters for impedance analyses of conical and cylindrical shells under axial excitations," *The Journal of Acoustical Society of America,* vol. 43, no. 4, pp. 683-690, 1968.

[36] J. Strutt (3rd Baron Rayleigh), The Theory of Sound, Dover: New York, 1945.

[37] K. Wang and C. T.-C. Nguyen, "High-Order medium frequency micromechanical electronic filters," *Journal of Microelectromechanical Systems,* vol. 8, no. 4, pp. 534-557, Dec. 1999.

[38] B. H. Tongue, Principles of Vibration, New York: Oxford University Press, 1996.

[39] Y. Lin, W.-C. Li, B. Kim, Y.-W. Lin, Z. Ren and C. T. -C. Nguyen, "Enhancement of micromechanical resonator manufacturing precision via mechanically-coupled arraying," in *IEEE International Frequency Control Symposium*, Besancon, France, Apr. 20-24, 2009, pp. 58-63.

[40] T. L. Naing, T. O. Rocheleau, E. Alon and C. T.-C. Nguyen, "A 78-Microwatt GSM Phase Noise-Compliant Pierce Oscillator Referenced to a 61-MHz Wine-Glass Disk Resonator," in *the 2013 Joint UFFC, EFTF, and PFM Symposium*, Prague, Czech Republic, Jul. 21-25, 2013, pp. 562-565.

[41] V. Kaajakari, T. Mattila, A. Oja, J. Kiihamaki and H. Seppa, "Square-extensional mode single-crystal silicon micromechanical resonator for low-phase-noise oscillator application," *IEEE Electron Device Letters,* vol. 25, no. 4, pp. 173-175, Apr. 2004.

[42] B. Kim, M. Akgul, Y. Lin, W.-C. Li, Z. Ren and C. T.-C. Nguyen, "Acceleration sensitivity of small-gap capacitive micromechanical resonator oscillators," in *IEEE International Frequency Control Symposium*, Newport Beach, USA, June 1-4, 2010, pp. 273-278.

[43] Y.-W. Lin, S.-S. Li, Y. Xie, Z. Ren and C. T.-C. Nguyen, "Vibrating micromechanical resonators with solid dielectric capacitive transducer gaps," in *IEEE International Frequency Control Symposium*, Vancouver, Canada, Aug. 29-31, 2005, pp. 128-134.

[44] D. Weinstein and S. A. Bhave, "Internal dielectric transduction in bulk-mode resonators," *Journal of Microelectromechanical Systems,* vol. 18, no. 6, pp. 1401-1408, 2009.

[45] M. A. Abdelmoneum, M. U. Demirci, Y.-W. Lin and C. T.-C. Nguyen, "Location-dependent frequency tuning of vibrating micromechanical resonators via laser trimming," in *IEEE Int. Ultrasonics, Ferroelectrics, and Frequency Control 50th Anniv. Joint Conf.*, Montreal, Canada, Aug. 24-27, 2004, pp. 272-279.

[46] M. Akgul and C. T.-C. Nguyen, "A passband-corrected high rejection channel-select micromechanical disk filter," in *IEEE International Frequency Control Symposium*, Taipei, May 19-22, 2014, pp. 1-6.

[47] M. U. Demirci and C. T.-C. Nguyen, "A low impedance VHF imcromechanical filter using coupled-array composite resonators," in *the 13th Int. Conf. on Solid-State Sensors & Actuators (Transducers'05)*, Seoul, Korea, Jun. 5-9, 2005, pp. 2131-2134.

[48] S.-S. Li , Y.-W. Lin and C. T.-C. Nguyen, "An MSI micromechanical differential disk-array filter," in *the 14th Int. Conf. on Solid-State Sensors & Actuators (Transducers'07)*, Lyon, France, June 11-14, 2007, pp. 307-311.

[49] A. W. Leissa, Vibration of plates, Washington, DC, United States: National Aeronautics and Space Administration (NASA), 1969.

[50] R. D. Blevins, Formulas for natural frequency and mode shape, New York: Van Nostrand Reinhold Co., 1979.

[51] H. C. Nathanson, W. E. Newell, R. A. Wickstrom and J. J. Davis, "The resonant gate transistor," *Electron Devices, IEEE Transactions on,* vol. 14, no. 3, pp. 117-133, 1967.

[52] F. D. Bannon, J. R. Clark and C. T.-C. Nguyen, "High-Q HF micromechanical filters," *IEEE Journal of Solid-State Circuits,* vol. 35, no. 4, pp. 512-526, 2000.

[53] H. A. C. Tilmans and R. Legtenberg, "Electrostatically driven vacuum-encapsulated polysilicon resonators: Part II. Theory and performance," *Sensors and Actuators A: Physical,* vol. 45, no. 1, pp. 67-84, Oct. 1994.

[54] S. Timoshenko, Strength of materials, New York: D. Van Nostrand company, inc., 1930.

[55] A. C. Ugural and S. K. Fenster, Advanced Strength and Applied Elasticity, Upper Saddle River, New Jersey: Pearson Education, Inc., 2003.

[56] J. N. Nilchi, R. Liu and C. T.-C. Nguyen, "7th order sharp-roll-off bridged micromechanical filter," in *the 18th International Conference on Solid-State Sensors, Actuators and Microsystems (TRANSDUCERS 2015)*, Anchorage, AK, Jun. 21-25, 2015, pp. 137-140.

[57] M. Akgul, "A Micromechanical RF Channelizer, PhD Dissertation," EECS Department, UC Berkeley, Berkeley, CA, 2015.

[58] Y. Lin, R. Liu, W.-C. Li and M. Akgul, "A micromechanical resonant charge pump," in *The 17th International Conference on Solid-State Sensors, Actuators and Microsystems (Transducers 2013)*, Barcelona, Spain, June 16-20, 2013 pp. 1727-1730.

[59] S. Lee, M. U. Demirci and C. T.-C. Nguyen, "A 10-MHz Micromechanical Resonator Pierce Reference Oscillator," in *Digest of Tech. Papers of the 11th International Conference on Solid-State Sensors & Actuators*, Munich, Germany, June 10-14, 2001, pp. 1094-1097.

[60] Y.-W. Lin, S. Lee, S.-S. Li, Y. Xie, Z. Ren and C. T.-C. Nguyen, "Series-resonant VHF micromechanical resonator reference oscillators," *IEEE Journal of Solid-State Circuits,* vol. 39, no. 12, pp. 2477-2491, Dec. 2004.

[61] L.-W. Hung and C. T.-C. Nguyen, "Silicide-based release of high aspect-ratio microstructures," in *The 23rd International Conference on Micro Electro Mechanical Systems (MEMS 2010)*, Hong Kong, China, Jan. 24-28, 2010, pp. 120-123.

[62] G. Piazza, P. J. Stephanou and A. P. Pisano, "Piezoelectric aluminum nitride vibrating contour-mode MEMS resonators," *Journal of Microelectromechanical Systems,* vol. 15, no. 6, pp. 1406-1418, Dec. 2006.